SIGNIFICANCE OF MID-MIOCENE VOLCANISM IN NORTHEAST NEVADA: PETROGRAPHIC, CHEMICAL, ISOTOPIC, AND TEMPORAL IMPORTANCE OF THE JARBIDGE RHYOLITE

by

JEFFREY SCOTT CALLICOAT

B.S., EASTERN ILLINOIS UNIVERSITY, 2008

A THESIS

submitted in partial fulfillment of the requirements for the degree

MASTER OF SCIENCE

Department of Geology
College of Arts and Sciences

KANSAS STATE UNIVERSITY
Manhattan, Kansas

2010

Approved by:

Major Professor
Matthew E. Brueseke

Abstract

The Jarbidge Rhyolite of Elko County, Nevada, is approximately 26 mapped bodies of porphyritic rhyolite. Several of the bodies are truncated by the Idaho or Utah border, and extend into the states for an unknown distance. This study focuses on five bodies, the Mahoganies, two near Wild Horse Reservoir, the outcrop enclosing the Jarbidge Mountains, and one outcrop south of Wells. The study's focus is providing field, petrography, geochemistry, oxygen isotope, and geochronology information about the five previously mentioned bodies. Physical volcanology encountered during this study indicates the sampled Jarbidge Rhyolite are effusive lava flows and domes that coalesced over the life of the volcanic system. First order approximations indicate that erupted products cover ~1,289 km^2 and erupted material totals ~509 km^3. Petrography indicates primary anhydrous mineral assemblages, assimilation of granitoid, possible assimilation of metamorphic rock and magma mixing of mafic and silicic bodies. Collectively, the Jarbidge Rhyolite lava flows sampled are compositionally restricted from rhyolite to high silica rhyolite and all samples demonstrate A-type magma characteristics. Compositions from different bodies overlap on Harker diagrams, and trace element ratios distinguish few flows from the other samples. Rare earth element patterns mimic one another, and incompatible trace element ratios overlap between bodies, likely indicating the presence of one large magma body. Oxygen isotope values for selected samples range 6.61-8.95‰$_{VSMOW}$ are coincident with normal igneous values. New $^{40}Ar/^{39}Ar$ geochronology indicates Jarbidge Rhyolite volcanism initiated ca. 16.7 Ma near Wild Horse Reservoir and was active at Bear Creek Summit ca.15.8 Ma. Local Steens Basalt, geochemistry, and Au-Ag mineralization indicate Jarbidge Rhyolite is similar to Middle Miocene silicic volcanics (e.g. Santa Rosa-Calico volcanic field) further west in the Oregon-Idaho-Nevada tristate region.

Table of Contents

List of Figures v
List of Tables vii
Acknowledgements viii
CHAPTER 1 - INTRODUCTION 1
Regional Geology 1
Regional Overview and Local Geology 2
CHAPTER 2 - METHODS 8
Field Methods and Petrography 8
Sample Preparation 8
Geochemical Analysis Preparation 9
$^{40}Ar/^{39}Ar$ Geochronology 11
Oxygen Isotope Analysis 11
Volume Estimates 12
CHAPTER 3 - FIELD RELATIONS 14
CHAPTER 4 - PETROGRAPHY 30
Xenocrysts, Xenocryst Clots and Weathering Products 36
CHAPTER 5 - GEOCHEMISTRY 39
Major Element Geochemistry 39
Trace Element Geochemistry 43
Rare Earth Element Geochemistry 45
CHAPTER 6 - OXYGEN ISOTOPES 48
CHAPTER 7 - GEOCHRONOLOGY 50
CHAPTER 8 - DISCUSSION 55
Physical Characteristics 55
Petrography 56
Geochemistry 58
Oxygen Isotopes 60
Geochronology 61

Regional Comparison 61
CHAPTER 9 - SUMMARY 65
CHAPTER 10 - SUGGESTED FUTURE WORK 66
References 67
Appendix A - Sample Locations and Petrographic Descriptions 76
Appendix B - Geochemistry 92
DCP-AES Major Element Results 92
DCP-AES Trace Element Results 95
ICP-MS Trace Element Results 98
Appendix C - Oxygen Isotope Analysis 101
Appendix D - Geochronology 102

List of Figures

Figure 1: Generalized mid-Miocene to present map of the NW USA. 3
Figure 2: Simplified geologic map of Elko County, NV. 6
Figure 3: Simplified geologic map of study area 7
Figure 4: Graphic depiction of volume calculation. 13
Figure 5: Sample location map. 14
Figure 6: Oxidized flow breccia south of Charleston. 17
Figure 7: Flow margin south of Charleston 18
Figure 8: Vertical joints in peak 8627, Mary's River Basin. 19
Figure 9: Upper vitrophyric breccia in Mary's River Basin transect. 20
Figure 10: View of Coon Creek Summit and adjacent area. 21
Figure 11: Flow fold in Coon Creek Summit. 22
Figure 12: Basal vitrophyre and stony rhyolite contact in Coon Creek Summit outcrop. 23
Figure 13: Jointed vitrophyric neck in Coon Creek Summit. 24
Figure 14: Jointed vitrophyric neck in Coon Creek Summit 25
Figure 15: Ramp structure located in south facing slope of Deer Mountain. 26
Figure 16: Mahoganies outcrop. 27
Figure 17: Wild Horse Reservoir outcrop. 28
Figure 18: Wild Horse Reservoir Dome outcrop. 29
Figure 19: Plagioclase crystals 30
Figure 20:Flow textures. 31
Figure 21: Summary of primary mineral phases 32
Figure 22: Photomicrographs of quartz open-system textures. 33
Figure 23: Photomicrographs of feldspar open-system textures 34
Figure 24: Photomicrographs of xenocrysts phases 35
Figure 25: Summary of phenocrysts phases. 37
Figure 26: Total alkali silica diagram. 40
Figure 27: Major element classification diagrams. 41
Figure 28: Major element Harker diagrams. 42
Figure 29: Trace element Harker diagrams 44

Figure 30: Multiple element plot of MORB normalized Seventy Six basalt, and Steens Basalt . 45
Figure 31: Ba vs. CaO, K_2O, Sr, and Eu plots. 46
Figure 32: Upper continental crust and chondrite normalized multiple element plot. 47
Figure 33: La/Lu_N Harker. 47
Figure 34: Diagram of $\delta^{18}O_{quartz}$ and $\delta^{18}O_{feldspar}$. 49
Figure 35: Approximate location of dated samples and ages. 51
Figure 36: Ideogram of sample JC-08-10. 52
Figure 37: Incremental step heating results for sample JC-08-24 53
Figure 38: Ideogram of sample JC-08-25. 54
Figure 39: Quartz-albite-orthoclase pseudo ternary diagram. 59
Figure 40: Comparative geochemical diagrams. 63
Figure 41: Comparative mulitple element plots 64

List of Tables

Table 1: Area and volume estimates of erupted products 15
Table 2: Oxygen isotope summary. 48
Table 3: Summary of single crystal geochronology 50
Table 4: Summary of $^{40}Ar/^{39}Ar$ geochronology via incremental heating technique. 50

Acknowledgements

Thanks to Dr. Matthew Brueseke for discussions about volcanology and igneous petrology, funding and discussing the project, and encouraging me to apply for the National Science Foundation fellowship and Geological Society of America Penrose Conference. Also, thanks to Dr. Allen Archer and Dr. Jack Oviatt for being committee members, Dr. John Morton at Miami University for geochemistry sample analysis, Dr. Willis Hames at Auburn University, Alabama for his role with geochronology, Dr. Peter Larson at Washington State University for the oxygen isotope analyses, Andy Neal and Bobby Ford for geologic discussions, and last, but certainly not least, my wife Lisa and family for their support.

CHAPTER 1 - **INTRODUCTION**

Middle Miocene volcanism of the Idaho-Oregon-Nevada (ION) tristate region initiated ca. 16.7 Ma with the eruption of the Steens Basalt, and Columbia River Basalt Group (Camp et al., 2003; Brueseke et al., 2007). Coeval rhyolite volcanism erupted across the ION region ca. 17-14 Ma (Christiansen et al., 2002; Brueseke et al., 2008). Some of the silicic volcanism associated with this event is fairly well studied (e.g. Santa Rosa Calico volcanic field), however, much of the regional volcanism is poorly understood with respect to its temporal and genetic nature.

The Jarbidge Rhyolite is several bodies of quartz phyric lava and ash flows and fall (Coats, 1964; Bernt, 1998) found throughout Elko County, Nevada, east of the most studied mid-Miocene bimodal volcanism. The Jarbidge Rhyolite was originally described by Schrader (1912), and later named and mapped by Robert Coats (Coats, 1964 & 1987). Previous work includes mapping at the 1:40,000 and 1:250,000 scale and regional geochemical study (Coats, 1964). The geochemical study focused on uranium exploration and was confined to the 15' Jarbidge quadrangle, which contains the 7.5' United States Geological Survey (USGS) Jarbidge North, Jarbidge South, Gods Pocket Peak, and Robinson Creek quadrangles(Coats, 1964). Prior and ongoing work by John Bernt is focused in the vicinity of the Jarbidge Mining district, an area not sampled by this study (Bernt, 1998).

The intent of this study is to provide field, petrographic, geochemical, oxygen isotope and temporal constraints on the Jarbidge Rhyolite to better define it.

Regional Geology

At approximately 17 Ma, the development of the Northern Nevada Rift (NNR) and initiation of the Yellowstone Hotspot/Columbia River Basalt Group (CRBG) occurred (Zoback et al., 1994). Feeder dikes' trends and chemical and temporal similarities between eruptive products of the NNR and CRBG suggest they are regionally similar magmatic systems (Zoback et al., 1994; Hooper et al., 2002; Camp & Ross, 2004; Brueseke and Hart, 2008). The main eruptive phase of the CRBG occurred from ca. 16.6-15.0 Ma and is mainly exposed in Washington (Camp and Ross, 2004), however basaltic volcanism local to the ION tristate region erupted ca. 16.7-14 Ma (Brueseke et al., 2007). The extent of these eruptions can be found at

Abert and Poker Jim Rim, OR (Brueseke et al., 2007), south to the Black Rock desert, NV, east to Copper Basin, NV, and north of the western Snake River Plain (Hart and Carlson, 1985; Camp & Ross, 2004; Brueseke et al., 2007).

Coeval with the flood basalt volcanism, silicic volcanism from diverse eruptive loci formed across the ION tristate area (Fig. 1; Manley and McIntosh, 2002; Brueseke et al., 2007; Starkel et al., 2009). Contemporaneous with this bimodal volcanism was regional extensional tectonism (Zoback et al., 1994; Cummings et al., 2000; Colgan and Henry, 2009) and the development of epithermal bonanza Au-Ag and precious metal deposits (e.g. Jarbidge district, Ivanhoe district, Midas district, National, and DeLamar; John, 2001; Wallace, 2003; Saunders et al., 2008). Extensive silicic lava flows, domes and ash flows were emplaced in north central Nevada ca. 16.7-14 Ma (John, 2001; Wallace et al., 2008; Callicoat and Brueseke, 2009). This regional mid-Miocene tectono-magmatic event has several unifying characteristics: (1) widespread silicic volcanism, from small and large loci, (2) flood basalt magmatism, (3) Au-Ag epithermal mineralization, and (4) similar extensional tectonic stresses.

Two silicic volcanic "fronts" developed from the centralized ION area of silicic volcanism: the High Lava Plains (HLP) and eastern Snake River Plain (ESRP). The HLP is the northwestern progression of bimodal volcanism from the ION tristate region (Jordan et al., 2004). The ESRP begins with the Bruneau-Jarbidge volcanic field, and includes the Twin Falls, Picabo, Heise, and Yellowstone volcanic fields, which decrease in age with northeastward progression (Fig. 1; Armstrong et al., 1975; Christiansen et al., 2002). The volcanic fields in the ESRP erupted large silicic ash flow sheets, with subordinate amounts of silicic lava flows. These were followed by localized basaltic activity that effectively buried the silicic centers under <1 kilometer of basalt (Christiansen and McCurry, 2008).

Regional Overview and Local Geology

The Jarbidge Rhyolite (JR) is a map unit specific to Elko County, NV, and several of the 26 bodies are truncated by state borders with Idaho and Utah (Coats, 1987). Bodies are north of Wild Horse Reservoir, surrounding Wild Horse Reservoir, between Elko and Wild Horse Reservoir, the Jarbidge Mountains and surrounding area, south of Wells, NV, and several bodies are truncated by the Idaho or Utah state boarders (Fig. 2). Many of the bodies are only

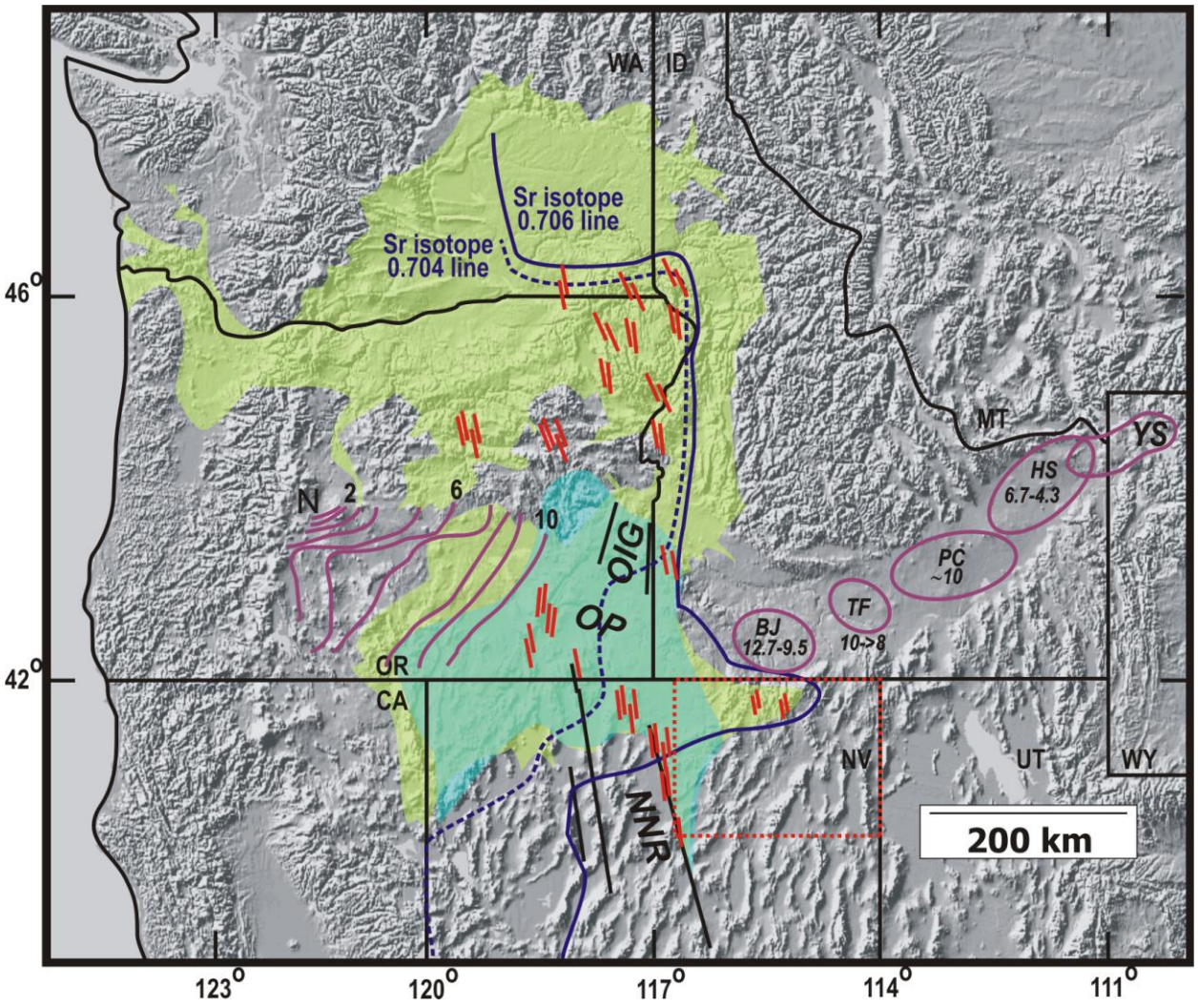

Figure 1: Shaded relief map of Pacific Northwest, US (Brueseke and Hart, 2008). The lime green color indicates the subaerial extent of Cenozoic flood basalt volcanism, red dashes indicate select flood basalt eruptive loci, blue color indicates area of Mid-Miocene silicic magmatism, numbered purple lines are isochrons for the High Lava Plains and numbers correlate to silicic activity (Ma), purple ovals depict volcanic centers associated with the eastern Snake River Plain and numbers bracket the activity of silicic volcanism at a given area. Solid black lines near NNR indicate the approximate strike of aeromagnetic anomalies. Solid black lines near OIG approximate trend of bounding faults of the graben. East of the Sr isotope 0.706 line is approximate edge of craton boundary, and west of the Sr isotope 0.704 boundary is accreted oceanic terranes. Abbreviations are as follows, Northern Nevada Rift (NNR), Oregon Plateau (OP), Oregon-Idaho Graben (OIG), Bruneau-Jarbidge (BJ), Twin Falls (TF), Picabo (PC), Heise (HS), and Yellowstone (YS). The numbers that correspond to BJ, TF, PC, HS, and YS indicate the period of volcanism that the field was active in million years ago.The red dash outline box is approximately defines the approximate location of Figure 2.

accessible by unimproved gravel/dirt roads, and access is limited by lack of roads, designated Wilderness areas, and private property. This study mainly focuses on samples gathered from the Jarbidge South, Mount Ichabod, Badger Creek, Wild Horse, Mary's River Basin NW, Delaware Creek, Tennessee Mountain, and Merritt Mountain USGS 7.5' quadrangles. Sampled bodies with corresponding names are illustrated on Figure 3.

The bodies are located east of the 0.706 $^{87}Sr/^{86}Sr$ line, which delinates the western edge of the North American Craton, as indicated by $^{87}Sr_i/^{86}Sr_i$ range of 0.7101-0.7142, confirming their position over the Proterozoic craton (Christiansen et al., 1986). Additional isotopic data includes an ε_{Nd} value of -24.8, indicating involvement of ancient lithosphere in JR magmatism (Nash et al., 2006). The basalt proximal to the JR is the Seventy Six basalt, which crops out as porphyritic stocks in Copper Basin (CB) and lava flows near Sunflower Reservoir (SR). The Seventy Six basalt CB has an $^{87}Sr_i/^{86}Sr_i = 0.70561$, $^{143}Nd_i/^{144}$ $Nd_i = 0.5124$, $^{206}Pb/^{204}Pb = 18.80$, $^{207}Pb/^{204}Pb = 15.60$, and $^{208}Pb/^{204}Pb = 38.87$ (Carlson and Hart, 1985 & 1987).

The largest outcrop of the rhyolite is the "main body" (MB; Fig. 3), which encompasses the town of Jarbidge, the "type section" and areas to the south. The stratigraphy of this area is being used as representative of the bodies sampled, with the exception of the Wells outcrop. The JR is underlain by Precambrian and Paleozoic metasedimetary rocks (Coats, 1964; Rahl et al., 2002). Cretaceous granitoid intruded the Precambrian and Paleozoic rocks, resulting in garnet bearing skarn bodies (Rahl et al., 2002). Local pre mid-Miocene rocks include Eocene ash flow tuffs interbedded with lacustrine strata and debris flow deposits (Rahl et al., 2002; Henry, 2008). Overlying the tuffs and sedimentary strata are the Seventy Six basalt stocks and JR (Coats, 1987). Minor amounts of dacite lava flows and tuffs, gravel, and rhyolitic ash flows overlie the JR (Coats, 1987). The northern boundary of the MB outcrop is unconformably overlaid by the younger, ca. 12.7-10.5 Ma, Cougar Point Tuff of the ESRP (Bonnichsen et al., 2008; Coats, 1987; Cathey and Nash, 2004). Following this, the Jarbidge Mountains experienced three different episodes of alpine glaciations which removed an unknown portion of JR (Coats, 1964). Fluvial erosion has occurred during the Pleistocene and as noted by Coats (1964), stream terraces are found at substantial elevations above the current rivers and streams.

Extension occurred in the Copper Basin area ca. 41.3 Ma and ceased prior to the emplacement of Seventy Six basalt and Jarbidge Rhyolite (Rahl et al., 2002). However, multiple mid-late Miocene normal faults cut the Jarbidge rhyolite, with a bimodal distribution of N20°W

and N70°E (Coats, 1964; Zoback et al., 1994). The northwest faults have similar trends to other mid-Miocene structures farther west, including the NNR and flood basalt feeder dikes. Bernt (1998) reports syn-magmatic faulting within the Jarbidge Rhyolite mining district. The faults do not cut the Cougar Point Tuff, indicating extension prior to 12.7 Ma (Coats, 1964; Cathey and Nash, 2004).

The regional volcanics have been dated by several authors who used different methods. The published geochronology indicates JR and Seventy Six basalt volcanism was active ca. 16.8-14 Ma within the study area. Seventy Six basalt dated by K-Ar geochronology yields ages of 12.4 ±0.7 and 15.5 ±0.8 Ma (Hart and Carlson, 1985), and an $^{40}Ar/^{39}Ar$ geochronology of a single plagioclase crystal yields age of 16.5 ±0.2 Ma (Rahl et al., 2002), which is considered more robust than the K-Ar ages. Reported ages of the Jarbidge Rhyolite are ca. 14 Ma within the main body (Bernt, 1998). Geochronology from outside the main body includes an $^{40}Ar/^{39}Ar$ age of 16.2 Ma from the Bull Run Basin (Henry, 2008), a K-Ar age of 16.8± 0.5 Ma from the Mahoganies, a K-Ar age of 15.4 Ma north of Wild Horse Reservoir (Evernden et al., 1964), a K-Ar age of 15.4 Ma east of Wild Horse Reservoir (Coats, 1964), and K-Ar ages of outcrops south of Wells, NV, that indicate activity from ~14.8-13.4 Ma (Snoke et al., 1997).

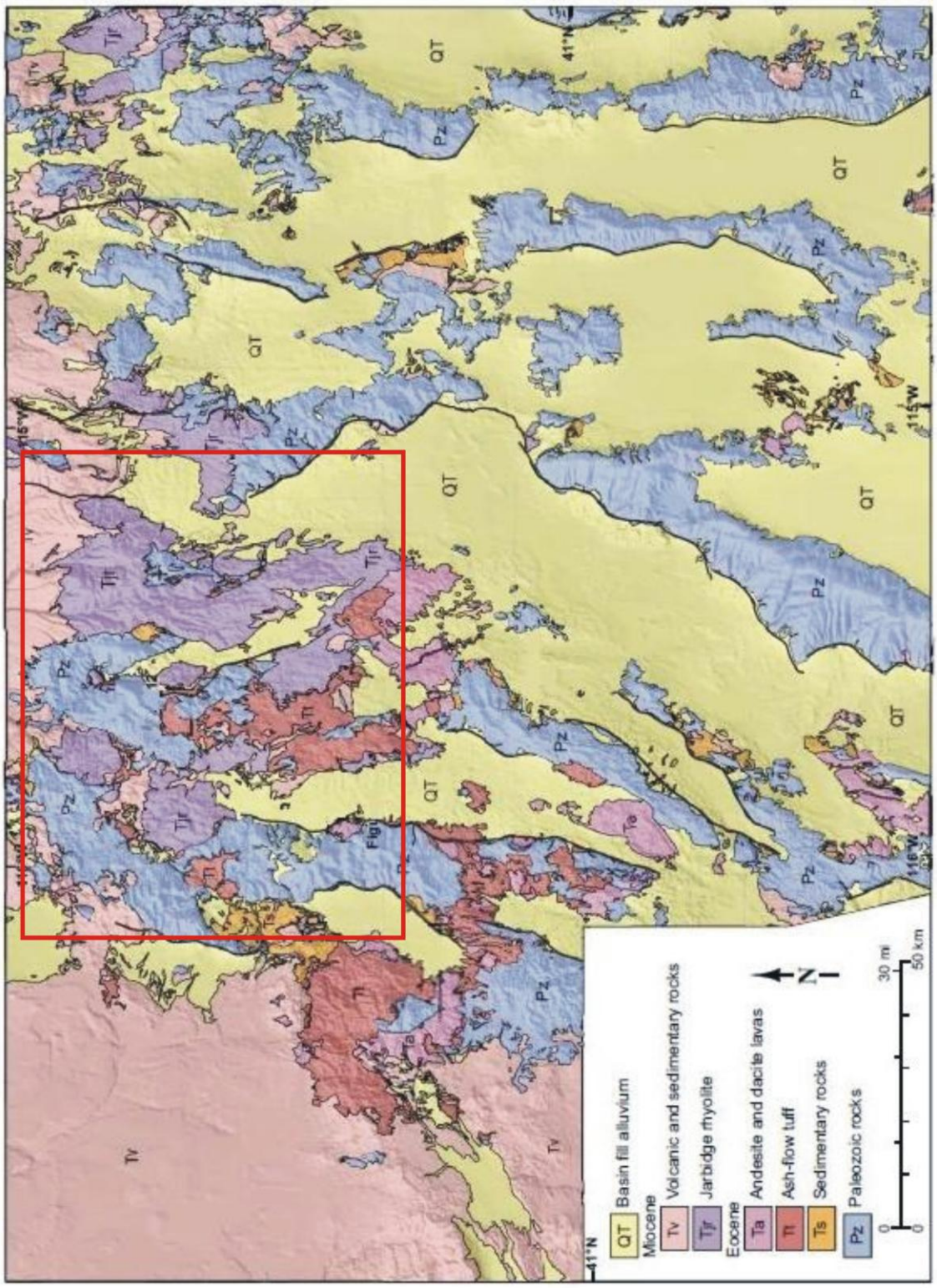

Figure 2: Modified generalized geologic map of Elko County, NV (Henry, 2008; simplified from Coats, 1987). The red box defines the approximate area displayed by Figure 3.

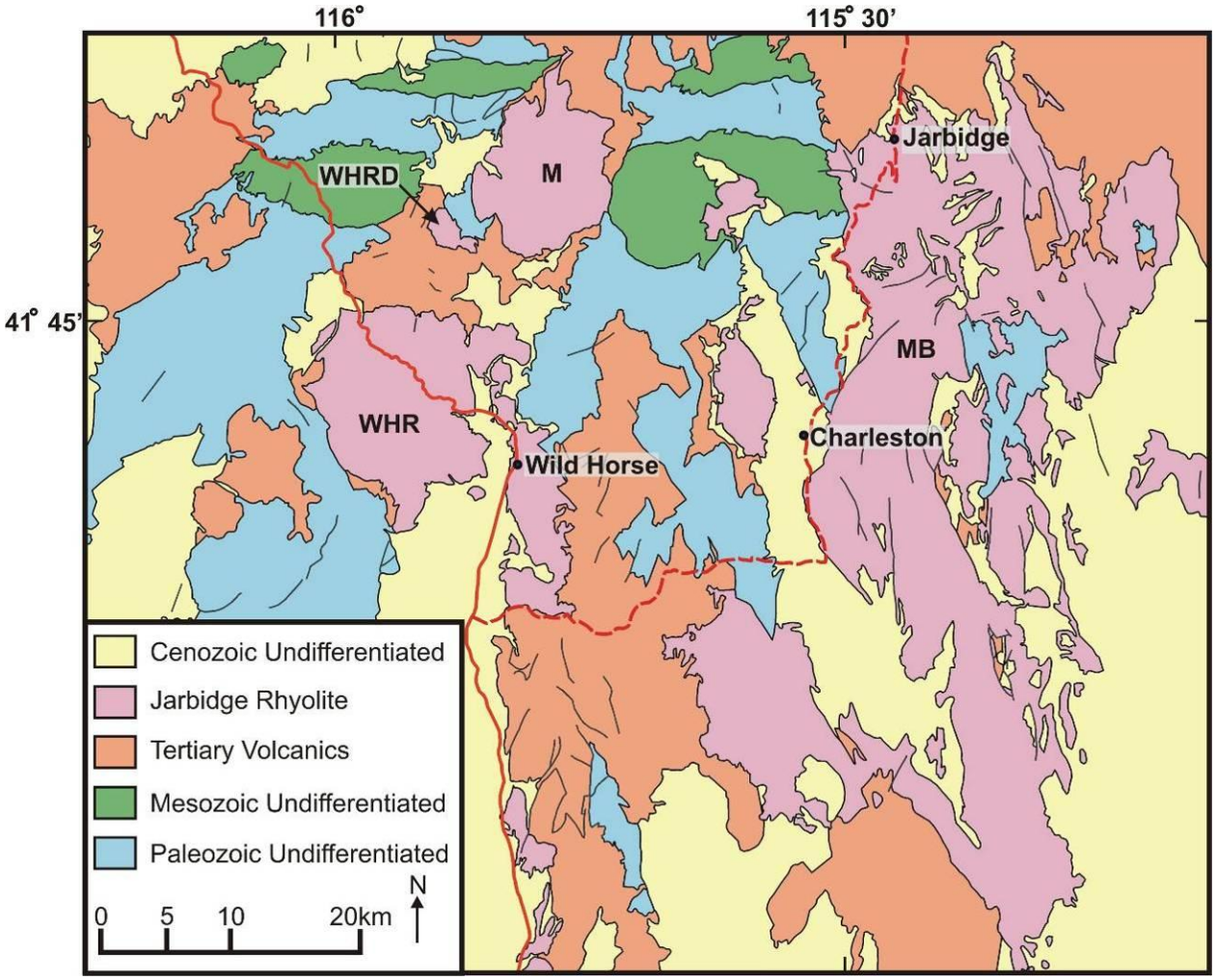

Figure 3: Simplified portion of Coats' (1987) geologic map of Elko County, Nevada. Wild Horse, Charleston, and Jarbidge are local towns whose approximate locations are represented by black circles; solid red line indicates main paved road, and the dashed red line indicates main unpaved road. Thin black lines indicate faults; only faults of considerable magnitude are shown on this figure. "WHRD" is Wild Horse Reservoir dome outcrop, "M" stands for Mahoganies outcrop, "WHR" stands for Wild Horse Reservoir outcrop, and "MB" stands for main body outcrop.

CHAPTER 2 - **METHODS**

Field Methods and Petrography

The Geologic Map of Elko County, Nevada (Coats, 1987) was used to identify bodies of Jarbidge Rhyolite. Sample collection was conducted on foot and I attempted to maximize the number of lava flows sampled. Areas were sampled where physical volcanology indicated different flows (e.g. vitrophyre, change in crystallinity, flow breccias). Sampling from altered lava flows was avoided and in all cases I collected the freshest possible material. The locations of collected samples were recorded using a Garmin e-trex Global Positioning System hand held device set to Universal Transverse Mercator (UTM) coordinates and North American Datum (NAD) of 1927. The coordinates of sampled locations may be found in Appendix A.

Representative samples were point counted with a target of 1,000 counts per thin section and a step interval of 1 mm. Point counting was conducted using the 10x objective and mineral counts were kept on a counter. Photographs were taken using a 4 megapixel camera mounted to a Nikon petrographic microscope. Scales in photomicrographs were digitally added using Spot software.

Sample Preparation

An initial mass of sample to process for petrography, geochemistry, geochronology and oxygen isotope data was based on: crystal size and abundance and alteration. Larger crystal size, higher crystallinity, and more prevalent alteration require larger masses for processing. Samples were split using a Rocklabs hydraulic splitter/crusher with tungsten carbide faces. Samples were split using the "knife edge" arms and reduced to a maximum size of 2.5 x 2 x 2 centimeters. Weathering rinds, apparent alteration, and any contaminant were removed using a diamond tipped rock saw, silica carbide sandpaper mounted on a grinding wheel, and hand picking. Using the rock saw, thin section blanks were cut to fit standard 24 x 44 millimeter thin sections and blanks were sent to Spectrum Petrographics Inc. Samples which had weathering rinds removed via the rock saw were ground with silica carbide sandpaper to remove any adhered metal. All samples were washed in deionized water to remove any adhering powder or contaminant. Samples were crushed using a Rocklabs crusher and reduced until sample pieces had a diameter

of <5 mm. A cone and quarter method was used to obtain a 15-20 ml aliquot of randomized sample. The aliquot was further reduced to a clay size fraction by a Spex Industries aluminum oxides shatter box, resulting in processed sample powder.

Geochemical Analysis Preparation

Loss on ignition (LOI) was determined for all samples analyzed for chemistry. Approximately one gram of processed sample powder was weighed in a ceramic crucible, heated in a muffle furnace at 950° C for one hour, allowed to cool to ambient temperature, and reweighed. LOI= $((mass_{initial}-mass_{final})/(mass_{initial}))*100$. Alteration was assessed by examining LOI with K_2O/Na_2O. Low temperature hydration is commonly deciphered by an increase in wt. % K_2O and SiO_2, decrease in Na_2O, and oxidation of Fe (Stewart, 1979; Riley et al., 2001). Vitrophyre samples have experienced some low temperature hydration as evidenced by the larger a K_2O/Na_2O ratio coinciding with larger LOI numbers (Fig. 20).

Major and trace element chemistry was obtained at Miami University using direct current plasma atomic emission spectroscopy (DCP-AES). An initial solution of nitric acid and trace solution spike was added to a 125 ml plastic bottle. Masses of solution components were recorded and later used for calculating the equivalent dilution. Processed sample powder and a lithium metaborate flux were homogenized and placed in a muffle furnace, resulting in a molten bead. The resultant molten bead was dissolved in an initial solution, resulting in a sample solution. Aliquots of sample solution were used for major and trace element analyses. Blanks were created for the major, minor and spiked solutions and run with samples, in addition to commercial external standards from the United States Geological Survey (USGS) and Japanese Geological Survey. Multi-element cassettes were used for data collection. Major element concentrations of samples were determined by peak intensity comparison with standards of known concentrations. Separate runs for phosphorous concentration were completed. Trace element concentrations were determined by standard addition. Reported concentrations were the result of averaging three runs. Data collection and reduction was performed on specific software written for the DCP-AES at Miami University and the methods follow those of Katoh et al. (1999).

The initial solution contains ~50 grams of 5% HNO_3, spiked with 3,000 ppm Li, 10 ppm Ge, and 20 ppm Cd. Two hundred milligrams of processed sample powder was mixed with 600

milligrams (with a maximum deviation of 0.5 mg) of lithium borate ($LiBO_2$) flux. Sample and flux mixture were placed in a graphite crucible. The crucibles were heated at 950° C in a muffle furnace for twenty minutes. A molten bead formed and was poured into the initial solution. This solution was shaken vigorously and placed on a reciprocating table. The samples stood at ambient temperature for at least twelve hours and if any solid residue remained the mixture was unusable.

Major and Trace Element Dilution:

Approximately one g of the sample solution was added to a 60 ml plastic bottle containing ~25 grams of spiked major solution. The equation to calculate equivalent dilution is: ((mass of major solution + mass of trace aliquot)/mass of trace aliquot)*(trace aliquot mass). Externally run standards include United States Geological Survey's AGV-2, BCR-2, BHVO-2, DNC-1, G-2, GSP-2, and SY-2. Japanese Geological Survey standards include JR-3, and JG-2, and one French Geological Survey standard, BE-N, was also run.

Trace element concentrations were determined by standard addition. Each sample required a set of solutions, one without spike, and two with varying amounts of acid and spike. Each bottle in a set has 10.000+/- 0.006 grams of the original solution added. Then the three bottles had: 0.6 ml of 5% HNO_3, 0.3 ml of HNO_3 and 0.3 ml of trace element spike, and 0.6 mL of trace solution added to them, respectively. External standards that were run are the same as those run for majors.

Data Collection and Reduction:

Data collection and reduction was done by computer software specific to Miami University Geology Department's DCP-AES. The following corrections were applied to the analyses (LeMaitre, 1976).

Oxidation ratio: $(OX)=FeO/(FeO+Fe_2O_3)= 0.93-0.0042\ SiO_2-0.022\ (Na_2O+K_2O)$

$Fe_2O_3=[0.899813(OX)(Fe_2O_3*)-0.899813(Fe_2O_3*)]/[-0.899813-0.100187\ (OX)]$

$FeO=(Fe_2O_3*-Fe_2O_3)/1.111342$

Nb Correction: $Nb_{(final)}=Nb_{(measured)}-(0.108xV_{(measured)})$

Zr Correction: CaO, Al_2O_3, and Fe_2O_3 are converted to ppm

Zr(final)=Zr(measured)/[((Ca+Al+Fe)/Zr(measured))x-0.000021+1.009696]

Rare Earth Element and Trace Element Analyses

Fifty mg of sample and seventy-five mg of sodium tetraborate ($NaBO_2$) and potassium carbonate (K_2CO_3) flux was mixed and homogenized. The mixture was then transferred to a 10 ml graphite crucible and placed in a muffle furnace at 950° C for thirty minutes. The resultant molten bead was allowed to solidify and cool to ambient temperature. Upon reaching ambient temperature, the bead was transferred to a 125 ml bottle containing 1% nitric acid. This solution was placed on a shaking table for several hours until the bead was dissolved. The analysis was performed the following day on a Varian quadrapole intercoupled plasma mass spectrometer (ICP-MS). The instrument is a prototype model with no identifying model name or number associated with it. Reported values are the average of 100 runs.

$^{40}Ar/^{39}Ar$ Geochronology

Three rhyolite samples were dated at Auburn University's Auburn Noble Isotope Mass Analysis Laboratory (ANIMAL) using $^{40}Ar/^{39}Ar$ geochronology. Rhyolite distribution and quantity of dated samples is: one sample from the Wild Horse Reservoir dome outcrop, one from the Wild Horse Reservoir outcrop, and one from the main body.

Multiple sanidine crystals were dated for each sample by a 50W Synrad CO_2 infrared laser. The high sensitivity and low blank of the instrument permits measurement of 10^{-14} mole samples to within 0.02% precision. An analysis is the result of eight cycles of measurement over a range of masses and half masses from m/e=40 to m/e=35.5. Data collection and reduction is facilitated by National Instruments hardware and a Labview program written by lab personnel specifically for ANIMAL. Initial data reduction is accomplished through an in-house Excel spreadsheet, with final reduction using Isoplot (Ludwig, 2003).

Oxygen Isotope Analysis

Crushed sample produced during geochemical preparation was sieved to a >2mm but <0.5 mm size. Quartz and feldspar crystals were separated by hand using binocular microscope. Crystals were chosen based on no visible inclusions, fractures, and alteration. Approximately 20 mg of sample was needed for a single analysis. Several analyses worth of a single sample mineral were sent to the Washington State University GeoAnalytical Lab. Laser fluorination was used to analyze samples. A 20W CO_2 laser was used to liberate oxygen following the laser techniques of Sharp (1990). Liberated oxygen was measured by a Finnigan™ Delta S Isotope

Ratio Mass Spectrometer operated by an ISODAT NT software operating system. The oxygen isotope values were corrected by repeated analysis of the UWG-2 garnet standard (δ^{18}= ~5.8‰), with the range from 0.05‰ to 0.22‰ of analytical precision (Valley et al., 1995; Takuri and Larson, 2005). Some samples have replication data and this can be found appendix C.

Volume Estimates

Volume estimates were obtained using ArcGIS version 9.3.1. Two National Elevation Datasets (NEDs) at one third arc second resolution were downloaded from the seamless map server (http://seamless.usgs.gov/). The NEDs were mosaiced using the mosaic tool in Arc toolbox. The resultant mosaiced raster's cell dimension was reset to 10 x 10 meters. The Geologic Map of Elko County (Coats, 1987) was scanned at a 720 dots per inch resolution, and georeferrenced with a resultant error smaller than the pixel size. All map datum and projections were set to UTM North 11 zone and world grid survey (WGS) of 1984. Bodies were digitized by point and click at ~1:5,000 scale. Spatial analyst, an ArcGIS extension, was used to calculate volumes. The zonal statistics function of spatial analyst determines maximum and minimum surface elevations of a defined area within an NED's boundary. The defined area is established by a polygon, which is a JR outcrop in this case. The lowest surface elevation within a polygon is treated as the lowest elevation of JR witin that outcrop. The raster calculator was used to subtract the minimum elevation from every cell in the NED, and a new NED titled "calculation" was created. The raster calculator works on an individual cell basis, applying a function or operation to each cell in a raster. By multiplying "calculation" by the area of a cell, a third NED, "calculation 2" was created. The multiplication effectively multiplied each thickness value by the area of space it represents, yielding a volume. Zonal statistics was used to sum the values of cells within the borders of a polygon, and the resultant sum reported is the value of erupted material. Overall, it is a cut and fill method. A schematic sketch visual depicts how the method works (Fig. 4).

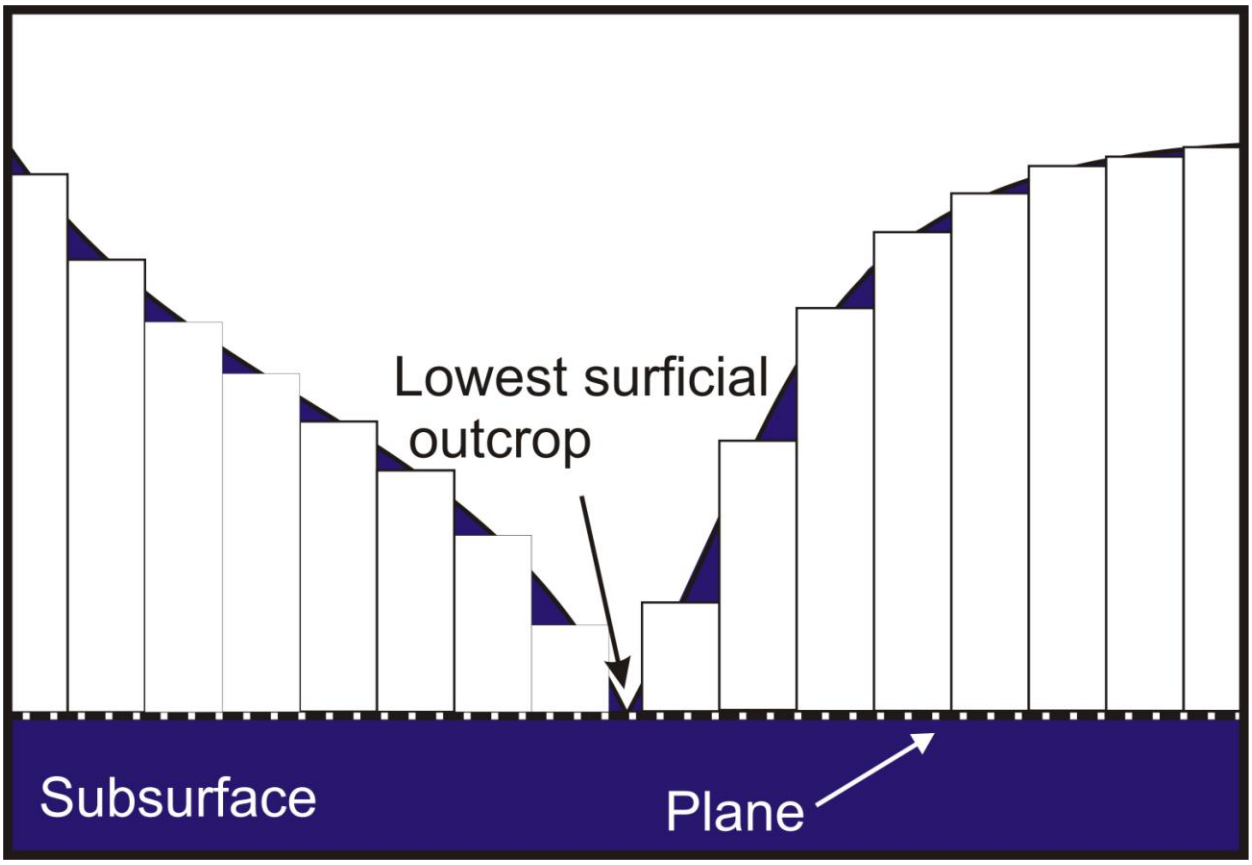

Figure 4: Generic cross section depicting portions of surface and subsurface included in cut and fill volume estimate method. Purple color represents all subsurface and solid black line indicates topographic surface. Plane arrow points to imaginary plane which volumes are calculated above; white columns indicates portion of ground and subsurface included in volume estimate. Purple color is not included in the calculation.

CHAPTER 3 - **FIELD RELATIONS**

The Jarbidge Rhyolite is several discrete bodies of coalesced rhyolite lava flows, domes, and pyroclastics (Coats, 1964 & 1987; Bernt, 1998; this study). The study focused on several JR bodies, and specific regions from each outcrop were sampled (Fig. 5).

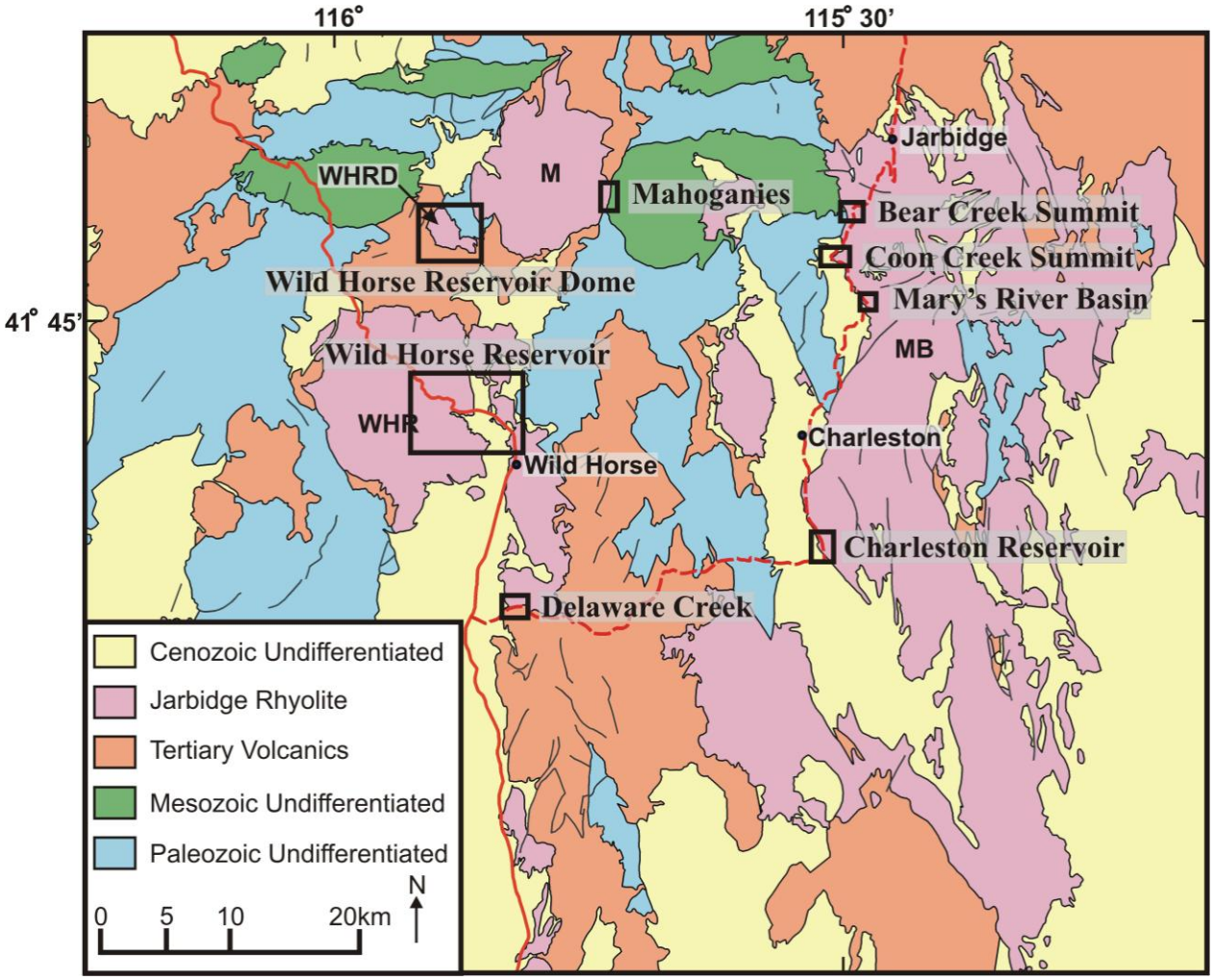

Figure 5: Black borders constrain the sampled locations, and adjacent names, in dark gray boxes, are the designated name for a sample location. Bear Creek Summit (BCS), Coon Creek Summit (CCS), Mary's River Basin (MRB), Charleston Reservoir (CR), Delaware (D; in text is grouped with Wild Horse Reservoir [WHR]), Wild Horse Reservoir Dome (WHRD), Mahoganies (M). BCS, CCS, MRB, CR are considered MB bodies, D and WHR are considered WHR bodies, WHRD is the WHRD outcrop, and M is the M outcrop.

The MB outcrop is the largest, with an approximate ArcGIS calculated area and volume of 949 km^2 and 405 km^3 (Table 1). This estimate is further supported by taking the average thickness of two unfaulted sample locations and multiplying by the area calculated using ArcGIS; which yields a volume of ~408 km^3. The approximate area and volume of erupted material is 232 km^2 and 66 km^3 for Wild Horse Reservoir, 101 km^2 and 37 km^3 for the Mahoganies, and 6.8 km^2 and 0.93 km^3 for the Wild Horse Reservoir dome (Table 1). Together these bodies come to a total approximate area and volume of 1,319 km^2 and 509 km^3. Area and volume was not calculated for the outcrop near Wells, NV.

Table 1: Summary of approximate area and erupted volume of JR bodies.

Location	Area (km^2)	Volume (km^3)
Main Body (MB)	949	405
Wild Horse Reservoir (WHR)	232	66
Mahoganies (M)	101	37
Wild Horse Reservoir Dome (WHRD)	6.8	0.93
Total	1,289	509

The interpretation of physical volcanology indicates that the JR observed during this study consist primarily of a series of thick rhyolite lava flows. Sampled packages vary in thickness from 61 - 485 m. Many packages contain multiple lava flows. Physical features include breccias, ramp structures, flow banding/folds (at hand and thin section scale), vitrophyre, sheet jointing, and internal massive portions of lava flow. Additionally, one vitrophyric neck was found.

Overall, the JR encountered lacks any indication of explosive eruptions, and lava flows were found overlying one another without pyroclastic material between them. Coats (1964) and Bernt (1998) report pyroclastic material in the JR formation from an area not sampled by this study. Given the large magnitude of lava erupted oogives may be expected, but are not observed in the study area. Erosion may have removed these surficial features.

Charleston Reservoir flows have very limited physical characteristics. A flow breccia, with oxidation staining contains clasts ranging from pebbles to boulders (Fig. 6). When viewed from a distance (Fig. 7) a lobate form is displayed, indicating this area is likely a flow margin.

The Mary's River Basin transect ascended through ~485 m of rhyolite. Spherodial weathering was observed at higher elevations along with vertical joints (Fig. 8). Nondescript stony rhyolite is common. However, a ~40-m-thick sequence of upper vitrophyric breccia, vitrophyre, stony rhyolite, and basal vitrophyre is found. The upper vitrophyric breccia (Fig. 9) consists of pebbles to boulders and overlies massive vitrophyre. These are believed to be associated with one another based on petrography and is discussed later. The massive vitrophyre overlies sheared stony rhyolite, which grades into a massive basal vitrophyre. Generally, vitrophyre has a trachytic texture, and ranges from glassy to devitrified.

Coon Creek Summit's (Fig.10) thickest portion is ~375 m. The only occurrence of flow banding is at CCS and this area is a possible eruptive center. The flow banding is on the centimeter scale (Fig. 11). Lower in the section, sheet jointing is obvious in the interior massive stony portion of flow. Three different vitrophyre outcrops are in this transect. Vitrophyre layers have vertical distances of ~30-120 m between stratigraphically higher or lower vitrophyre outcrops. Lower in the section, basal vitrophyre makes a convolute contact with interior stony rhyolite (Fig. 12). A jointed vitrophyre neck with near horizontal joints crops out at the base of the package (Fig. 13). Underlying the vitrophyric neck is a clast-supported breccia of devitrified vitrophyre and white matrix (Fig. 14).

Bear Creek Summit is a topographic saddle located between Coon Creek Summit and Deer Mountain. A ramp structure of alternating layers of devitrified vitrophyre and stony rhyolite is present on the south side of Deer Mountain (Fig. 15). The alternation occurs at the centimeter scale. Sheet jointing of stony rhyolite is observed in the thicker stony rhyolite portions. Vitrophyre in this area displays internal shearing, a flow foliation.

The Mahoganies outcrop also lacks evidence of pyroclastic activity. The sampled areas appear as massive stony interiors with underlying basal vitrophyre (Fig. 16). The Wild Horse Reservoir, and Wild Horse Dome areas sampled are non-descript, consisting of thick stony rhyolite (Fig. 17 & 18).

Figure 6: Oxidized flow breccia located south of Charleston. A 55 cm long rock hammer serves as scale.

Figure 7: Yellow line traces the contact of a Jarbidge Rhyolite flow margin and sedimentary strata south of Charleston. Photograph taken approximately 1.5 km southwest of margin, view is to the northeast.

Figure 8: Vertical joints in peak 8627, Mary's River Basin NW 7.5' USGS quadrangle. Yellow lines in lower left corner indicate joint dip direction. Photograph was taken from ~1 km north-northeast with 3x zoom power. Trees are ~2-3m tall. This area may be an eruptive center.

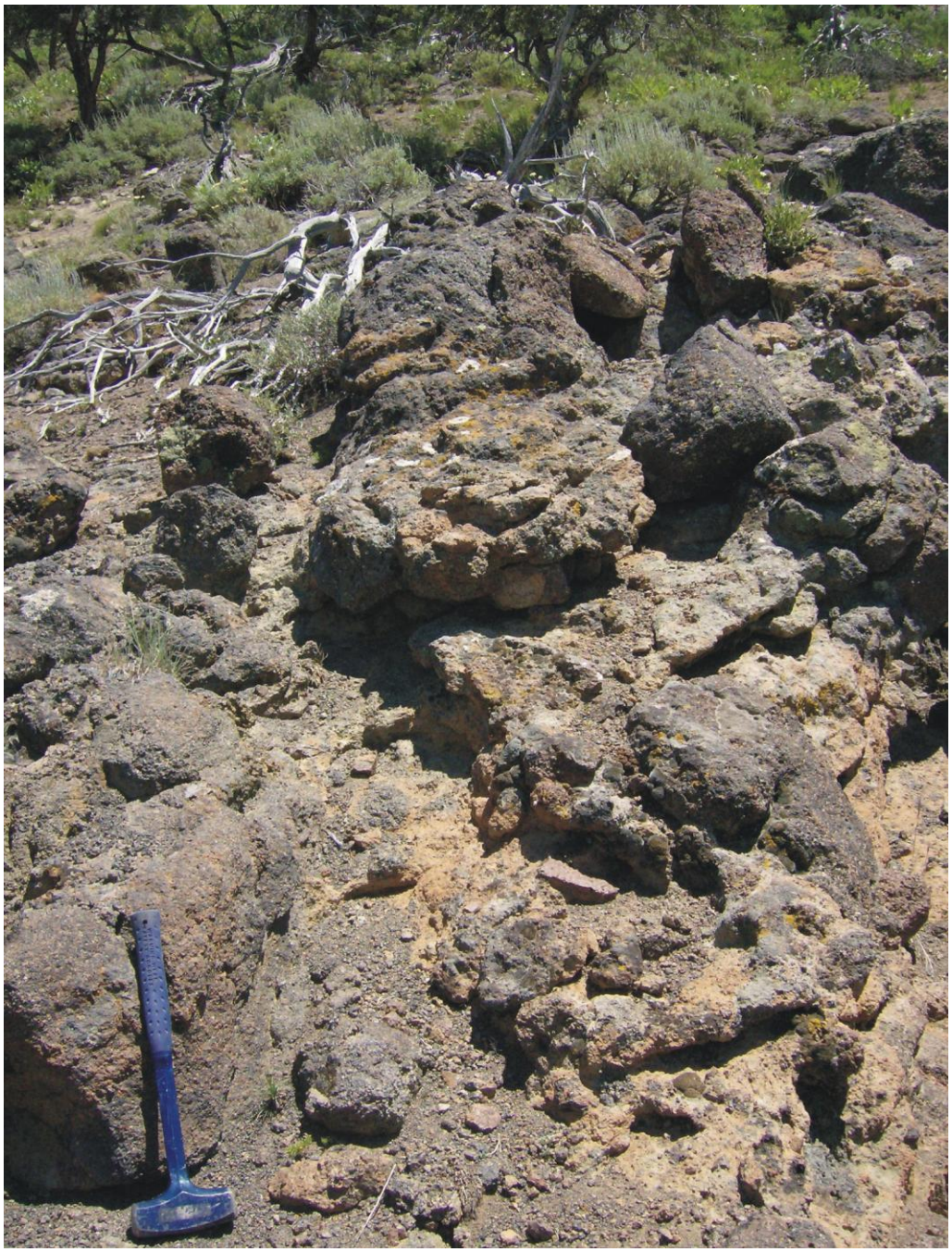

Figure 9: Upper vitrophyric breccia with a ~40 cm hammer for scale. Photograph is taken from Mary's River Basin transect.

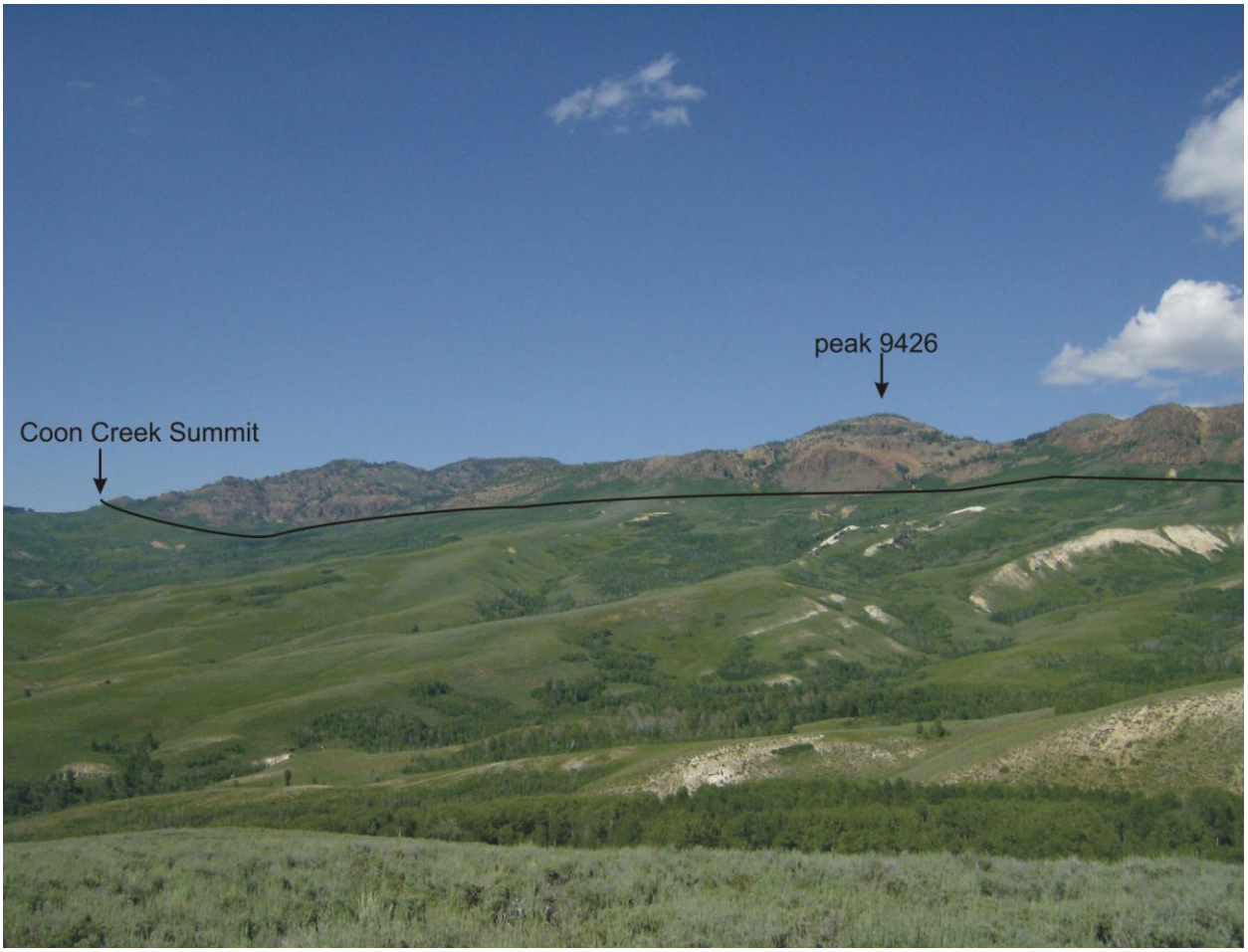

Figure 10: View of Coon Creek Summit and adjacent area from ~4.75 km south. Coon Creek Summit and peak 9426 are ~1.3 km from one another with ~300 m of vertical relief. Black line is the approximate contact between Jarbidge Rhyolite and underlying Eocene ash flow tuffs and sedimentary strata.

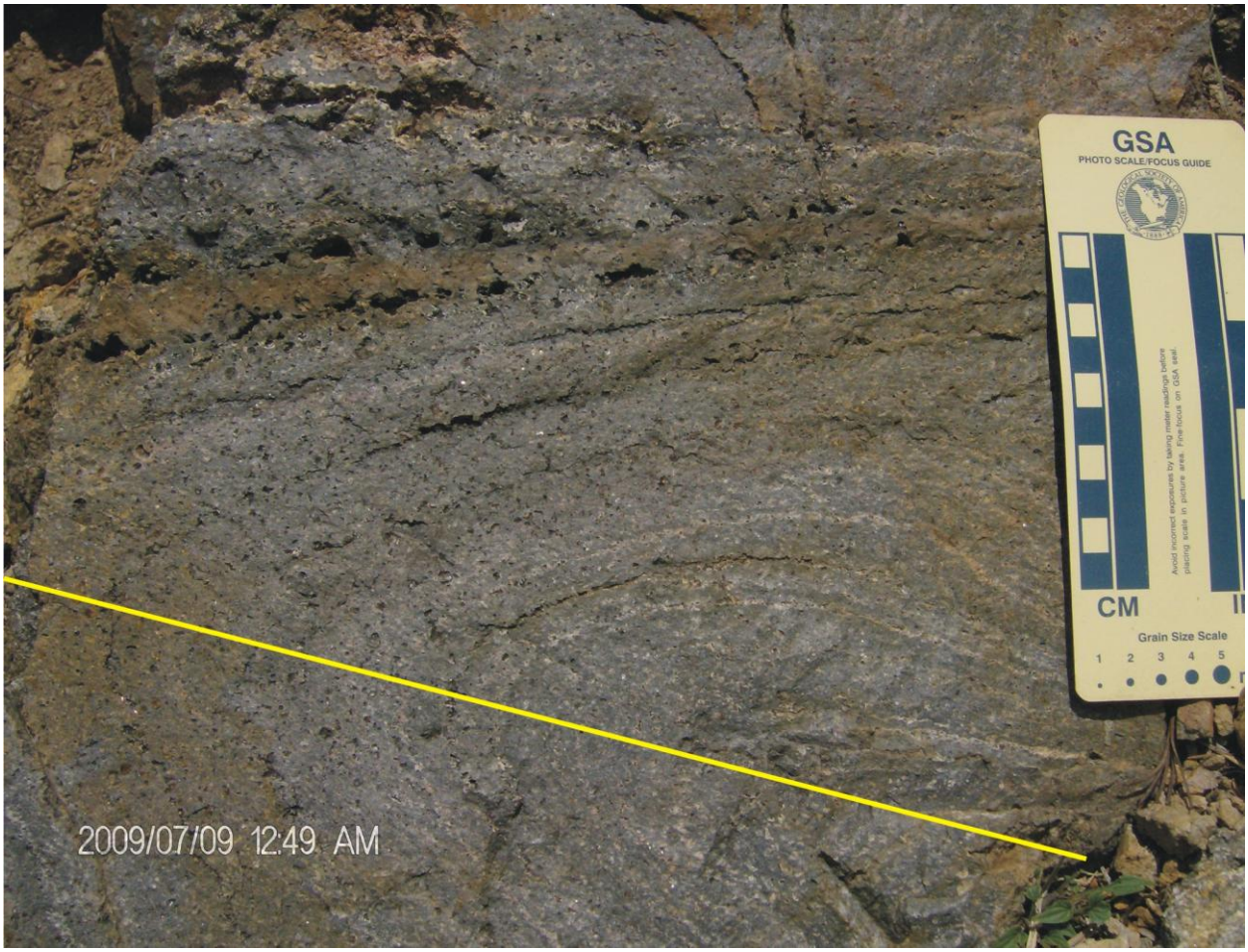

Figure 11: Yellow line approximates the axial plane of the flow fold in JR from Coon Creek Summit.

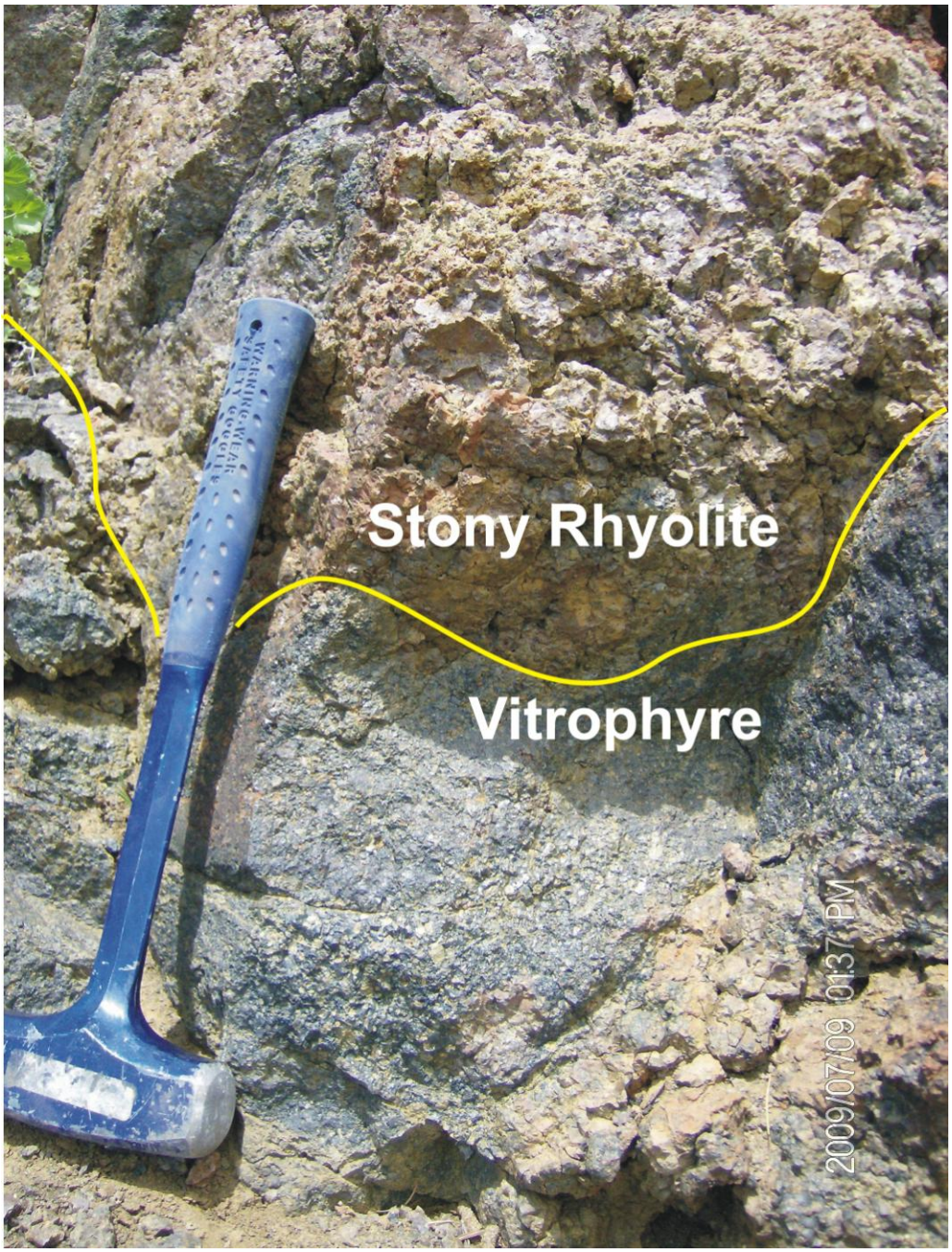

Figure 12: Convolute contact between basal vitrophyre and stony rhyolite with ~40 cm long rock hammer for scale. Yellow line follows approximate transition of vitrophyre to stony rhyolite in Coon Creek Summit outcrop.

Figure 13: Jointed vitrophyric neck in Coon Creek Summit transect; possible eroded neck or plug.

Figure 14: Photograph is taken south of Coon Creek Summit transect. Yellow lines approximate dip direction. Joints outcrop over an estimated 10 m of vertical relief. Underlying breccia is devitrified rhyolite and ashy material.

Figure 15: Ramp structure, "root less" dikes, located on south slope of Deer Mountain. Alternating bands of vitrophyre and stony rhyolite are indicated by arrows and text. Stony rhyolite appears reddish and vitrophyre as dull black.

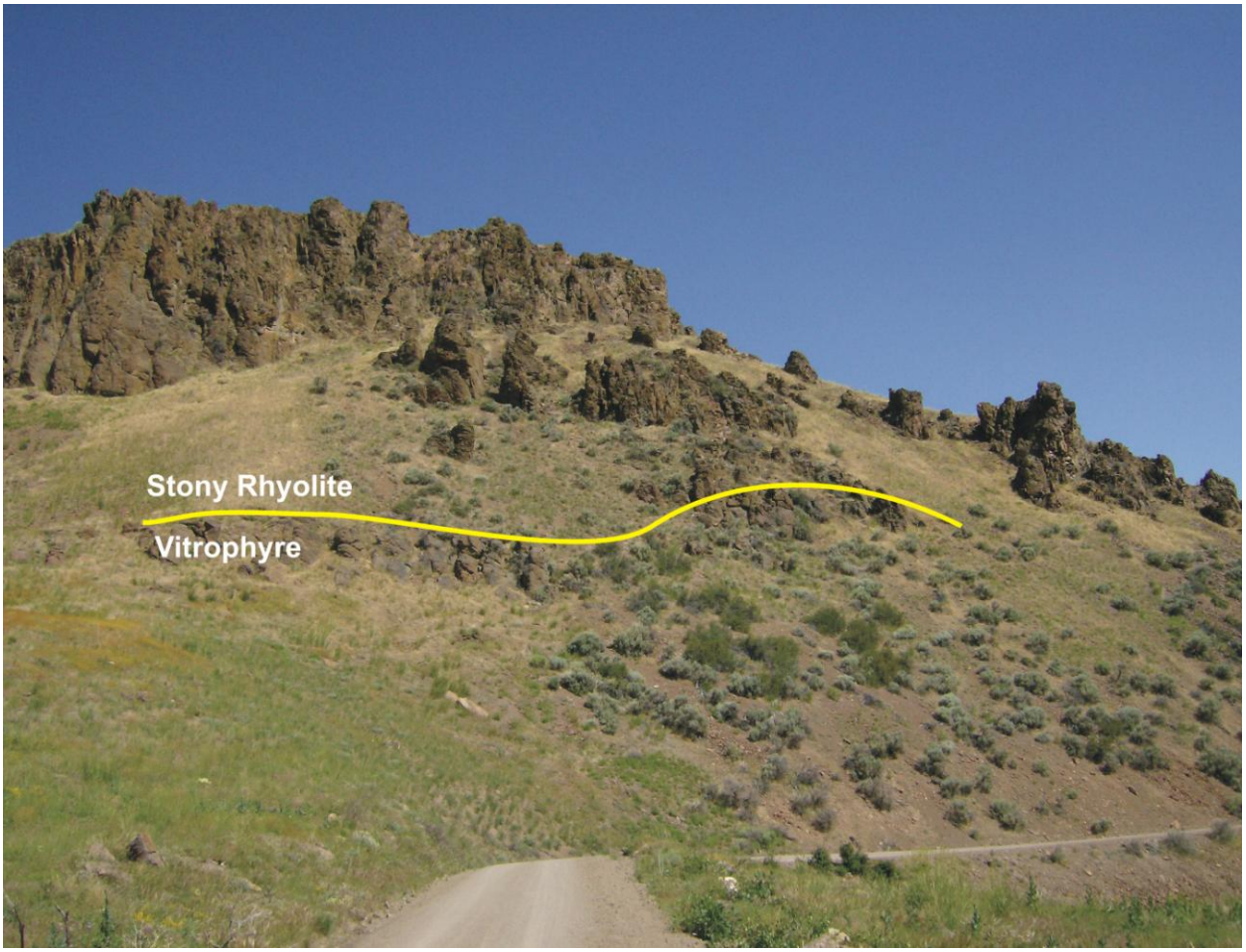

Figure 16: Yellow line indicates approximate contact of vitrophyre and stony rhyolite in Mahoganies outcrop. Photograph was taken several hundred meters south of slope. Outcrop relief is approximately 61 m from road to highest elevation.

Figure 17: Wild Horse Reservoir outcrop approximately 85 m thick from road to crest. Photograph was taken from 0.25 km to the southeast.

Figure 18: View of Wild Horse Reservoir Dome outcrop. Picture was taken from ~3 km northwest of outcrop. The outcrop is approximately 200 m thick. Yellow line approximates the contact of JR and underlying sedimentary strata.

CHAPTER 4 - **PETROGRAPHY**

Appendix A includes UTM coordinates and field notes of collection areas, petrographic description of samples, and point counted modes for representative samples. In hand sample, the JR is smoky quartz-phyric. Phenocrysts abundances approximately range from 15-40 %, and eleven point counted samples yield an average phenocrysts abundance of ~30 % by volume. Smoky quartz crystals are fractured and several mm in diameter; however, several samples contain crystals upward of ~1 cm. Sanidine crystals typically display a euhedral habit and a few samples contain seriticizied sanidine crystals. Crystal sizes range from 1 to an observed maximum of 12 mm. Plagioclase crystals are less, if not as common as sanidine, and are typically seriticized. Plagioclase crystals typically cover the same size range as sanidine; however, one sample, JC-09-21b, displays several plagioclase crystals as large as 2.2 cm. Additionally, a single plagioclase crystal 3.8 cm in the longest dimension was found in a JR lava flow (Fig. 19A). The flow bearing this crystal is proximal to the Seventy Six basalt in Copper Basin, which contains similar sized plagioclase crystals (Fig. 19B). Open-system textures in feldspars may be seen by the naked eye in several samples from CCS.

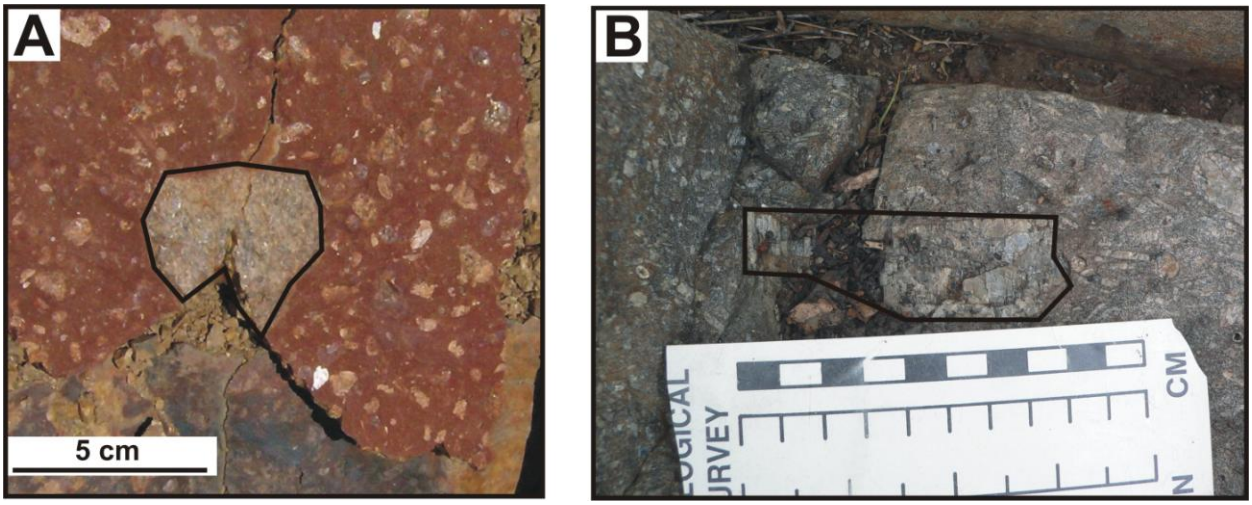

Figure 19: A) Plagioclase xenocryst 3.8 cm in longest dimension found in the JR lava flow. B) Plagioclase crystal in Seventy Six basalt, Copper Basin.

In thin section, JR samples are holocrystalline to hypocrystalline. Vitrophyre groundmasses vary from glassy to devitrified and commonly display perlitic fracture.

Vitrophyre samples commonly have a higher proportion of mafic minerals than the stony rhyolite. Stony rhyolite groundmass is commonly devitrified with microcrystalline feldspar laths. Flow banded glass (Fig. 20A), flow-aligned oxides, and pilotaxitic and trachytic texture (Fig. 20B) are present in several samples.

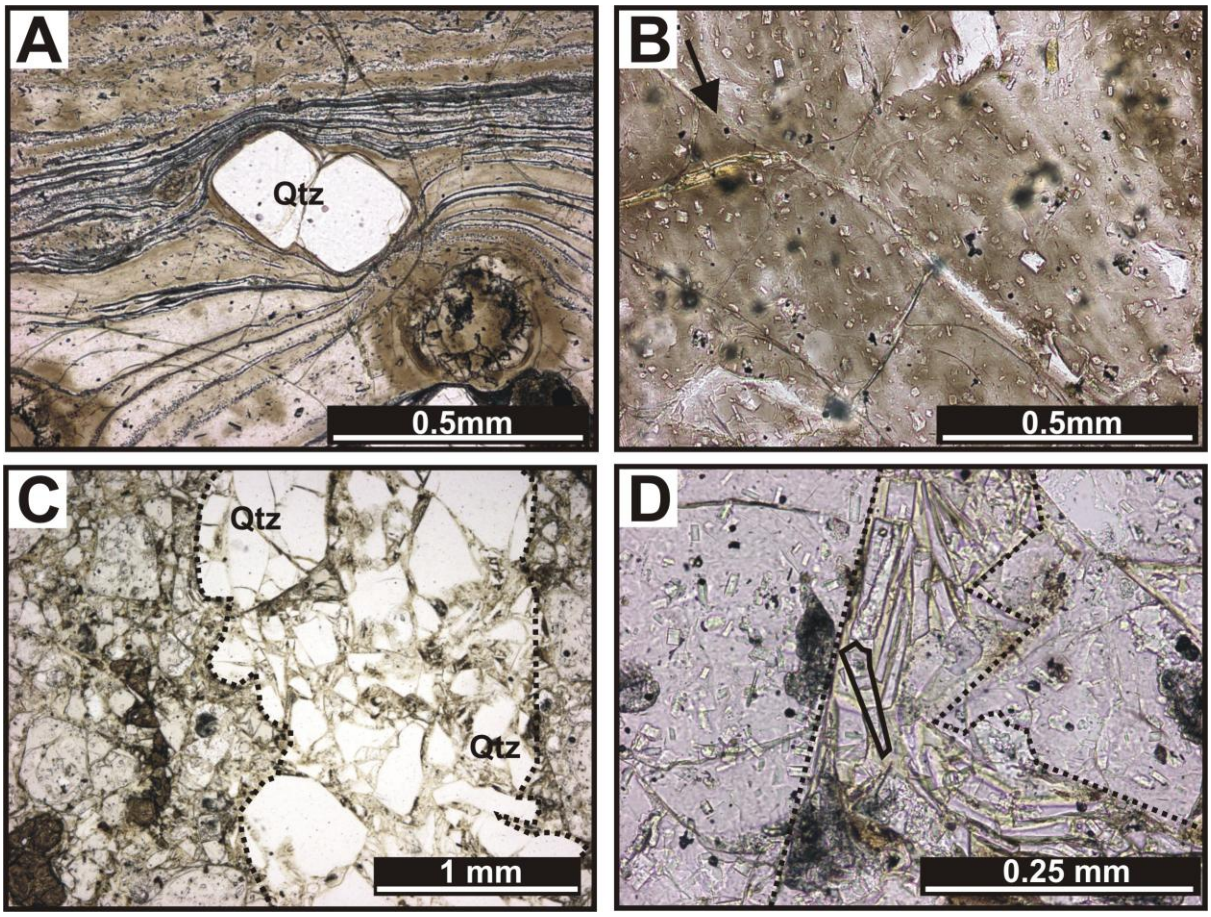

Figure 20: A) Flow-banded glass, black bands, and quartz phenocryst in plane polarized light (PPL). B) Pilotaxitic groundmass in vitrophyre in PPL. Arrow approximates flow foliation. C) Upper vitrophyre breccia in PPL. A disarticulated, but only partly displaced, quartz crystal is found between the two dashed lines, and pilotaxitic vitrophyre is found outside them. Abbreviation Qtz=quartz. D) Crystal chips infilling space between vitrophyre clast in PPL. Dotted lines trace clast boundaries and chips fill area between clasts/dotted lines. One chip is outlined in black, and several additional chips are found above, and down and to the right from this chip.

In thin section, the upper vitrophyre of MRB is clast supported. Clasts are vitrophyre with pilotaxitic texture and seriate crystals (Fig. 20C). Fractured crystals are found filling void

space between vitrophyre clasts (Fig. 20D). No concentric oxide shells, as described by Manley (1996), were found. This sample comes from a transitional area between dense and brecciated vitrophyre; hence, the sampled zone may not have been vesciculated enough to form pumice or made contact with the atmosphere. The underlying massive vitrophyre, and basal vitrophyre of this flow also displays pilotaxitic texture and similar mineralogy; together these define one flow.

Phenocryst phases in the JR are quartz, sanidine, plagioclase, Fe-Ti oxides, ± clinopyroxene, ± biotite, ± hornblende, ± oxyhornblende, zircon, and ± apatite (Fig. 21). Quartz,

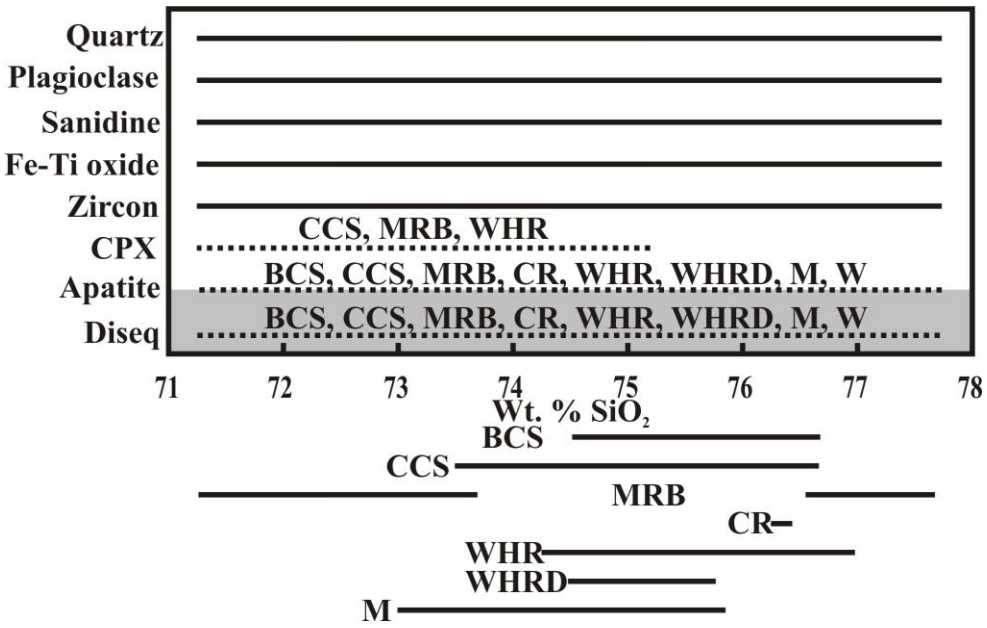

Figure 21: Primary mineral occurrences across SiO_2 wt. % range. Black lines indicate that the phase is found in all thin sections from this study. Dashed line indicates that mineral is intermittently found and abbreviations above dashed lines indicate what sample locations contain the mineral. Abbreviations are CPX= clinopyroxene, Diseq= disequilibrium textures, BCS= Bear Creek Summit, CCS= Coon Creek Summit, MRB= Mary's River Basin, CR= Charleston Reservoir, WHR= Wild Horse Reservoir, WHRD= Wild Horse Reservoir Dome, M=Mahoganies. Gray field denotes area of textures. The solid lines under the box indicate the wt. % SiO_2 displayed by each outcrop.

sanidine, and plagioclase are the major primary phases, and 11 point counted samples yield average modal abundances in % by volume for quartz (11.2), sanidine (9.6), and plagioclase (7.0). The point counted samples reveal transitions between relative quantities of major phases with increasing wt. % SiO_2. The most abundant major rock forming mineral transitions from plagioclase to sanidine to quartz as wt. % SiO_2 increases. Anhydrous mineral assemblages are

typical and open-system textures are common; and the degree of open system processes varies between samples.

In thin section, quartz crystals are euhedral-anhedral, varying in size from microcrystalline to 5.4 mm. Modally, quartz varies from 4.4 - 16.7 % by volume. Quartz textures include embayments (Fig. 22A), ocelli (Fig. 22B), chessboard extinction, broken crystals whose faces could fit together like jigsaw puzzle pieces (Fig. 20C), and granophyre and graphic granite textures (Fig. 23F). Independent crystals may be linked by crystallographic orientations, indicating that these now separate crystals are structurally connected.

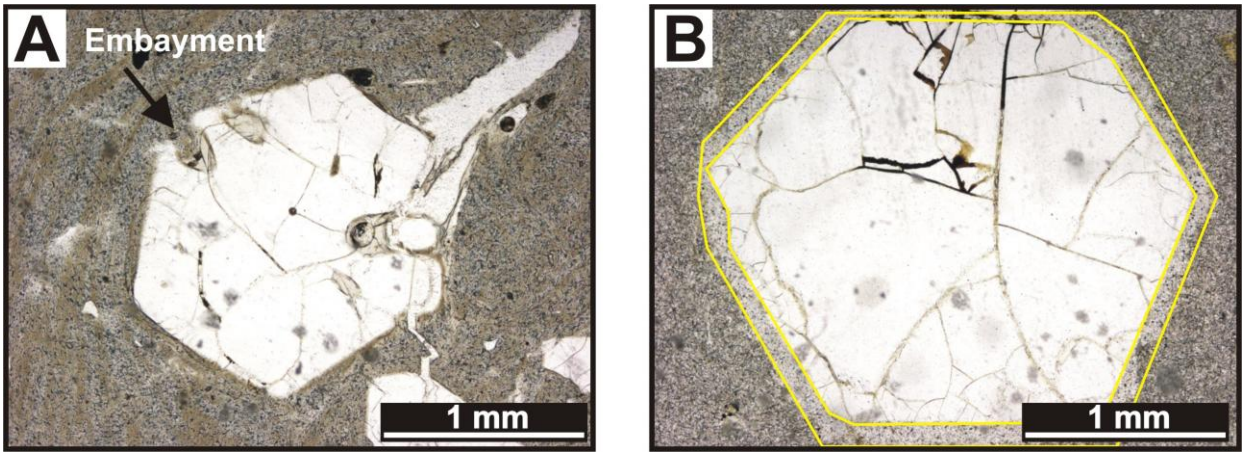

Figure 22: A) Embayed quartz in flow banded groundmass in PPL. B) Yellow lines "box" the quartz ocelli surrounding the crystal in PPL.

Sanidine displays simple or no twins. Those samples without twinning are determined to be sanidine based on their 2V angle and optic axis figures. Modally, sanidine's abundance varies from 1.6 to 16.5% by volume. Sanidine is commonly anhedral-subhedral, displaying embayments, anti-rapakivi (Fig. 23A), skeletal (Fig. 23B), spongy, inclusion rims (Fig 23C) and boxy textures. Skeletal sanidine is intergrown with skeletal plagioclase in several samples (Fig. 23B). Crystallographically controlled square glass reentrants (Fig. 23D) and plagioclase

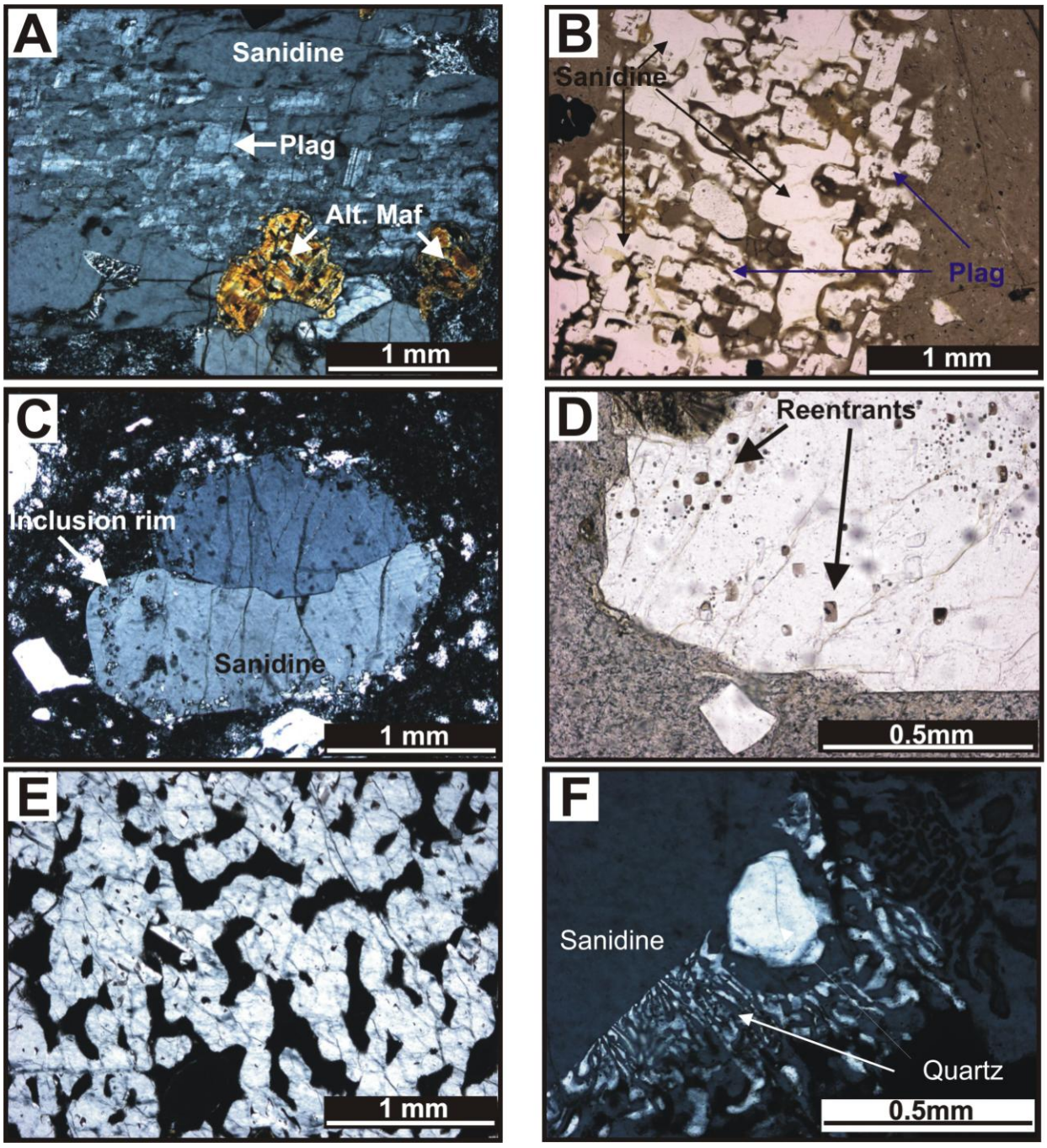

Figure 23: Photomicrographs of open system textures. A) A clot of sanidine, plagioclase and altered mafics in crossed polarized light (XPL). B) Extensively resorbed plagioclase and sanidine PPL. C) Inclusion rim in sanidine in XPL. D) Glass reentrants in PPL. E) Spongy plagioclase, view is of one crystal and glass groundmass in XPL. F) Graphic granite texture in XPL.

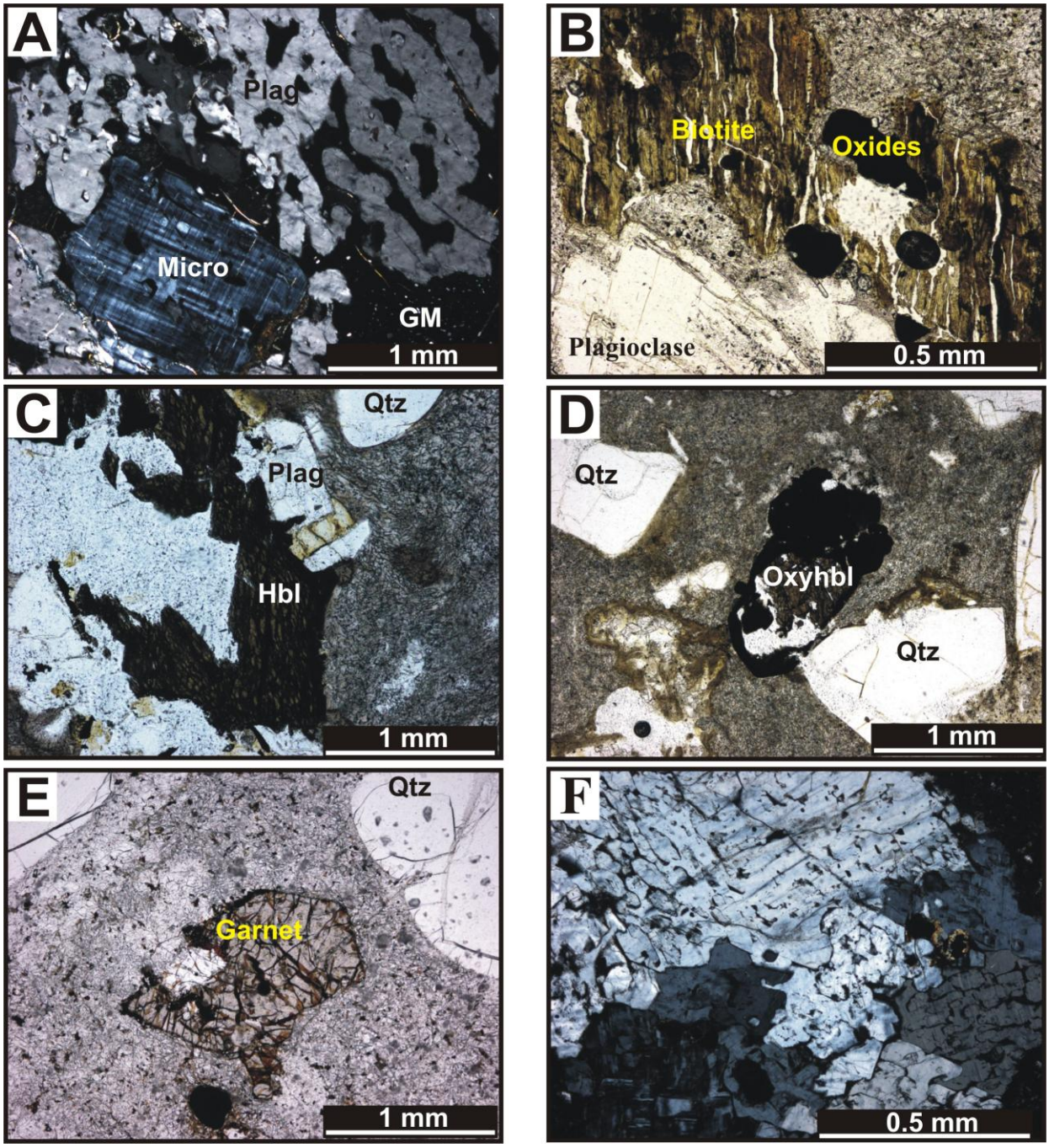

Figure 24: A) Xenocrystic clot of microcline (Micro) and plagioclase (Plag) in XPL. B) Xenocrystic biotite with oxide inclusions in PPL. C) Clot of hornblende (Hbl), and plagioclase in PPL. D) Oxyhornblende (Oxyhbl) in PPL. E) Garnet xenocryst in PPL. F) Xenocrystic clot of plagioclase crystals in XPL.

inclusions occur in some sanidine crystals. Groundmass sanidine displays a pilotaxitic texture (Fig. 20B). Plagioclase is anhedral-subhedral and modally varies from 2.5-14.1% by volume. Textures include skeletal, embayed, boxy and spongy crystals (Fig. 23E). Their compositional

range is An_{10-40}, as determined by the Michel-Levy technique. Plagioclase clots are common and typically include zircon, apatite, Fe-Ti oxides, pyroxenes and altered mafic phases.

Clinopyroxene, characterized by inclined extinction, high interference colors and optic axis figures, has euhedral-anhedral form. It occurs as independent phases in groundmass and in glomeroporphyritic clots with plagioclase, microcline, oxides, and itself. The only noted inclusion is apatite. Oxide phases include both magnetite and ilmenite, based on prismatic habits. Sizes vary from groundmass, to several mm. Apatite occurs as an inclusion phase, and some oxides display disequilibrium with melt (embayments and reentrants).

Accessory phases include zircon, and apatite. Zircon is ubiquitous. It occurs as independent crystals, within plagioclase clots, in groundmass and as inclusions in clots and biotite. Apatite's form is euhedral needles through anhedral fractured crystals, and occurs as inclusions in feldspar and biotite, in clots, and groundmass. Apatite is found in all samples but one from BCS.

A xenolith was found in the Seventy Six basalt, and in thin section it is enclave is seriate, with quartz, sanidine, plagioclase, zircon and Fe-Ti oxide microphenocryst. All phases are anhedral and the groundmass is cryptocrystalline. A silicic clot of polygonal quartz and feldspar (?) is present.

The basalts are holocrystalline. Phenocryst phases are plagioclase, titanaugite, and olivine. Plagioclase compositions of larger component crystals range An_{40-64}, and resorbed crystals have compositions near An_{35}. The largest and midsized crystals may be sieved, where as the groundmass population is sub-euhedral and has an ophitic texture. A xenocryst consisting of quartz, feldspar, and orthopyroxene is noted. The xenocryst is composed of anhedral crystals, some of which display open system textures. Glass is found between grains.

Xenocrysts, Xenocryst Clots and Weathering Products

Xenocrystic microcline is in several samples from the BCS, CCS, and MRB and one instance is reported for WHR (Fig. 25). It is present in two point counted samples and the modal percentages are 0.6 and 4.5 by volume. Crystals are anhedral, skeletal, embayed, boxy, display tartan twinning, occur in clots (Fig. 24A) and one crystal displays rapakivi texture. Additionally, the microcline displays salient characteristics that microcline from the local Cretaceous granitoid, Coffee Pot Stock, exhibits. Biotite is present in CCS, MRB and WHR samples. The

crystals are altering to chlorite, resulting in kata-alteromoprhs (Fig. 24B). Oxidized bands cross open sections of the minerals, indicating a volume change. Xenocrystic clots of microcline, biotite, plagioclase, zircon, apatite, and Fe-Ti oxides are present. Iron oxides, apatite, and zircon occur as inclusions within biotite crystals, biotite occasionally occurs as an inclusion in plagioclase, and it occurs as an independent crystal. Biotite also has salient characteristics of biotite within the Coffee Pot Stock.

Hornblende and oxyhornblende occur within the same sample, JC-08-25 (from WHRD). Hornblende appears xenocrystic in origin given the solid grain-grain contacts with several minerals (Fig. 24C). Oxyhornblende displays grain edges that have altered to more competent oxides (Fig. 24D). In the same sample oxides with plucked cores occur and are inferred to be oxyhornblende. Serpentinized olivine is in a WHR vitrophyre sample. Primary features are replaced and the primary mineral is inferred to be olivine based on fractures and association of minerals. The serpentinized olivine occurs in a plagioclase clot.

Two Jarbidge Rhyolite samples, CR and W, contain garnet. It is isotropic with high relief and internal fractures (Fig. 24E). The crystals are rounded and occur as inclusions in feldspar, and glomeroporphyritic plagioclase-garnet clots.

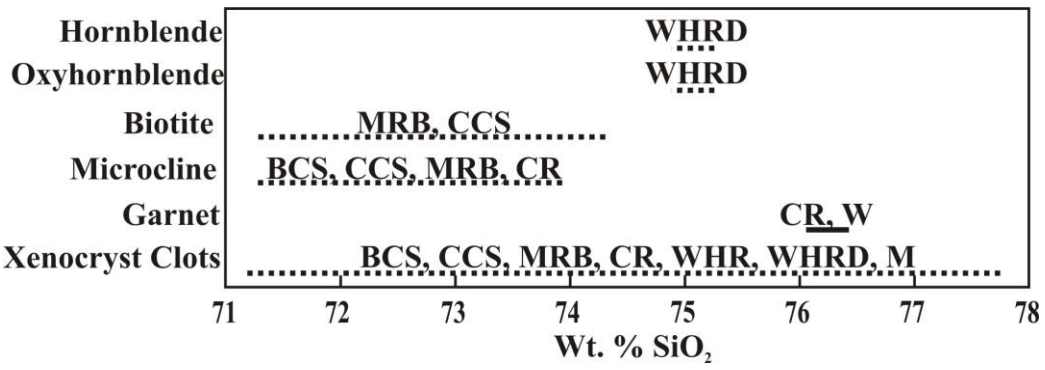

Figure 25: Initials above line indicate the location of the xenocryst-bearing sample is from. Dashed line indicates that xenocryst is not found in all samples from listed sample location(s) and solid line indicates xenocryst is found in all samples from listed location(s). Length of line indicates range in wt. % SiO_2 the xenocryst is found over.

Xenocryst clots (Fig. 24F) are numerous, occurring in many of the samples. The clots are believed to be xenocrystic because they do not have euhedral crystal faces that protrude into the groundmass (Seaman, 2000) and crystals within the clots have solid grain boundaries (Bachman

et al., 2002). Plagioclase, microcline, biotite, and Fe-Ti oxides constitute clots. Some xenocrystic clots are composed solely of plagioclase. Feldspars within the xenocryst clots have solid grain-to-grain boundaries and some have lenses of melt between crystal faces.

CHAPTER 5 - **GEOCHEMISTRY**

Major and selected trace elements analyses were obtained on 27 Jarbidge Rhyolite samples, five Seventy Six basalt samples, and the Seventy Six basalt xenocryst sample. Ten rhyolites, two basalts (one from Copper Basin [CB] and one from Sunflower reservoir [SR] area), and the xenolith were analyzed for a suite of trace and rare earth elements. Major elements are reported in weight percent (wt. %) oxide and trace and rare earth elements are reported in parts per million (ppm).

Major Element Geochemistry

On the total alkali silica (TAS) diagram of LeBas et al. (1986), JR plots as rhyolite, the Seventy Six basalt xenocryst plots as andesite, Seventy Six Basalt CB plots as trachybasalt, and Seventy Six basalt SR plot as basalt (Fig. 26).

The JR is meta- to slightly peraluminous, having an alumina saturation index (ASI) of 0.95 through 1.15 (Fig. 27 A), and a mean ASI of 1.02. The ASI increases with increasing SiO_2 (Fig. 27 B). JR is ferroan according to the definitions of Frost et al. (2001), having an Fe# = ~0.95-0.99 with an average Fe#=0.96 (FeO# = $FeO^{tot}/(FeO^{tot}+MgO)$. Some samples have low temperature hydrothermal alteration as indicated by K_2O/Na_2O ratios that increase with LOI (Fig. 27 C). On the modified alkali lime index (MALI) plot of Frost et al. (2001) the rhyolite samples dominantly plot as calc-alkalic with a few alkali-calcic samples (Fig. 27 D). This plot only applies to those samples with less than 75 wt. % SiO_2, given Frost's projected divisions end.

Generally, the rhyolites are silica rich having wt. % SiO_2 = 71.5-77.8, with an average of 75.1. FeO*, TiO_2, CaO, P_2O_5, MnO, Al_2O_3 and MgO display an inverse relationship with wt. % SiO_2 (Fig. 28). Overall, the JR has salient characteristics of A-type magmatism such as high average wt. % SiO_2 (75.13), Fe# (0.96), and TiO_2/MgO (8.24).

Sampled basalts plot as tholeiitic on Miyashrio's (1974) FeO*/MgO vs. SiO_2 diagram. The Seventy Six basalt has $Na_2O > K_2O$ for both CB and SR. Seventy Six basalt K/P ratios range ~5.2-6.1 for CB and 4.8-5.1 for SR. The K/P ratio is an indicator of crustal contamination, and ratios of uncontaminated mantle derived magma will not be > 3.5 (Basaltic Volcanism Study Project, 1981). The basalts have low wt. % TiO_2 (1.82-1.90). The Seventy Six basalt CB has

higher wt. % CaO, Al_2O_3, Na_2O, and K_2O than the Seventy Six basalt SF. Seventy Six basalt samples have major element geochemistry similar to Steens basalt.

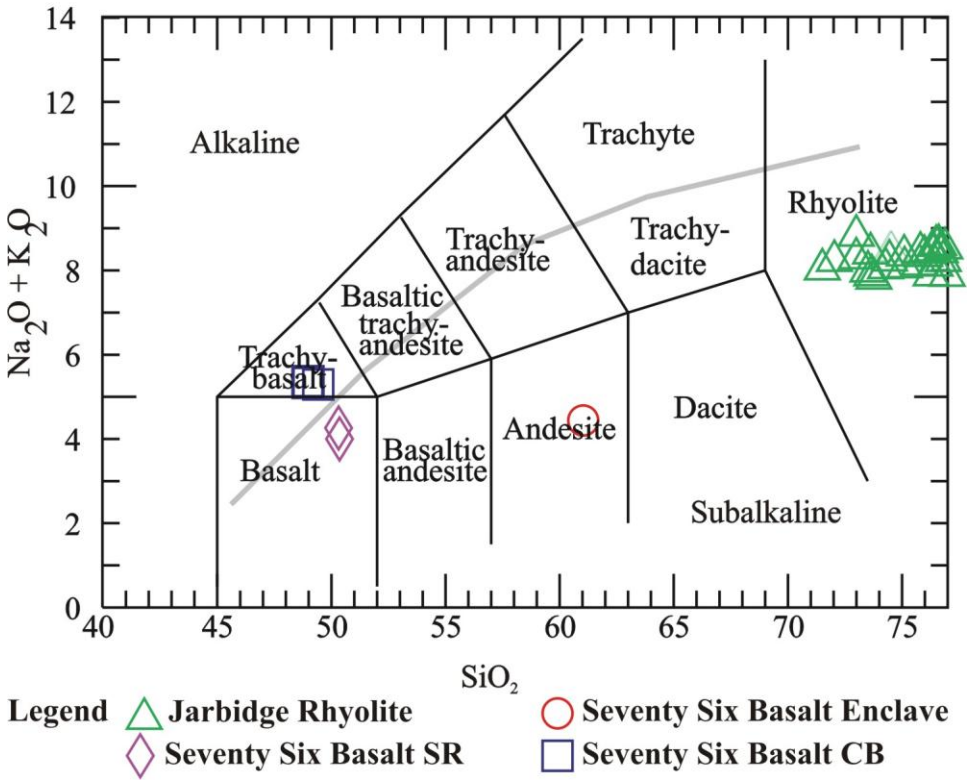

Figure 26: TAS diagram of LeBas et al. (1986). The samples plot as rhyolite for Jarbidge Rhyolite, basalt for Seventy Six Basalt SR, trachybasalt for Seventy Six basalt CB, and andesite for the Seventy Six basalt xenolith.

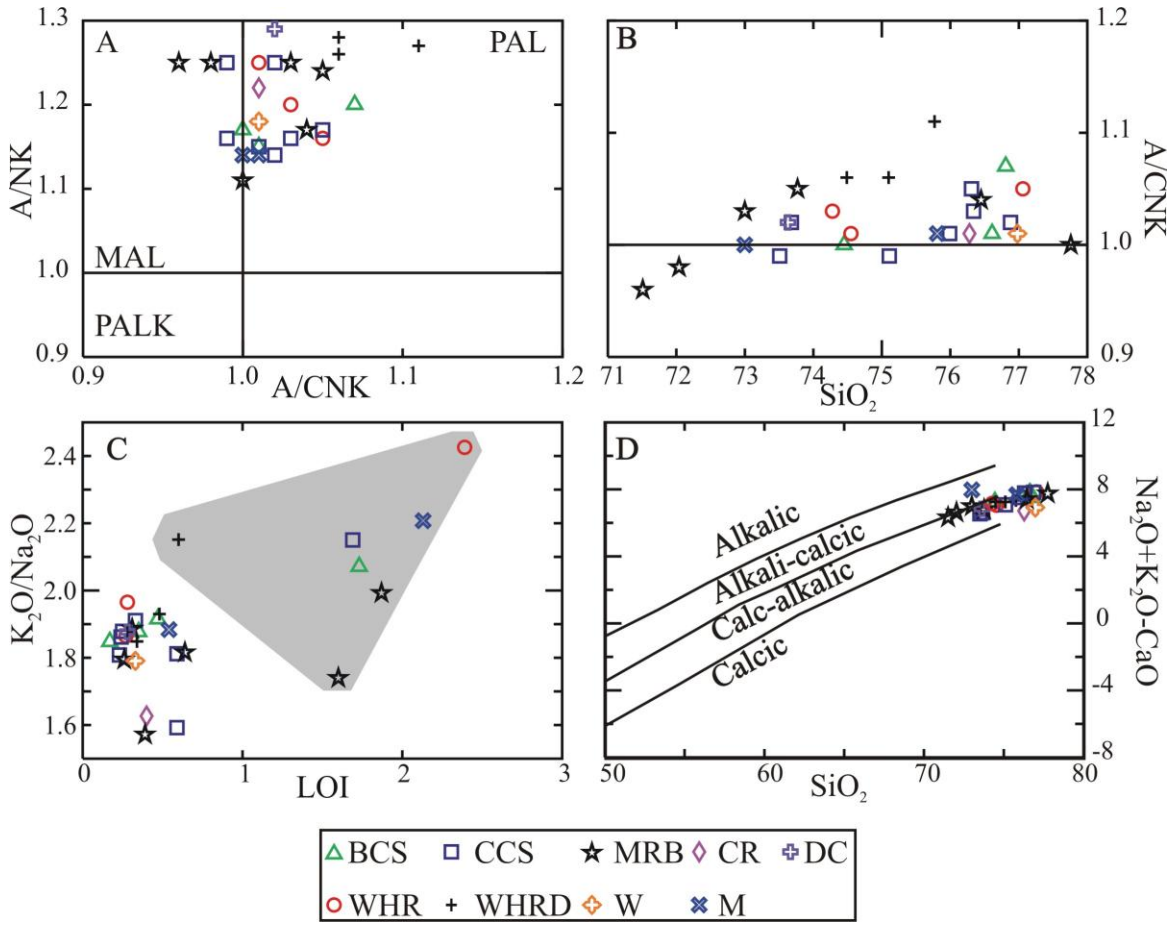

Figure 27: A) ASI plot. Abbreviations are PALK= peralkaline field, MAL= metaluminous field, and PAL= peraluminous field. B) Diagram depicting ASI increase with increasing wt. % SiO_2. A/CNK>1 is peraluminous. C) Low temperature hydration alteration plot. Samples within grey field have a linear trend with LOI, which is likely the result of low temperature hydration. D) Modified alkali index of Frost et al. (2001) depicting JR samples dominantly as calc-alkalic with minor alkali-calcic samples. These divisions only apply to those samples with less than 75 wt. % SiO_2 (Frost et al., 2001).

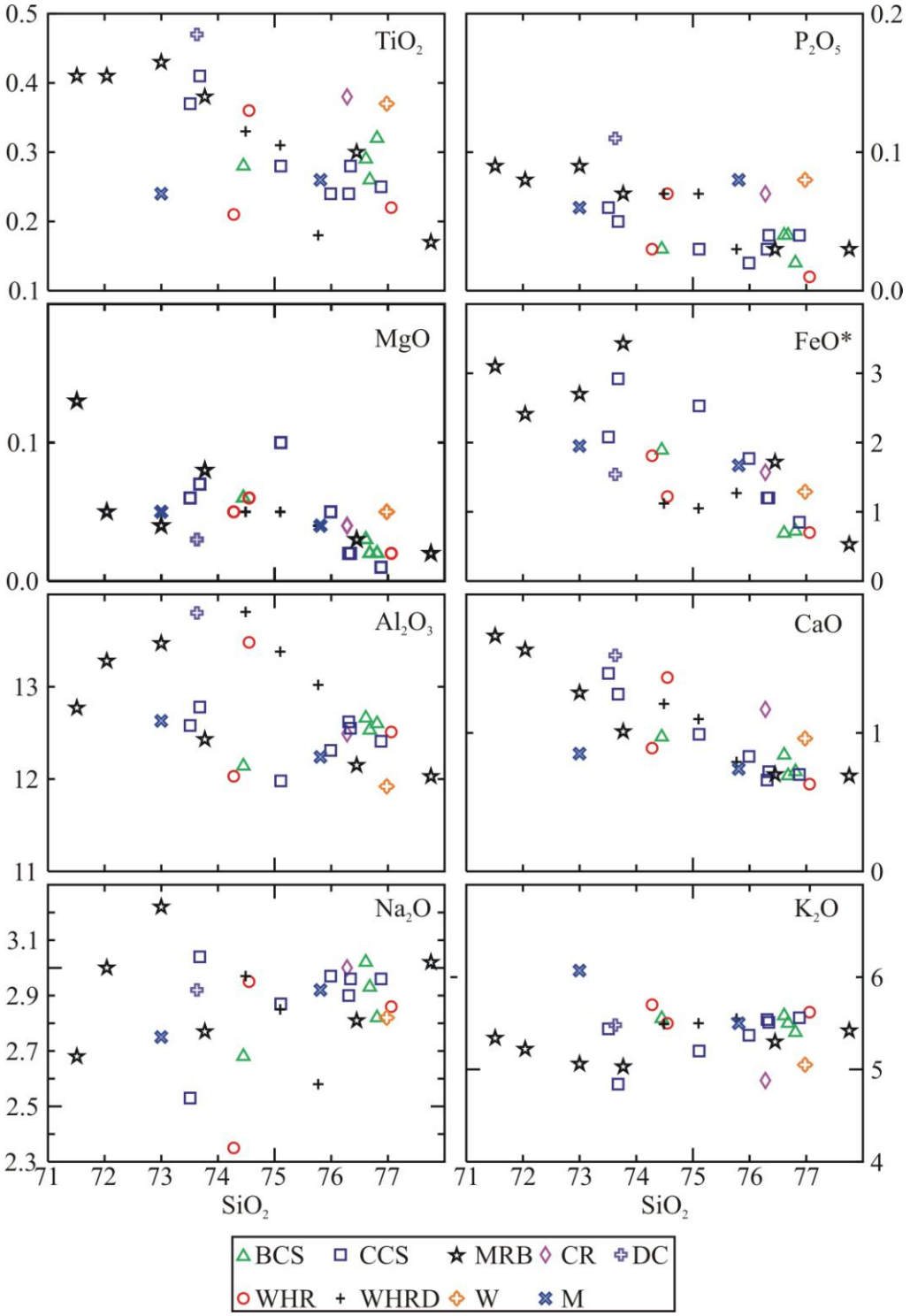

Figure 28: Harker diagrams with major oxide identified in upper right corner of diagram. Symbols are organized according to geography and consistent with text abbreviations, however DC is distinguished from WHR. TiO_2, P_2O_5, MgO, and FeO* behave compatibly, Na_2O displays how sample converge at higher Na_2O with increasing wt. % SiO_2, and K_2O displays its constant concentration range.

Trace Element Geochemistry

Trace elements in JR that display negative correlation with SiO_2 are Ba, Sr, Sc (Fig. 29) and Cu, and the only trace element that displays a positive correlation with SiO_2 is Rb (Fig. 29). The remaining trace elements, Nb (Fig. 29), V, Cr, Co, Ni, Y, Zr and Zn are invariant with respect to SiO_2.

Barium displays the widest range of concentrations (389-2715 ppm) among any trace element. Samples from the same transcet display Ba concentrations varying by as much as 2,000 ppm (Fig. 29). When plotted against Sr, two groups, one high Ba and Sr and one low Ba and Sr, become evident. On the Rb vs. Nb+Y diagram of Pearce et al. (1984) JR dominantly plot in the within plate granite field.

Trace element plots discriminate between flows. Plotting Ba/Rb or Sr/Rb vs. Rb separates the vitrophyre-stony rhyolite-vitrophyre samples from MRB from the other JR samples. Crustal contribution in a rhyolite may be evaluated by Rb/Nb and La/Nb ratios (Pearce et al., 1984). Rb/Nb ratios of the Jarbidge Rhyolite have a mean with standard deviation of 8.33±1.76 and La/Nb ratio is 4.05±0.71. Incompatible trace element ratios, Nb/Y, Rb/Y, and Rb/Nb, ranges overlap between sample locations.

Chemical stratigraphy is apparent within two transects. CCS displays concentration increases of SiO_2, and Rb and decreases of MgO, CaO, FeO*, TiO_2, Ba, and Sr with increasing elevation until mid elevation. Then the trends reverse. MRB displays the same relationships for the same elements.

The Seventy Six basalt samples fall within the compositional range of accepted Steens basalt (Johnson et al., 1998) on the modified MORB diagram (Fig. 30; Pearce, 1983). The Seventy Six basalt xenolith is enriched in incompatible elements.

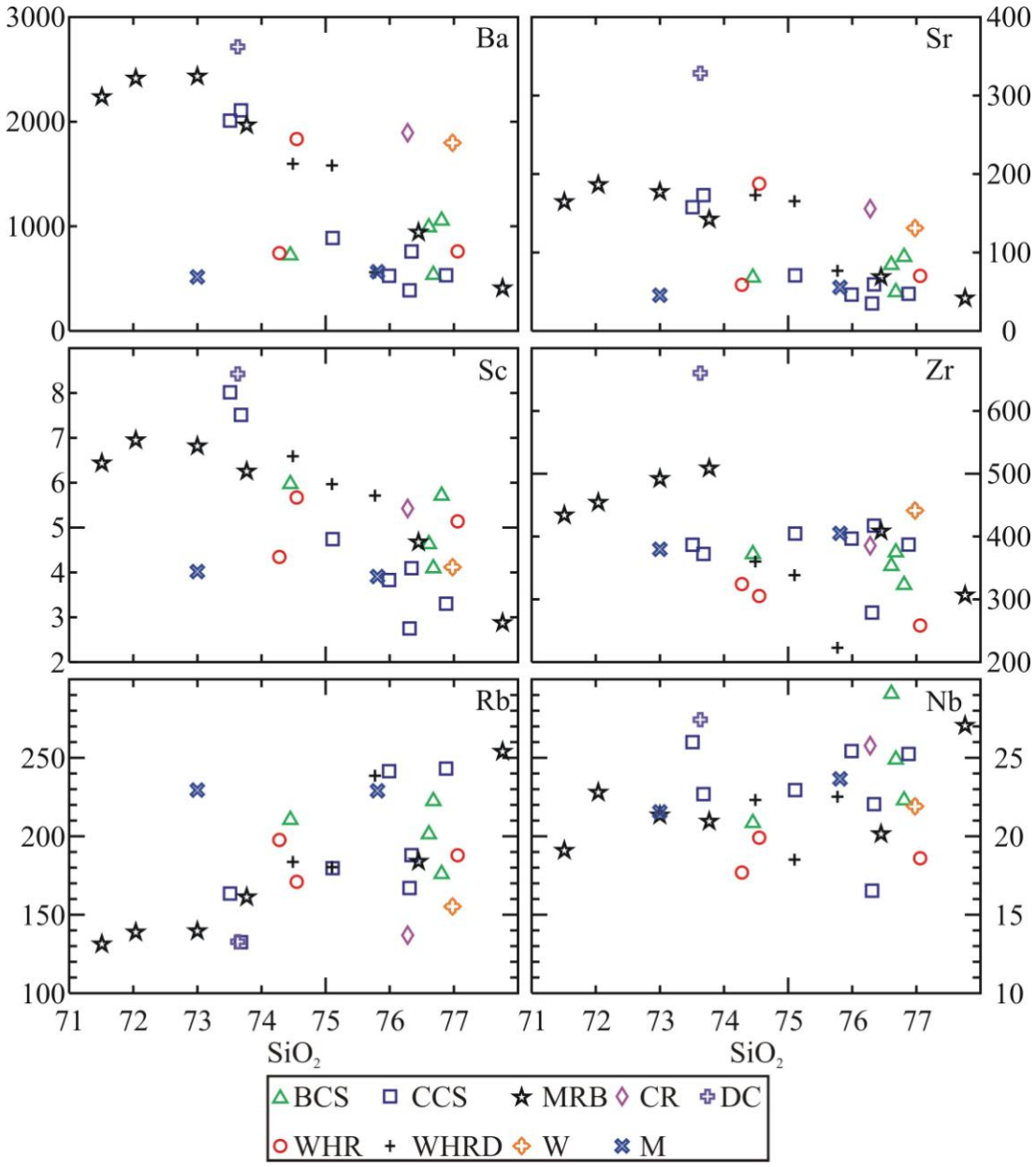

Figure 29: Harker diagrams of selected trace elements. Ba, Sr, Zr, and Sc are behaving compatibly, Rb is behaving incompatibly and Nb is invariant. Abbreviations are consistent with geographic abbreviations in text.

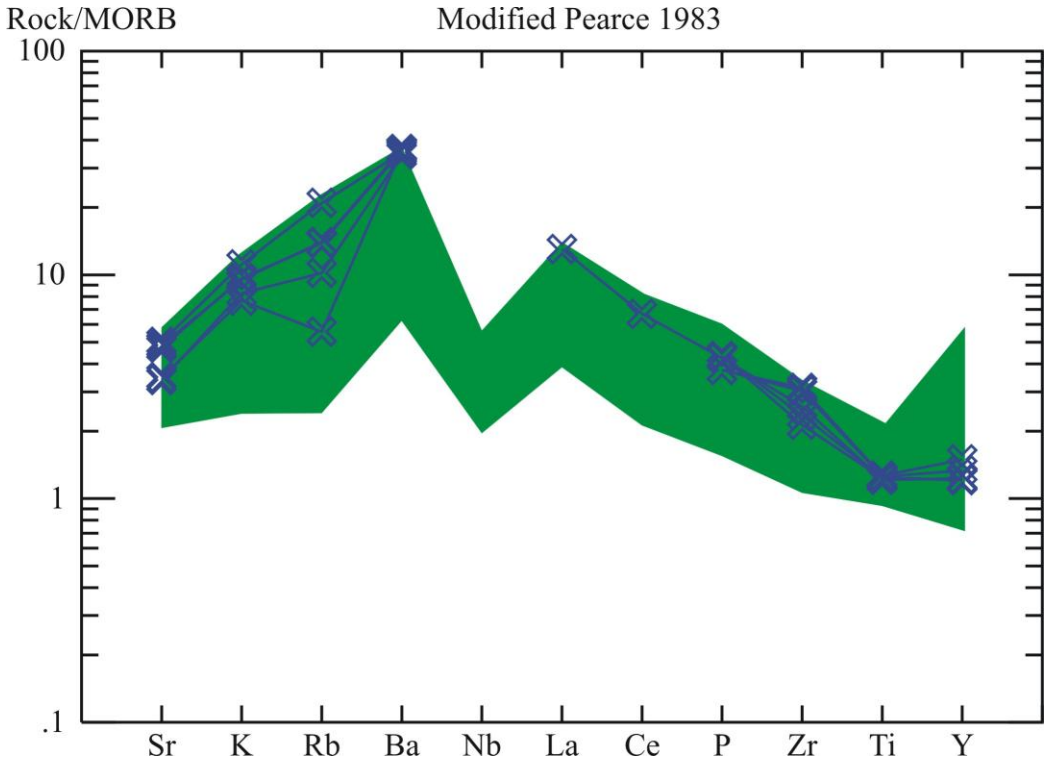

Figure 30: Multi element diagram of MORB normalized Seventy Six basalt, and Steens basalt. The green field encloses compositions of Steens Basalt (Johnson et al., 1998) and the Seventy Six basalt is represented by the hollow X symbols.

Rare Earth Element Geochemistry

Plots of Ba vs. Eu, Sr, and CaO display a positive linear relationship; where as a plot of Ba vs. K_2O displays a negative correlation (Fig. 31). JR samples are enriched in light REEs (LREEs) and to a lesser extent heavy REEs (HREEs), when normalized to chondrite (Sun and McDonough, 1989; Fig. 32). The LREE/HREE ratios normalized to chondrite (Sun and McDonough, 1980) yield La/Lu_N (subscript N indicates the samples are normalized to chondrite composition) of 6.63 and 6.68 for the Seventy Six basalt CB and SR respectively, 10.45 for the Seventy Six enclave, and a range of 12.81-19.61 for Jarbidge Rhyolite, demonstrating increasing fractionation with increasing wt. % SiO_2. Grouping samples into two groups, those from the MB outcrop and those near WHR, La/Lu_N increases with increasing SiO_2 for samples from

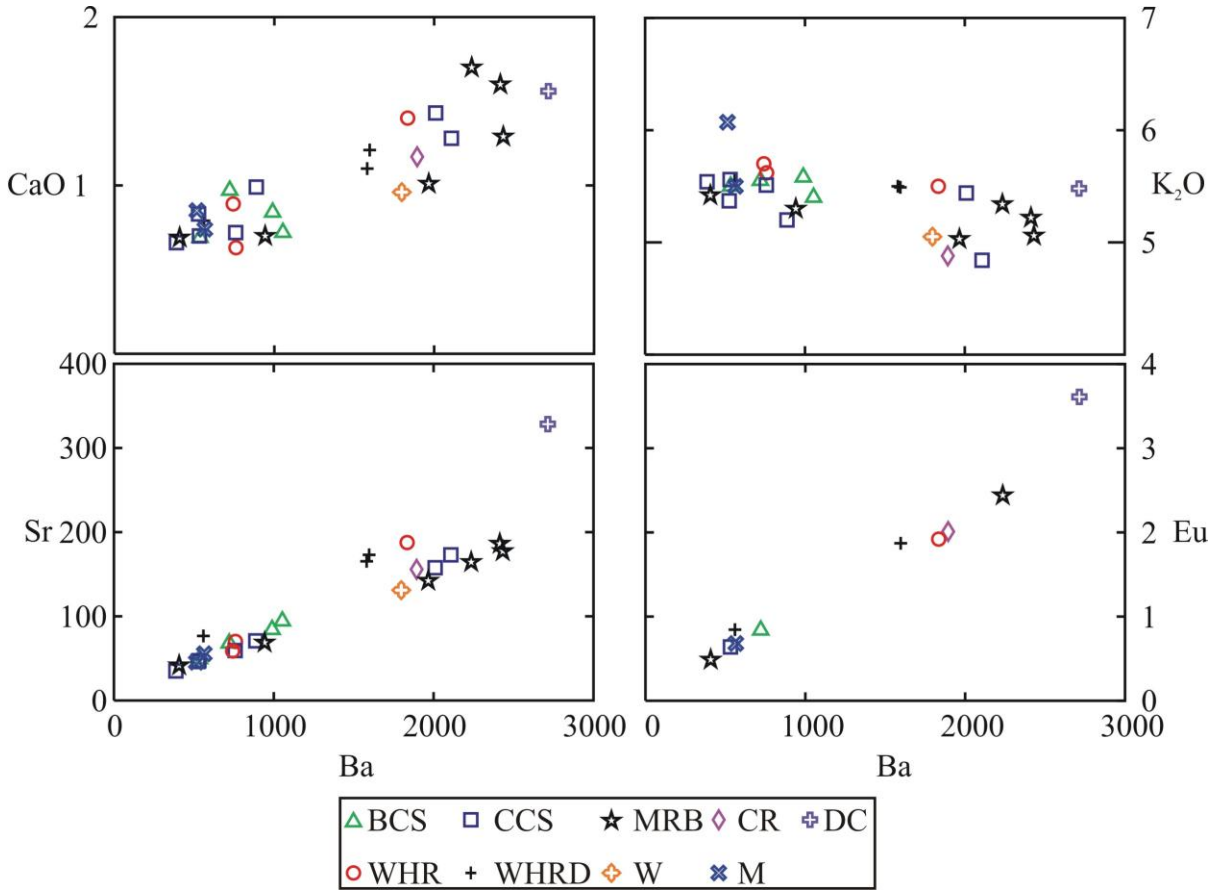

Figure 31: Plots of Ba vs. CaO, K_2O, Sr, and Eu. Correlation of Ba with CaO, Sr, Eu, and K_2O is graphically displayed. Ba, Sr, and Eu reported as ppm and CaO and K_2O reported as wt. %. The high Ba and Sr and low Ba and Sr groups are illustrated on the Ba vs. Sr plot.

the MB (Fig. 33). Eu/Eu* ratios are 36.82 and 40.86 for the Seventy Six basalt, 34.31 for the andesite xenolith, and 11-62.24 for the JR when normalized to chondrite (Sun and McDonough, 1989). The negative Eu anomaly increases with increasing wt. % SiO_2. The chondrite normalized pattern is similar to Bachman and Bergantz's (2009) hot, dry, and reduced REE pattern. With the exception of europium, all samples' REEs are enriched compared to upper continental crust (Taylor and McLennan, 1985). On the tectonic discrimination diagram of Whalen et al. (1984), the Jarbidge Rhyolite plots in the anorogenic (A-type) field.

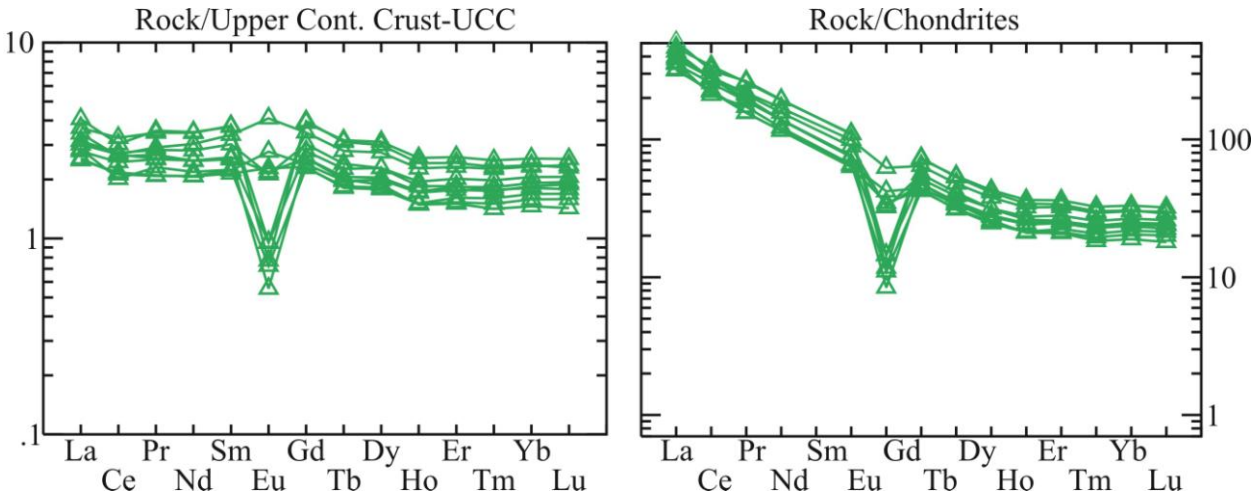

Figure 32: Rare earth element multi-element diagrams of Jarbidge Rhyolite normalized to upper continental crust (Taylor and McLennan, 1985) and chondrite (Sun & McDonough, 1989) compositions. The overall patterns are similar and the Eu differences can be explained by plagioclase fractionation.

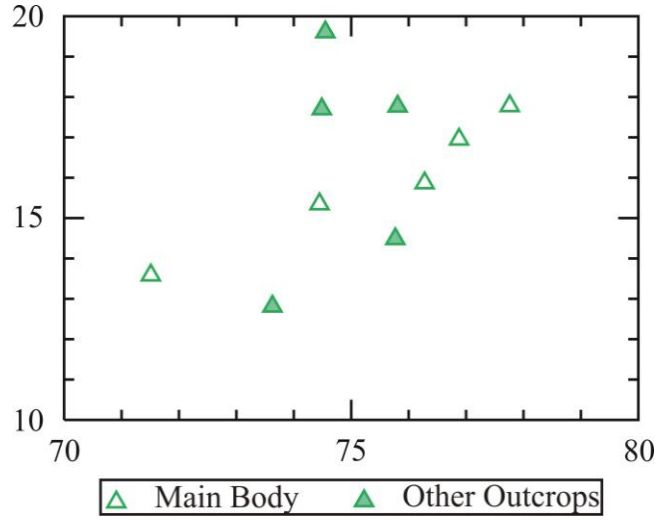

Figure 33: La/Lu_N vs. wt. % SiO_2 differences graphically displayed. Samples collected around Wild Horse Reservoir are abbreviated WHR JR and samples collected within the main body of Jarbidge Rhyolite are abbreviated MB JR.

CHAPTER 6 - **OXYGEN ISOTOPES**

Feldspar and quartz separates were handpicked from the same crushed sample prepared for geochemistry. Crystals selected for analysis are free of inclusions and apparent alteration. Values are reported as ‰ $\delta^{18}O_{VSMOW}$ (Vienna standard mean ocean water). Oxygen isotope data of quartz and feldspar separates were obtained for BCS, CCS, MRB, DC, and WHRD and only feldspar values were obtained for WHR and M (Table 2).

Table 2: Reported values of $\delta^{18}O$, "-" indicates no sample was analyzed.

Location	Sample	Quartz	Feldspar
BCS	JC-08-10	7.45	6.67
CCS	JC-09-4	7.96	6.61
MRB	JC-09-8	8.28	7.34
DC	JC-09-15	8.46	7.74
WHR	JC-08-26	-	7.84
WHRD	JC-08-25	7.72	8.24
M	JC-09-17	-	8.95

Minerals in isotopic equilibrium with the magma and not altered by a post emplacement event have $\delta^{18}O_{feldspar}<\delta^{18}O_{quartz}$ (Taylor, 1968). Such a relation is displayed by all samples except JC-08-25, which displays $\delta^{18}O_{feldspar}>\delta^{18}O_{quartz}$ (Fig. 34). The reversal is evidence of a low temperature hydrothermal event (Taylor, 1968). The $\Delta_{quartz\text{-}feldspar}$ values (which is the difference between, $\delta^{18}O_{quartz}$ and $\delta^{18}O_{feldspar}$) are ≤ 2, with the exception of the WHRD sample, (Fig. 34), indicating they were in isotopic equilibrium with the magma. This permits the $\delta^{18}O_{feldspar}$ value to proxy for the magmatic $\delta^{18}O$ value of a sample (Taylor, 1968; Boroughs et al., 2005). Feldspar values from rhyolitic melts may range 0.2-0.4 lower than the melt value (Taylor, 1968). Unaltered whole igneous rock $\delta^{18}O$ values range from 6-10‰ (Taylor, 1978), and the proxy whole rock values for JR are 6.61-8.95‰.

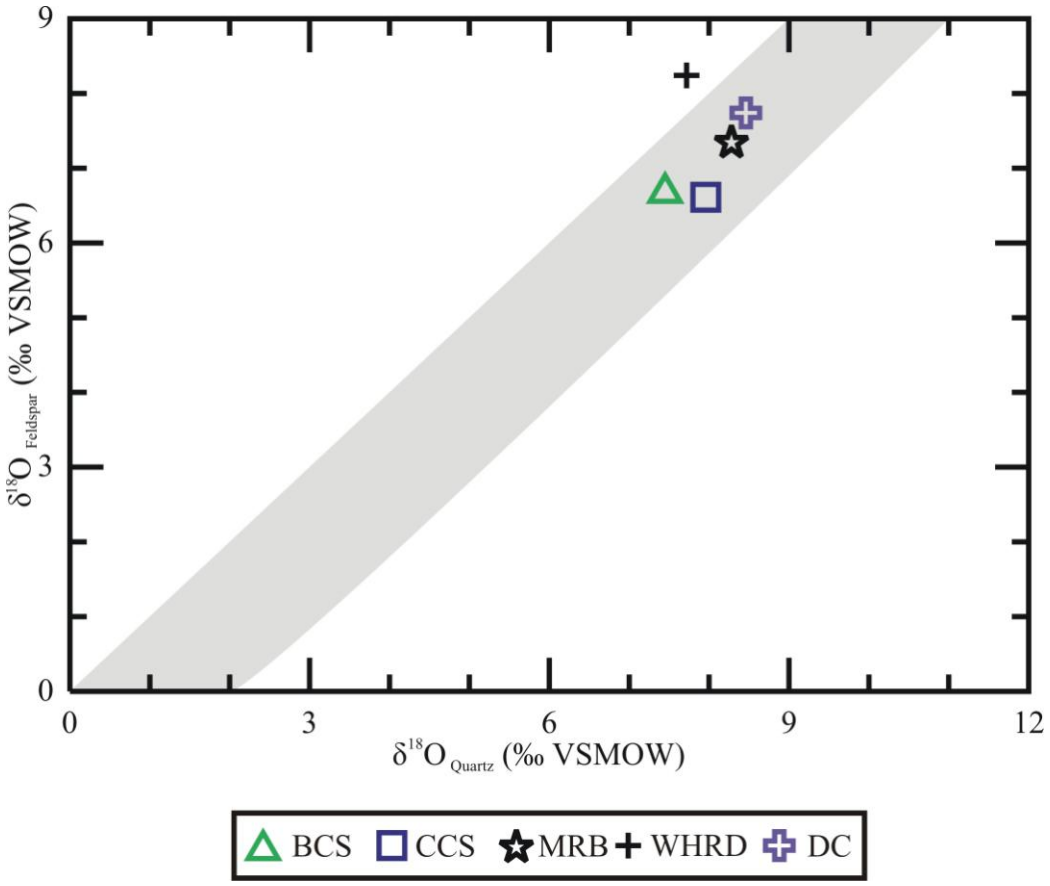

Figure 34: Diagram of $\delta^{18}O_{quartz}$ and $\delta^{18}O_{feldspar}$. Samples which are in isotopic equilibrium fall in the gray field. Legend is the same as chemical legend.

CHAPTER 7 - **GEOCHRONOLOGY**

Three samples were chosen for geochronology, JC-08-10 from BCS, JC-08-24 from WHR, and JC-08-25 from WHRD. Approximate sample locations and respective ages are plotted on a base map (Fig. 35), and exact UTM coordinates can be found in Appendix A. Samples from BCS, JC-08-10, and WHRD, JC-08-25, have reported ages of single crystal analyses (Table 3), and JC-08-24 (Table 4) has age reported from incremental step heating technique. The mean standard weighted deviate (MSWD) from single crystal analyses for sample JC-08-24 was unacceptable. This sample was subsequently analyzed via incremental step heating technique.

Table 3: Table summarizes single crystal analyses. Abbreviations are "MSWD" for mean standard weighted deviate and "n" represents the number of crystals analyzed.

Sample	Location	MSWD	n	Age (Ma)	±1σ
JC-08-10	BCS	0.99	10	15.76	0.06
JC-08-25	WHRD	14	18	16.66	0.05

Table 4: Table summarizes incremental heating technique. "Steps" heading indicates how many heating intervals are involved in the reported age and "% Ar" indicates the total percent of Ar used to calculate the reported age.

Sample	Location	MSWD	Steps	% ^{39}Ar	Age (Ma)	±1σ
JC-08-24	WHR	1.12	10	88	16.30	0.03

Sample JC-08-10 is from BCS and yields an age of 15.78±0.06 Ma. An ideogram displays a broad base and peak (Fig. 36). The age for sample JC-08-24 was produced via step heating, and yields an age of 16.30±0.03 Ma (Fig. 37). The WHRD sample, JC-08-25, has a multi peak ideogram, with a reported age of 16.66±0.05 Ma (Fig. 38). This sample also has a negative $\Delta_{quartz\text{-}feldspar}$ value, an indicator of hydrothermal alteration (Taylor, 1968). The multiple peak ideogram is believed to be the result of the hydrothermal event indicated by oxygen isotopes.

The new ages indicate volcanism initiated 16.66±0.05 Ma at WHRD and was active until at least 15.76 ±0.06 Ma at BCS. The ages reported by this study bracket the ^{40}Ar/^{39}Ar age of 16.2 Ma. for JR volcanism in Bull Run Basin (Henry, 2008). The K/Ar age of 16.8± 0.5 Ma from the Mahoganies overlaps with the new ages (Evernden et al., 1964). The K/Ar ages for samples

near Wild Horse Reservoir (15.4 Ma north of Wild Horse Reservoir [Evernden et al., 1964] and15.4 Ma east of Wild Horse Reservoir [Coats, 1964]), indicate younger ages for JR volcanism in this region. However more $^{40}Ar/^{39}Ar$ geochronology is needed to validate these ages because the K-Ar geochronology yields younger and more imprecise results than the $^{40}Ar/^{39}Ar$ technique. Combined ages from this study and previous studies are used to approximate duration of volcanism at a location. Volcanism around the WHR region may have been active ca. 16.8 -15.4 Ma and MB volcanism may have been active ~15.8 to 14 Ma.

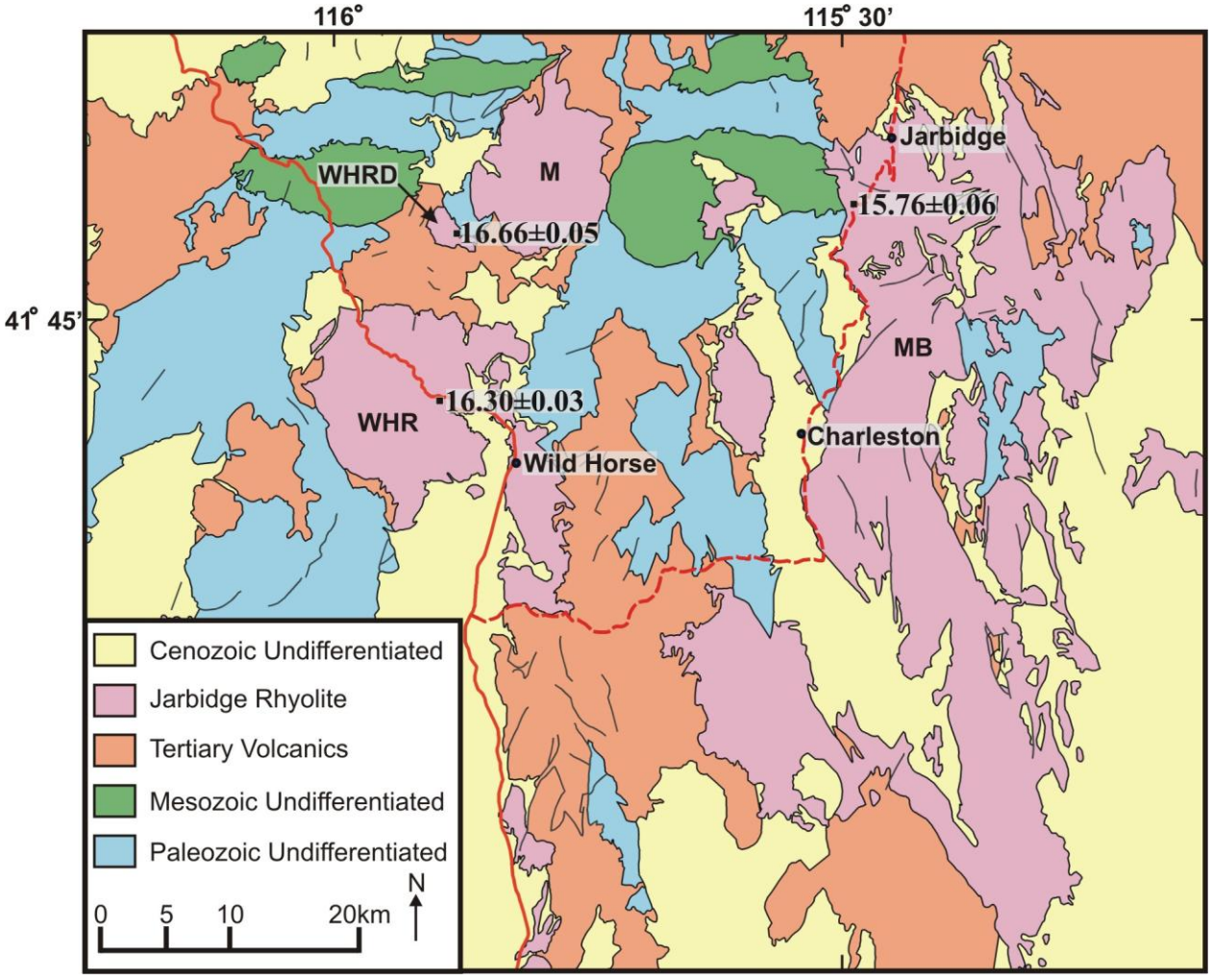

Figure 35: Depiction of approximate location of dated samples, and ages in million years ago. Map is a simplified portion of Coats (1987) geologic map of Elko County, Nevada. Errors are 1 sigma.

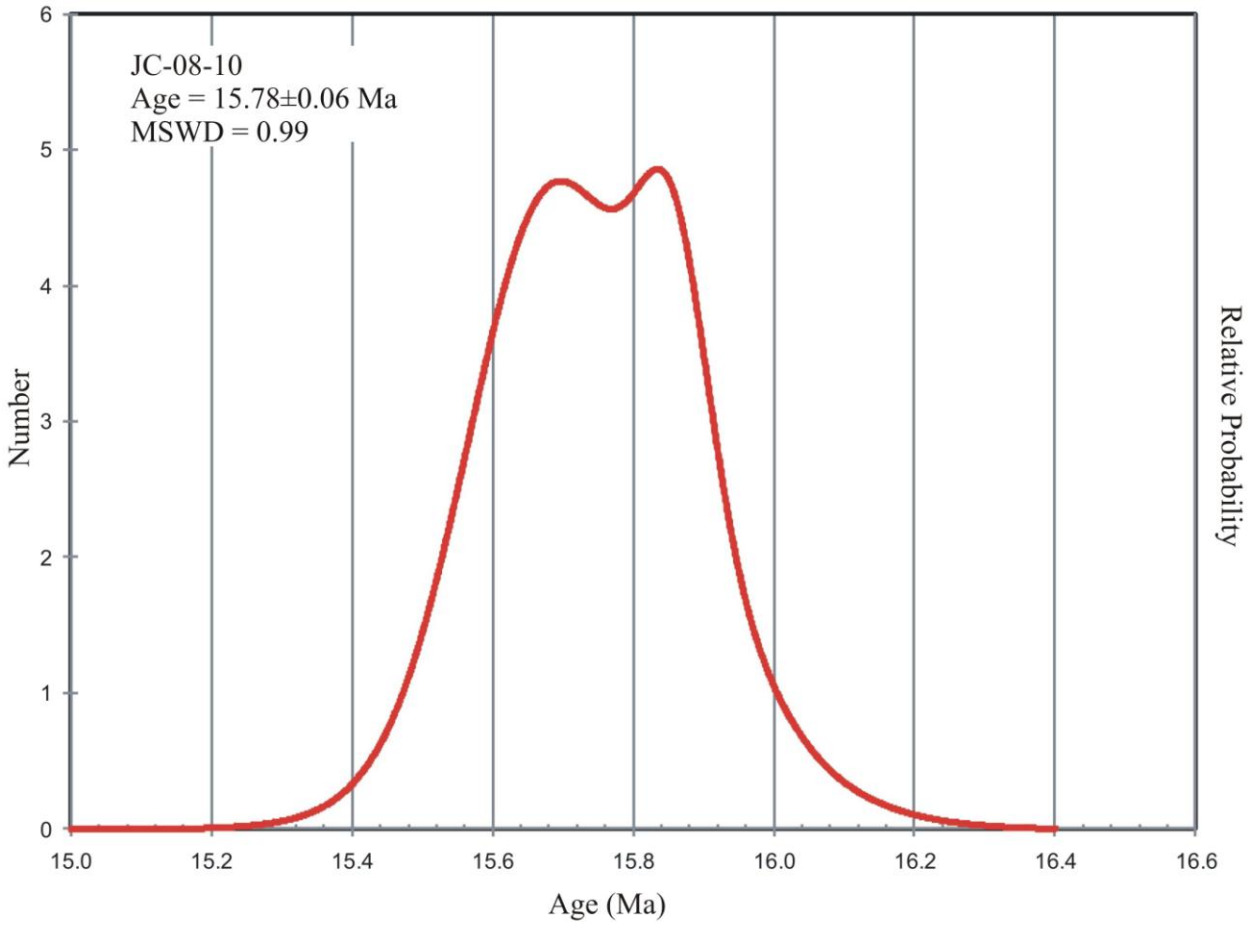

Figure 36: Ideogram of sample JC-08-10. One sigma error.

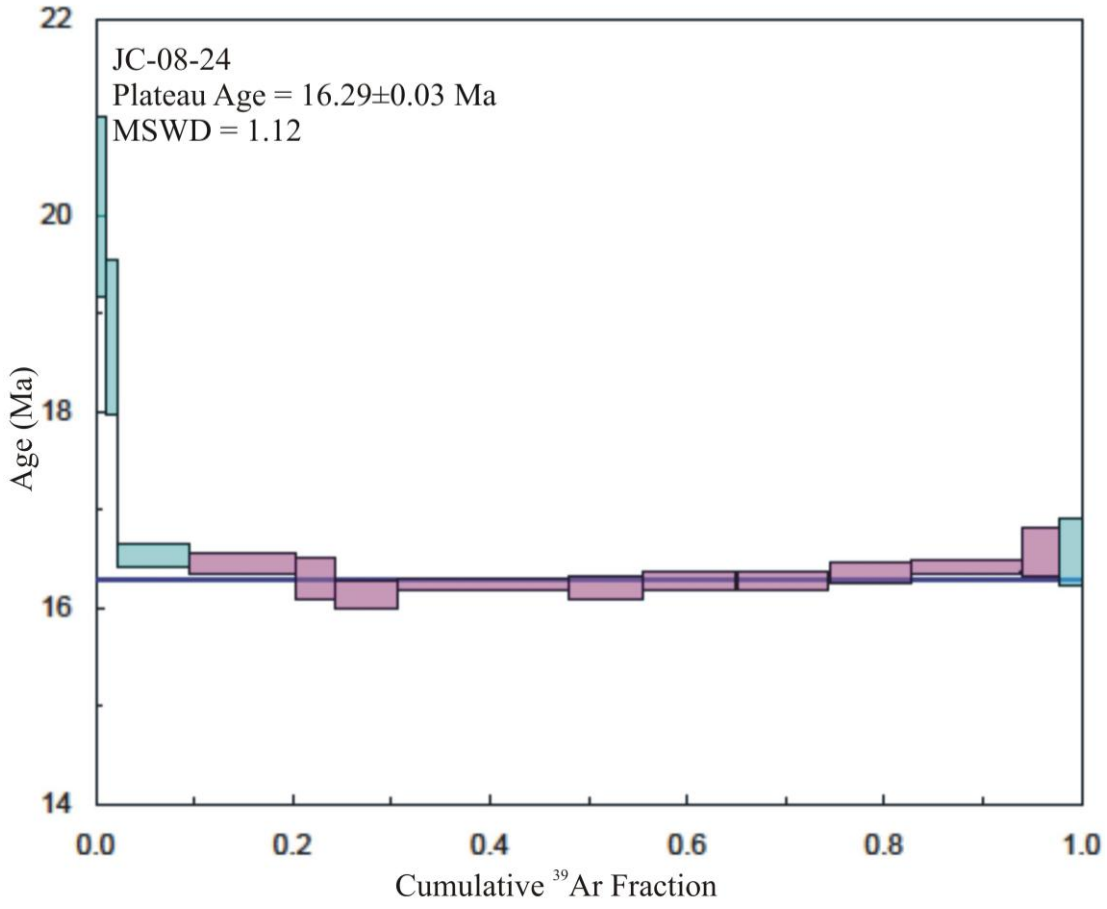

Figure 37: Incremental step heating steps 1-14. Accepted steps are 4-13, in magenta, and rejected steps are 1-3 and 14, in cyan. Box heights represent one sigma error and error for reported age is one sigma.

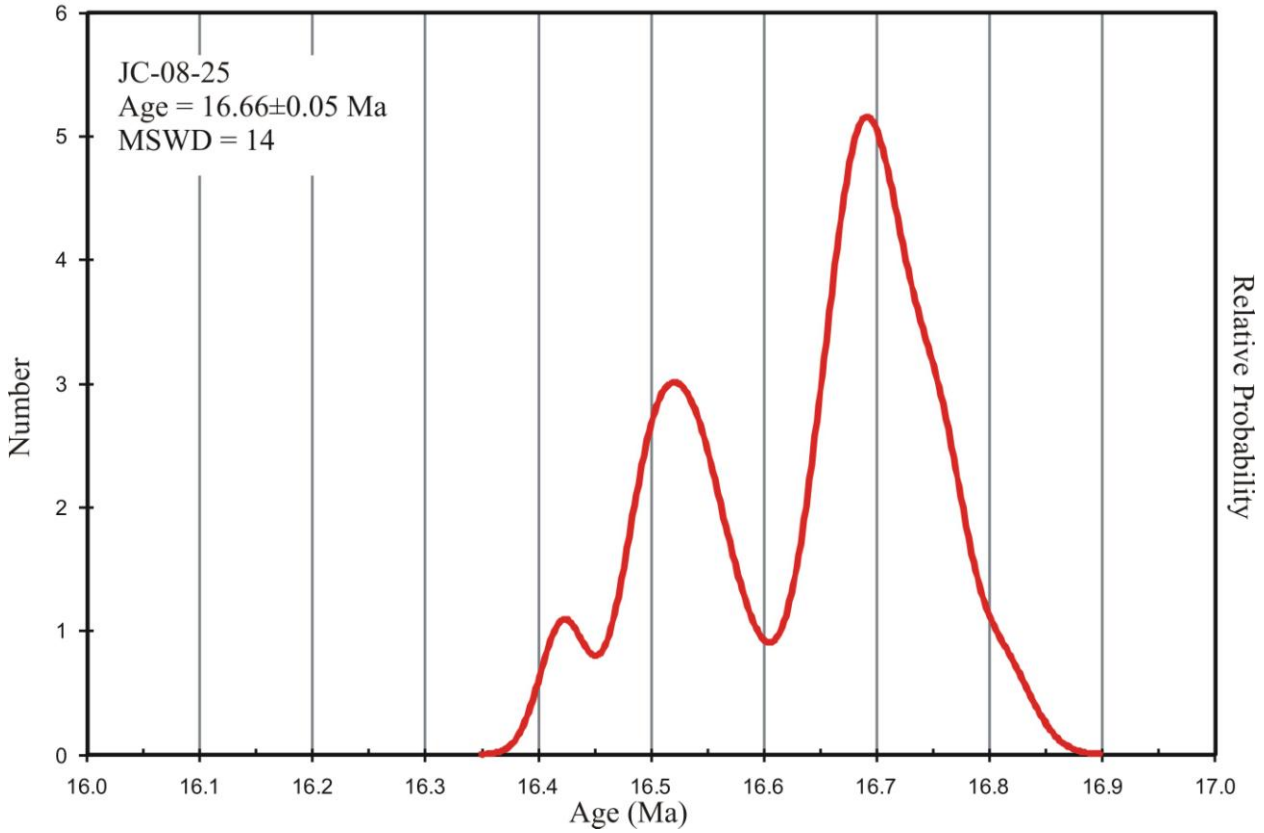

Figure 38: Ideogram of sample JC-08-25. Reported age error is one sigma. The multiple peaks are believed to be the result of the hydrothermal event indicated by oxygen isotopes.

CHAPTER 8 - **DISCUSSION**

Physical Characteristics

Physical volcanology indicates that sampled Jarbidge Rhyolite are lava flows. No pyroclastic textures were found during field or petrographic microscope work. Upper vitrophyric breccias, sheet jointing in stony rhyolite, and carapace and crumble breccia are present in JR lava flows and indicate they are not pyroclastic deposits. What is noted in several basal samples are trachytic and pilotaxitic textures. This type of coherent crystallite defined flow textures in vitrophyre are characteristic of voluminous silicic lava flows (Manley, 1996) and support the macroscopic observations. The contact between basal vitrophyre and interior stony rhyolite could not be clearly seen at all outcrops, but where observed it is irregular. Such basal vitrophyre and stony rhyolite contacts are present in rhyolite lava flows of the Bruneau Jarbidge eruptive center (Bonnichsen and Kaufman, 1987). Generally the JR lava flow interiors are nondescript.

The margins of the flows near Charleston Reservoir are thick and abrupt (Fig. 6) and are characteristic of lava flows (Bonnichsen and Kauffman, 1987; Henry and Wolf, 1992). Given this is a margin, it may be distal from its source. Instead of displaying pyroclastic textures, the margin is encased in carapace breccia, another characteristic of lava flows (Manley, 1996; Manley and McIntosh, 2002).

At the outcrop scale, the identified upper breccia is composed of equant vitrophyric clasts in an ashy matrix, resembling a crumble breccia (Bonnichsen and Kauffman, 1987). In thin section, the sample is characteristic of upper vitrophyric breccias of the Juniper Mountain volcanic center (Manley, 1995 & 1996). Sample JC-09-10A has fractured phenocrysts (Fig. 20C) and debris filling cracks (Fig. 20D). Fracturing appears in-situ since mineral fragments only display minor displacement (Fig. 20C). Manley (1996) states that these fractures form within the flow's carapace and phenocrysts and glass chips are formed via grinding of adjacent fractured faces.

Steep flow margins, carapace breccia, crumble breccia, and crystallite alignment in groundmass supports the conclusion that all sampled JR are lava flows. This does not imply the area is free of pyroclastic deposits. Pyroclastic units at sampled areas may be covered by the

lava flows and Coats (1964 & 1987) and Bernt (1998) report pyroclastic deposits within areas not sampled by this study.

Using conservative extrusive:intrusive ratios of 1:2 (Leeman et al., 2008) and 1:5 (de Silva and Gosnold, 2001), the range of total volume of magma involved in the JR magmatic system is ~1,527-3,054 km^3, with an intrusive component of ~1,018-2,545 km^3. This is a first order calculation that does not take energy and mass balances into account.

The erupted volume qualifies the studied Jarbidge Rhyolite as a large volume rhyolite field (>10 km^3 of erupted material) and such magmatic systems and volcanic provinces can be found in continental margins and rifts, and areas of mantle upwelling (Riley et al., 2001). Examples of large volume effusive silicic volcanism are found in the Bruneau-Jarbidge eruptive center (individual lava flows range 10-200 km^3; Bonnichsen, 1982), the Central Plateau Member rhyolites of the Yellowstone volcanic field (total erupted volume 600-900 km^3; Girard and Stix, 2009), Taylor Creek Rhyolite ($\geq$100 km^3; Duffield and Dalyrmple, 1990), The Badlands lava flow of the Juniper Mountain volcanic center (15 km^3 of erupted material; Manley,1996), and the Chao dacite coulee of the Central Andes ($\geq$26 km^3; de Silva et al., 1994).

Large rhyolite lava flows are insulated by their quenched carapaces. Numerical modeling on a theoretical rhyolite lava flow 150 m thick with sheet geometry and erupting at 950° C indicates the flow could remain mobile for 20 years and may travel 12-60 km (Manley, 1992). This indicates that the flows do not have to be rapidly and effusively emplaced, but could slowly and effusively advance from their eruptive centers.

Petrography

Biotite, in Jarbidge Rhyolite samples, occurs with inclusions of iron oxide, apatite, and zircon, and is an inclusion in plagioclase. These characteristics match the petrographic descriptions of biotite from the nearby Cretaceous Coffee Pot Stock (Seymour, 1980). Xenocrystic microcline is further support for assimilation of granitic rock.

Although garnet is apparent in thin section, it is of xenocrystic origin as evidenced by its anhedral to subhedral form and texture. Plagioclase cored by garnet is found in the CR sample. This type of texture is found in metamorphic rocks (Stowell and Stien, 2005). Also, garnet bearing skarns crop out locally and this may be the source of the xenocrystic garnet.

Other disequilibrium textures in JR include other xenocrysts, xenocrystic clots, ocelli, glass reentrants, rapakivi texture, inclusion rims, crystal corners are rounded and embayed, sieved, boxy, spongy, and skeletal crystals. These textures indicate magma mixing or assimilation and melting of country rock (Stimac, 1992; Seaman, 2000; Hibbard, 1981; Streck, 2008; Bachman et al., 2002). Embayments and ocelli are characteristics of mixing of two distinct magmas (Seaman, 2000). Skeletal plagioclase crystals infilled by sanidine or quartz are the result of magma mixing between a mafic and silicic magma body (Hibbard, 1981). The boxy texture in plagioclase is due to dissolution, given the glass reentrants, and the spongy cellular textures exhibited by some crystals is attributed to pervasive dissolution (Streck, 2008). Spongy plagioclase is attributed to melting (Petcovic and Grunder, 2003; Girard and Stix, 2009). Plagioclase compositions of the basalt and rhyolite also converge at An_{40}.

These petrographic observations imply that assimilation of metamorphic rocks and Cretaceous magnesian (calc-alkaline) granitoid, as well as interaction (e.g. mixing) with mid-Miocene basalt affected the Jarbidge Rhyolite magmatic system. These observations also suggest that a mafic magma body underplated JR magmas at depth.

The combination of field and petrographic evidence suggests effusive eruptions were driven by recharge of basaltic magma into the JR magmatic system. The evidence of magma mixing includes xenocrystic plagioclase and sieved, resorbed, and rounded crystals. Dissolution and resorption of crystals can be caused by the thermal evolution of a magma system due to under platting mafic magmas (Woods and Huppert, 2003). Dissolution and resorption of crystals in a magma system increases volume resulting in over-pressurization of the magma system (Woods and Huppert, 2003). Over-pressurization can be assisted by volatiles from the underplating magma being injected into the overlying silicic system (Woods and Huppert, 2003).

Volcanism within the JR main body was contemporaneous with faulting (Bernt, 1998), and local extensional tectonism was active (Colgan and Henry, 2009). Contemporaneous extensional tectonism and effusive rhyolitic volcanism is also observed in Bearhead Rhyolite in NM, Coso volcanic field in CA, and Taylor Creek rhyolite in NM (Justet and Spell, 2001). These volcanic fields range in area from 150-1,000 km^2 and erupted volumes vary from 1.9 (Coso volcanic field, California; Bacon et al., 1981)- $\geq$100km^3 (Taylor Creek Rhyolite; Duffield and Dalyrmple, 1990).

Geochemistry

Jarbidge Rhyolite lavas are metaluminous-to-slightly peraluminous. Regionally, peralkaline-metaluminous Cenozoic rhyolites are found over the western portion of the Oregon-Idaho-Nevada tristate region, reflecting the accreted underlying lithosphere, whereas silicic volcanism over the Wyoming craton is dominantly peraluminous (Wright et al., 2004; Branney et al., 2008).

The chemical diversity of feldspar-compatible trace elements is highly variable in the sample suite. Europium concentrations normalized to chondrite (Sun and McDonough, 1989) composition illustrate differing degrees of negative Eu anomalies, a trait attributed to plagioclase fractionation. Europium concentrations negatively correlate with SiO_2 and Rb, supporting plagioclase crystal fractionation. The correlation between Ba and Eu, Sr, CaO, and K_2O most likely indicates that Ba is behaving compatibly with plagioclase.

When normalized to chondrite composition (Sun and McDonough, 1989), the LREE enrichment, deep negative Eu anomaly, and relatively flat HREE pattern mimics the REE pattern of hot, dry and reduced magmas of (Bachman and Bergantz, 2009). These magmas are commonly associated with areas of mantle upwelling, continental rifts or hotspots (Bachman and Bergantz, 2009). JR dominantly plots in the "within plate granite field" on a Y+Nb vs. Rb plot (Pearce et al., 1984) and within the A-type granite field (Whalen et al., 1987). The within plate chemical nature of silicic rocks is also established by Nb concentrations >20 ppm, typical of continental rhyolite and oceanic rifts and the JR has average Nb concentration of 22.5± 3.1 ppm (Macdonald et al., 1992; Pankhurst et al., 1998).

The JR has salient characteristics of A-type magmatism with high avg. SiO_2, TiO_2/MgO, and Fe# and the samples plot well within the A-type field of Whalen et al. (1987). Patino Douce (1997) published work supporting evidence that high silica metaluminous A-type magmas could be produced by shallow (<15 km) melting of magnesian granitoid rocks. Additionally, CIPW calculated abundances of quartz, albite, and orthoclase plot on the minima of the pseudo-ternary granite system (Fig. 39) indicating a shallow petrogenesis. Additionally, Turner and Rushmer (2009) published data indicating that FeO and Al_2O_3 concentrations are the product of the lithology being melted. The less evolved JR plots within their tonalite melting field. The published Sr isotope (Christiansen, 1986) and Nd isotope (Nash et al., 2006) work on the JR indicates the involvement of ancient lithosphere in the JR magmatic system. Overall, the data

presented is in agreement with a shallow origin via melting of upper continental crust (magnesian granitoid), rather than lower or middle crust.

The varying degrees of open system textures and similar REE patterns imply similar petrogenetic histories with varying degrees of open-system processes between samples. Varying abundances of xenocrystic phases also support different magma bodies or varying amounts of the same process. Interestingly whole rock trace element ratios largely overlap between sampling locations, and this implies similar petrologic processes occurred between bodies and all JR lavas studied came from the same magma body at depth.

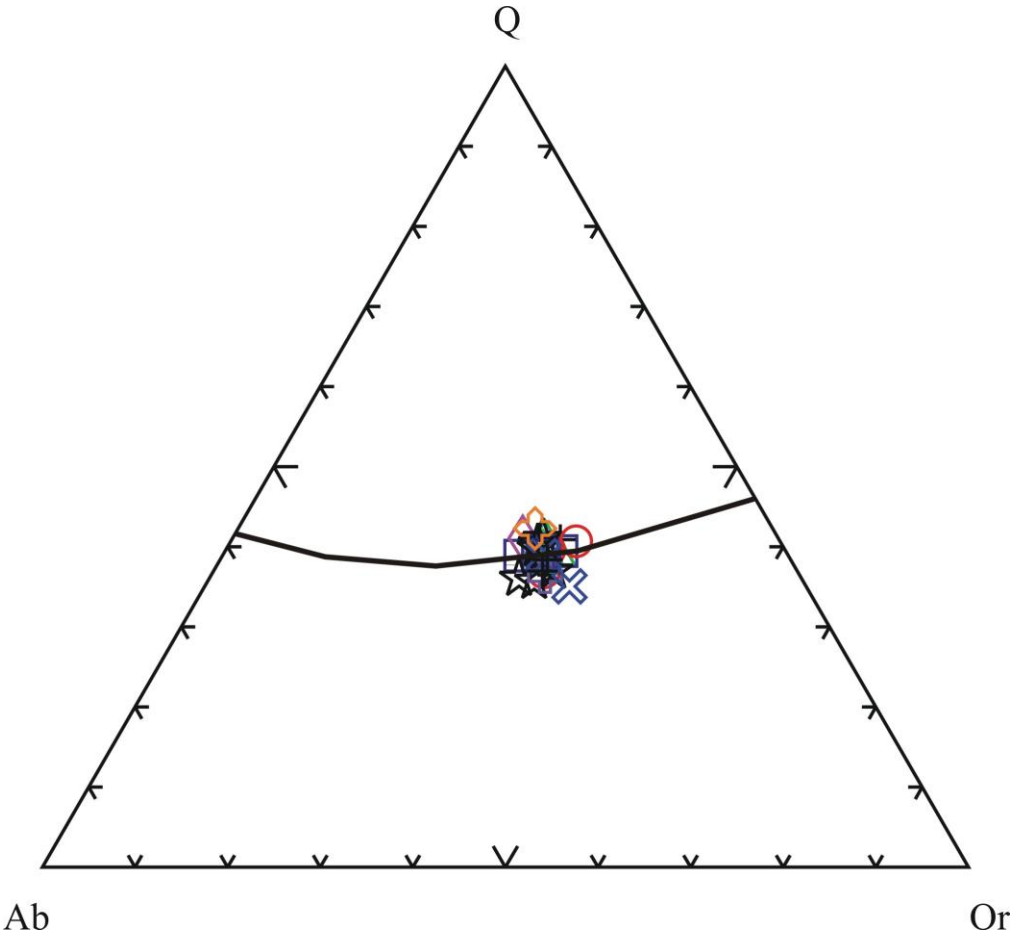

Figure 39: (Q)-Quartz, (Ab)- Albite (Or)-Orthoclase pseudo ternary diagram with JR samples plotting near low pressure high temperature minima. Q, Ab, and Or concentrations are CIPW calculated.

The basalts are not primary as expressed by their low Ni (<36) and Cr (<62) concentrations and elevated (>3.5) K/P ratio of samples (4.7-6.9). The Seventy Six SR basalt has higher SiO_2, MgO, TiO_2, FeO*, Ni, Cr, V, Sc, Zr, Y, and lower K_2O, Al_2O_3, Na2O, and

P_2O_5, Rb, and Sr than the Seventy Six basalt CB. Depletions in FeO*, MgO, Ni, and Cr can be caused by olivine fractionation, FeO*, TiO_2, and V by Fe or Ti oxides, and FeO*, MgO, and Sc depletions can be caused by pyroxene fractionation. A Ba/La ratio of ~18 is indicative of a mantle source enriched in LILE (Weaver, 1991). Such a ratio is achieved by combination of ancient oceanic crust and pelagic sediment (Weaver, 1991). Interestingly, the Seventy Six basalts' Th/La ratios of 0.065 and 0.064 are extremely close to those of MORB (0.067; Weaver, 1991). Given the incompatible nature of each element, crystal fractionation of olivine, pyroxenes and oxide fractionation should not obscure the source's signature. This ratio may increase via assimilation, and said assimilation is indicated by the high K/P ratio.

The significance of these ratios relates to the magma's source (Carlson and Hart, 1988). The overlapping values of Steens and Seventy Six basalt indicate they have the same subduction enriched mantle source. The modified MORB diagram (Fig. 30) illustrates the Seventy Six basalt has element concentrations of LILE, REE, and HFSEs within the concentration ranges of Steens Basalt, indicating the Seventy Six basalt is Steens Basalt.

Oxygen Isotopes

The proxy $\delta^{18}O$ values of the JR are within normal granitic rock range (Taylor, 1979). Normal values indicate the lack of melting and mixing of hydrothermally altered crust, sedimentary or metasedimentary rocks with the Jarbidge Rhyolite magmatic system.

The isotopic disequilibrium observed in the Wild Horse Reservoir Dome sample ($\delta^{18}O_{feldspar}>\delta^{18}O_{quartz}$), indicates that the minerals must have interacted with an isotopically heavier fluid. Taylor (1972) states that a negative $\Delta_{quartz\text{-}feldspar}$ value is "clear cut isotopic evidence of a low temperature hydrothermal event". This sample also has an unusually high K_2O/Na_2O ratio (Fig. 27C). This likely represents a low temperature hydrothermal alteration event.

North of the Jarbidge mining district lies the Bruneau-Jarbidge volcanic center, a unique caldera setting where voluminous, silicic pyroclastic deposits erupted with initially low $\delta^{18}O$ values. This contrasts with the Heise and Yellowstone volcanic fields, which display a temporal pattern of initially normal $\delta^{18}O$ rhyolite volcanism followed by low $\delta^{18}O$ rhyolite volcanism (Watts et al., 2010). Mid-Miocene mineralization is found northwest (Silver City, ID) and immediately south (Jarbidge mining district, NV) of the Bruneau-Jarbidge eruptive center. It is

demonstrated that Au-Ag epithermal deposits in the northern Great Basin are temporally associated with bimodal mid-Miocene volcanism (Wallace, 2003; Saunders et al., 2008). The geothermal systems responsible for mid-Miocene mineralization are believed to be dominantly meteoric water and the ore forming solutions have been shown to be 10 ‰ $\delta^{18}O$ higher than mid-Miocene meteoric water (Saunders et al., 2008). Shifts of this magnitude are reported for waters in equilibrium with secondary minerals and hot springs within Yellowstone (Sturchio et al., 1990); indicating the same $\delta^{18}O$ enrichment in hydrothermal waters can occur at each location. This shift is taken to indicate that the same $\delta^{18}O$ depletion in a rock type could occur to country rock affected by meteoric water dominated ore fluids or intercaldera geothermal fluids. When hydrothermal fluids interact with country rock, the fluid will become enriched in $\delta^{18}O$ and the country rock $\delta^{18}O$ depleted (Taylor, 1978). Whether mid-Miocene mineralization occurred in the location of the Bruneau-Jarbidge volcanic center is unknown, but if it occurred it could result in $\delta^{18}O$ depleted country rock. Additionally, the $\delta^{18}O$ low cycle at BJ may be the result of melting rocks affected by the Jarbidge mineralization event.

Geochronology

The geochronology from this study indicates JR volcanism was active in the region from 16.7-15.8 Ma. The oldest date produced from this study is contemporaneous with the flood basalt volcanism at and around Steens Mountain. Additionally, the $^{40}Ar/^{39}Ar$ age of the Seventy Six basalt, 16.5±0.2 Ma (Rahl et al., 2002), indicates emplacement which is contemporaneous with Steens volcanism. These relationships verify that the JR is an eastward extension of the mid-Miocene ION silicic volcanism associated with the inception of the Yellowstone Hotspot.

Regional Comparison

Several volcanic fields/events have been chosen to compare JR volcanism to, and these include mid-Miocene volcanism of the ION region (e.g. McDermitt caldera complex, Santa Rosa Calico volcanic field, Juniper Mountain volcanic center) and the central Snake River Plain volcanics (e.g. Cougar Point Tuff and central Snake River Plain rhyolite lava flows).

The JR is high silica, meta-to-slightly peraluminous rhyolite with A-type magma characteristics. Of the volcanics being compared CSRP (Cathey and Nash, 2004), and SC and JMVC rhyolites are meta-slightly peraluminous rhyolite with A-type magma characteristics

(high SiO_2, Fe#, and TiO_2/MgO). MD has a TiO_2/MgO ratio <1. A Harker diagram of MgO discriminates the JR and SC rhyolites from the CSRP rhyolites (Fig. 40A). At a given wt. % SiO_2 JR and SC rhyolites have lower wt. % MgO than the CSRP rhyolites. MD and JMVC samples have variable MgO. The difference in wt. % MgO results in higher TiO_2/MgO ratios for JR and SC rhyolites. Also, FeO* is slightly lower in JR and SC at $\leq$74 wt. % SiO_2.

Trace elements further illustrate the similarity between the JR and SC. JR and SC rhyolites have lower Nb (Fig. 40B) and Ta than the CSRP. No Nb data for JMVC or MD is included in the suite, so none is compared. High Nb concentrations in SRP volcanism is attributed to melting of recent basaltic additions to the crust (Christiansen and McCurry, 2008). Additionally, Rb/Nb ratios for JR and SC are higher than those in CSRP at a given wt. % of TiO_2 (Fig. 40C) or SiO_2. The Rb/Nb ratio is higher in crustal rocks and melts derived from them (Pearce et al., 1984; Ayalew and Yirgu, 2003) and not easily changed by partial melting (Christiansen et al., 2007). Such chemical variability may represent mass differences between basaltic and crustal inputs in the SC, JR, and CSRP magmatic systems and implies the petrogenetic processes acting on the JR magmatic system are more similar to those of the SC than CSRP.

A plot of La vs. Lu distinguishes the volcanic fields from one another (Fig. 40D) indicating they are in fact different volcanic fields. A REE pattern of JR normalized to chondrite (Sun and McDonough, 1989) most closely mimics that of the SC (Fig. 41). The MD volcanism has a higher concentration of MREE than does the JR (Fig. 41). Although JR patterns are similar to CSRP volcanics' Cougar Point Tuff (CPT), and CSRP lava flows (CSRPLV), the Eu anomaly is more pronounced in several JR samples and the HREE concentrations are lower in all JR samples (Fig. 41). When normalized to continental crust (Taylor and McLennan, 1995) the JR's pattern once again is closest to SC and generally resembles that of CSRPLF (Fig. 41). LREE, LILE, and HREE concentrations of JR differ from those of MD and CPT.

Oxygen isotope comparison is limited to JR and CSRP, but highlights a very significant difference between the two volcanic systems. The CSRP $\delta^{18}O_{feldspar}$ values range from 1.35-3.76‰ $\delta^{18}O_{quartz}$ range from 2.6-4.7‰ (Boroughs et al., 2005), and magmatic $\delta^{18}O$ values are low ranging 0-3.8‰ (Watts et al., 2010), whereas JR has normal igneous rock $\delta^{18}O$ values. The different $\delta^{18}O$ values indicate the importance of hydrothermally altered crust in the CSRP volcanics' petrogenesis and lack of hydrothermally altered crust in the JR's petrogenesis.

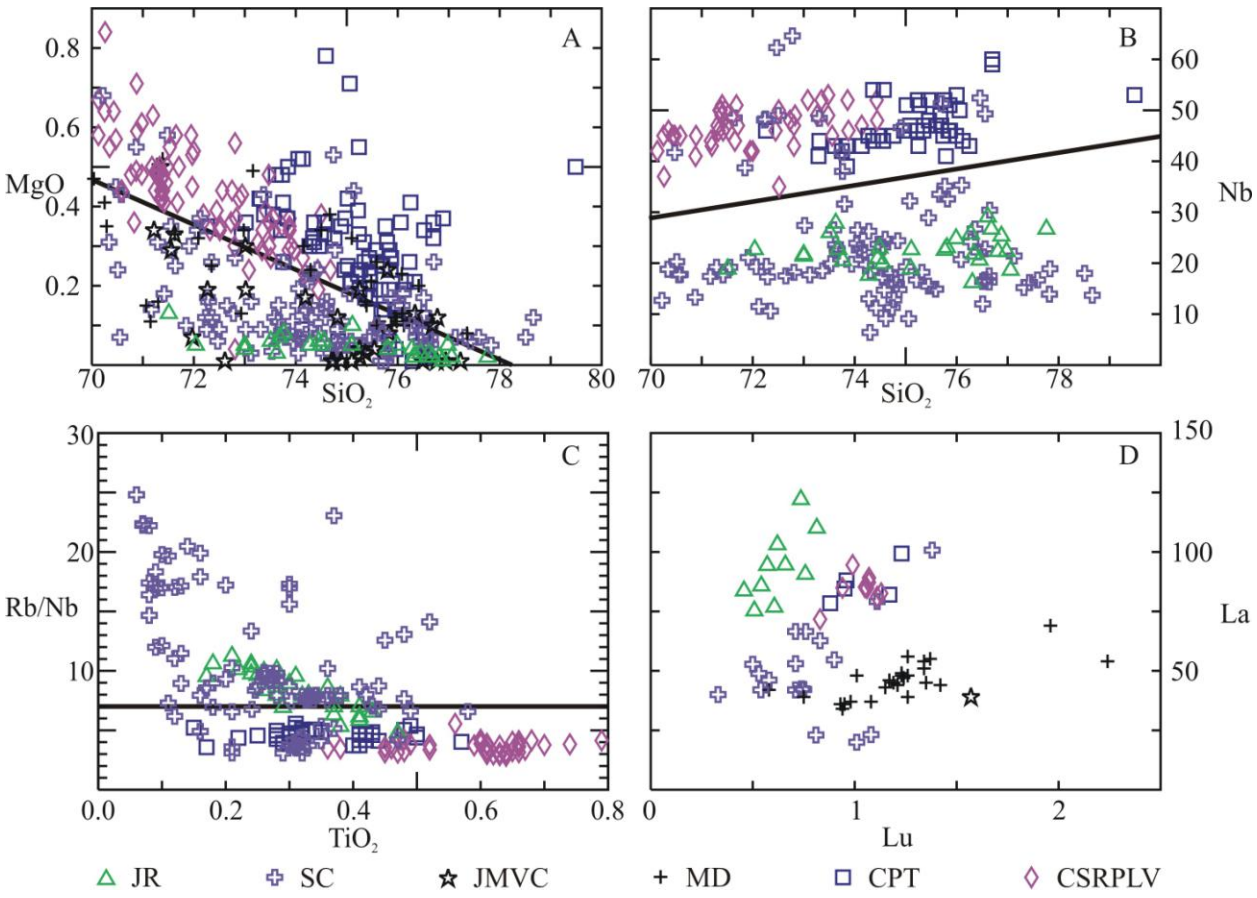

Figure 40: A) Harker of MgO vs. TiO_2. Black line is visually drawn and meant to emphasize the distinction of JR and SC from CSRPL and CPT. JMVC and MC are considered to mainly plot below the line, with JR and SC. B) Harker diagram of Nb. JMVC or MD are not plotted due to lack of data. Black line is visually drawn in to emphasize the difference between JR and SC and CSRPLF and CPT. C) Plot of Rb/Nb vs. TiO_2. Black line is the upper continental crust Rb/Nb ratio (Rudnik and Gao, 2003). D) La vs. Lu plot which distinguishes each volcanic field.

Overall, the JR is temporally and chemically most similar to SC. Further similarities between SC and JR are the eruptive styles of rhyolitic volcanism. The fields display effusive eruptions with fissural sources and domes or coulees (Coats, 1964; Brueseke et al., 2008). Eruptions were stimulated by local upwelling of Steens Basalt and syn-magmatic extension. The fields display the characteristics of mid-Miocene volcanism, silicic and flood basalt volcanism, epithermal Au-Ag mineralization, and similar extensional tectonism.

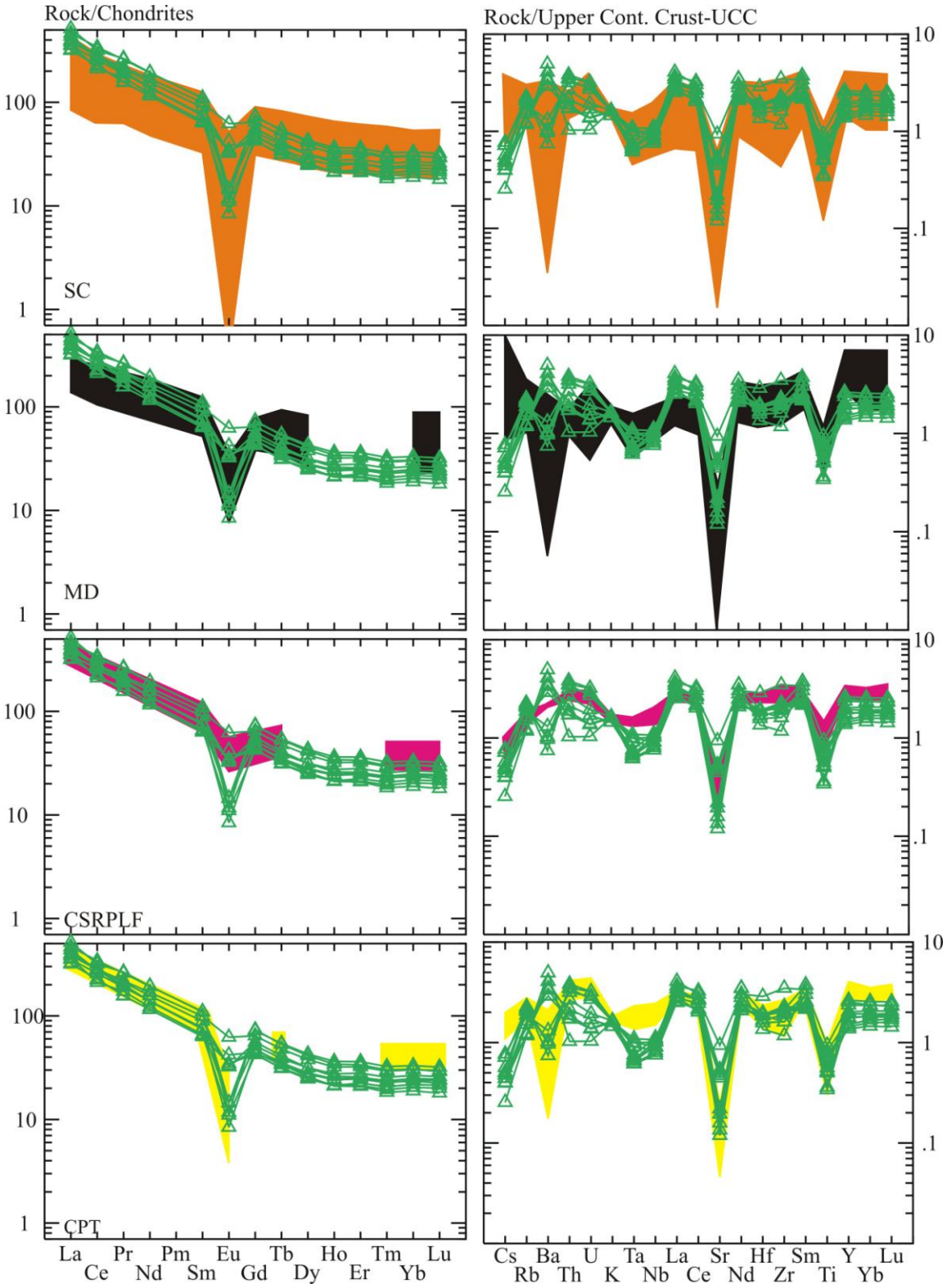

Figure 41: Chondrite and upper continental crust normalized compositions for Santa Rosa volcanic field (SC), McDermitt caldera complex (MD), Central Snake River Plain rhyolite lava flows (CSRPLF), and Cougar Point Tuff (CPT) with JR pattern superimposed on top.

CHAPTER 9 - **SUMMARY**

The presence of thick abrupt flow margins, sheet jointing, carapace and crumble breccia, and crystallite flow orientated basal vitrophyre supports the interpretation that studied JR are lava flows. Pyroclastic deposits at the sampled areas may not have been observed because the lava flows may have over ridden them and buried them beneath the flows. Pyroclastic deposits are reported for areas not sampled by this study (Coats 1964, 1984; Bernt, 1998). Overall, the Jarbidge Rhyolite bodies are coalesced lava domes and flows and pyroclastics.

Xenocrysts indicate the assimilation of magnesian granitoid and possible assimilation of metamorphic rock. Open-system textures and the large feldspar xenocryst imply basalt played a magma mixing role in JR petrogenesis and provided the thermal input for melting local crust. Coupled basaltic input and faulting played a role in the JR eruptions.

The Jarbidge Rhyolite consists of meta-to-slightly peraluminous, normal $\delta^{18}O$ rhyolites with A-type magma characteristics. Parallel REE chondrite and upper continental crust normalized patterns and similar $\delta^{18}O$ values of JR samples suggest a similar petrogenesis between sample locations. A shallow petrogenesis is likely given the samples' position on the Q-Ab-An pseudo ternary diagram. Similar geochemical characteristics produced by shallow melting of calc-alakine granitoid have been reported (Patino Douce, 1997; Petcovic and Grunder, 2003; Turner and Simon, 2009). Oxygen isotope, $^{87}Sr_i/^{86}Sr_i$, and Nd isotope data also support the melting of upper crustal lithologies (Cretaceous granitoid) to produce the Jarbidge Rhyolite.

Jarbidge Rhyolite began erupting in the study area at16.7 Ma with activity lasting until 14 Ma (Bernt, 1998). The temporal nature, local Au-Ag epithermal mineralization, extensional tectonic regime, and local Steens Basalt volcanism suggest this area is an eastern extension of ION Mid-Miocene volcanism.

CHAPTER 10 - **SUGGESTED FUTURE WORK**

Mapping of individual flows is required to fully define the magnitude of Jarbidge Rhyolite volcanism. This can also provide aspect ratio data, a criterion that may be used to distinguish between lava and ash flows. Detailed field mapping can unequivocally prove that these features are domes, and elucidate the extent of individual flows.

A set of analyses and field work to determine viscosity could provide estimates of duration of volcanism and extent of flow migration during and post eruption. Preliminary work could illustrate aspect ratios, which can be a semi-quantitative inference of emplacement and viscosity. Detailed microprobe work for temperature and volatile content could follow. The temperature of the flow could be assessed via: i) Ti in quartz, ii) oxide thermometry iii) and if oxides are used, obtaining oxygen isotopes for the samples which have oxygen isotope data could yield as a check for thermometry.

Comparative chemical and isotopic mineral analyses between the Jarbidge Rhyolite, Coffee Pot Stock, and Seventy Six basalt may confirm the petrogenetic connection between the igneous bodies. Comparing chemical analyses of biotite crystals from the Jarbidge Rhyolite and Coffee Pot Stock may indicate that the JR magma system did assimilate local Cretaceous granitoid. Strontium isotope analysis of plagioclase from the Seventy Six basalt and the xenocrystic plagioclase crystal found in JR can unequivocally indicate a link between the two sources. Whole rock Sr isotope work could provide evidence of magma mixing between the Seventy Six basalt and Cretaceous granitoid or reveal proportions of basalt and granitoid in the JR.

References

Armstrong, R.L., Leeman, W.P., and Malde, N.E., 1975, K-Ar dating, Quaternary and Neogene rocks of the Snake River Plain, Idaho: American Journal of Science, 275, 225-251.

Ayalew, D. & Yirgu, G., 2003, Crustal contribution to the genesis of Ethiopian plateau rhyolitic ignimbrites: basalt and rhyolite geochemical provinciality, Journal of the Geological Society, London, v. 160, p. 47-56.

Bachman, O. and Bergantz, G.W., 2009, Rhyolites and their source mushes across tectonic settings, Journal of Petrology, v. 00, p. 1-9.

Bachman, O., Dungan, M.A., & Lipman, P.W., 2002, The Fish Canyon magma body, San Juan Volcanic Field, Colorado: Rejuvination and eruption of an upper-crustal batholiths. Journal of Petrology, v. 43, p. 1469-1503.

Bacon, C.R., Macdonald, R., Smith, R.L. & Baedecker, P.A., 1981, Pleistocene high-silica rhyolites of the Coso volcanic field, Inyo County, California, Journal of Geophysical Research, v. 86, No. B11, p. 10223-10241.

Basaltic Volcanism Study Project, Basaltic volcanism on the terrestrial planets. 1286 pp., Pergamon, New York, 1981.

Bernt, J.D., 1998, Volcanism, tectonic evolution and gold-silver vein formation in the Jarbidge Mountains, Elko County, Nevada. Geological Society of Nevada Meeting.

Bonnichsen, B., 1982, Rhyolite lava flows in the Bruneau-Jarbidge eruptive center, Southwestern Idaho. Idaho Bureau of Mines and Geology Bulletin v. 26, p. 283-320.

Bonnichsen, B. and Kaufman, D.F., 1987, Physical features of rhyolite lava flows in the Snake River Plain volcanic province, Southwestern Idaho. In: J.H. Fink (Editor), The emplacement of silicic domes and lava flows. Geological Society of America Special paper 212, Pgs. 119-145.

Bonnichsen, B., Leeman, W.P., Honjo, N., McIntosh, W.C. & Godchaux, M.M., 2008, Miocene silicic volcanism in southwestern Idaho: geochronology, geochemistry, and evolution of the central Snake River Plain, Bulletin of Volcanology, V. 70, p. 315-342.

Boroughs, S., Wolff, J., Bonnichsen, B., Godchaux, M., & Larson, P, 2005, Large-volume, low-$\delta^{18}O$ rhyolites of the Central Snake River Plain, Idaho, USA. Geology, v. 33, p. 821-824.

Branney, M.J., Bonnichsen, B., Andrews G.D.M., Ellis, B., Barry, T.L. & McCurry, M., 2008, 'Snake River (SR)-type' volcanism at the Yellostone hotspot track: distinctive products from unusual, high-temperature silicic super-eruptions. Bulletin of Volcanology v. 70, p. 293-314.

Brueseke, M.B. & Hart, W.K., 2009, Geology and petrology of the mid-Miocene Santa Rosa-Calico volcanic field, Northern Nevada, Nevada Bureau of Mines and Geology, Bulletin 113.

Brueseke, M.B. & Hart, W.K., 2009, Intermediate composition magma production in an intracontinental setting: Unusual andesites and dacites of the mid-Miocene Santa Rosa-Calico volcanic field, Northern Nevada. Journal of Volcanology and Geothermal Research, v. 188, p. 197-213.

Brueseke, M.B., Hart, W.K., & Heizler, M.T., 2008, Diverse mid-Miocene silicic volcanism associated with the Yellowstone-Newberry thermal anomaly. Bulletin of Volcanology, v. 70; p. 334-360.

Brueseke, M.B., Heizler, M.T., Hart, W.K., & Mertzman, S.A., 2007, Distribution and geochronology of Oregon Plateau (U.S.A.) flood basalt volcanism: The Steens basalt revisited. Journal of Volcanology and Geothermal Research v. 161, p. 187-217.

Callicoat, J. & Brueseke, M.E., 2009, Mid-Miocene volcanism in northeast Nevada: Spatial, chemical and chronologic significance of the Jarbidge Rhyolite. Geological Society of America Abstracts, 2009 Annual meeting, Portland.

Camp, V.E. & Hanan, B.B., 2008, A plume-triggered delamination origin for the Columbia River Basalt Group. Geosphere, v. 4, p. 480-495.

Camp, V.E. & Ross, M.E., 2004, Mantle dynamics and genesis of mafic magmatism in the intermontane Pacific Northwest. Journal of Geophysical Research, v. 109. doi: 10.1029/2003JB002838.

Camp, V.E., Ross, M.E. & Hanson, W.E., 2003, Genesis of flood basalts and Basin and Range volcanic rocks from Steens Mountain to the Malheur River Gorge, Oregon. Geolocial Society of America Bulletin, v. 115, p. 105-128.

Carlson, R.W. & Hart, W.K., 1985, Distribution and geochronology of Steens Mountain-type basalts from the northwestern Great Basin. Isochron West, No. 43, p. 5-10.

Carlson, R.W. & Hart, W.K., 1987, Crustal genesis on the Oregon Plateau. Journal of Geophysical Research, v. 92, n. B7, p. 6191-6206.

Carlson, R.W., and Hart, W.K., 1988, Flood basalt volcanism in the Pacific northwestern United States, in Macdougall, J.D., ed., Continental flood basalts: Dordrecht, Netherlands, Kluwer Academic Publishers, p. 35-62.

Cathey, H.E. & Nash, B.P., 2004, The Cougar Point Tuff: Implications for Thermochemical Zonation and longevity of high-temperature, large volume silicic magmas of the Miocene Yellowstone Hotspot. Journal of Petrology, v. 45, p. 27-58.

Christiansen, R.L., Fougler, G.R., & Evans, J.R., 2002, Upper-mantle origin of the Yellowstone hotpot. Geological Society Upper-mantle origin of the Yellowstone hotpot. Geological Society of America Bulletin, v. 114, p. 1245-1256.

Christiansen, E.H., Haapala, I. & Hart, G.L., 2007, Are Cenozoic topaz rhyolite the erupted equivalents of Proterozoic rapakivi granites? Examples from the western United States Finland, Lithos, p. 219-246.

Christiansen, E.H. & McCurry, M., 2008, Contrasting origins of Cenozoic silicic volcanic rocks from the western Cordillera of the United States. Bulletin of Volcanology, v. 70, p. 251-267.

Christansen, E.H., Sheridan, M.F., & Burt, D.M., 1986, The geology and geochemistry of cenozoic topaz rhyolites from the Western United States. Geological Society of America Special Paper 205.

Coats, R.R., 1964, Geology of the Jarbidge Quadrangle, Nevada-Idaho: Contributions to General Geology. Geological Survey Bulletin 1141-M.

Coats, R.R., 1987, Geology of Elko County, Nevada. Nevada Bureau of Mines and Geology Bulletin 101.

Cummings, M.L., Evans, J.G., Ferns, M.L. & Less K.R., 2000, Stratigraphic and structural evolution of the middle Miocene synvolcanic Oregon-Idaho graben, v. 112, No. 5, p. 668-682.

Colgan, J.P. & Henry, C.D., 2009, Rapid middle Miocene collapse of the Mesozoic orogenic plateau in north-central Nevada, International Geology Review. v. 51, No. 9-11, p. 920-961.

Delvigne, J.E., 1998, Atlas of micromorphology of mineral alteration and weathering. Mineralogical Association of Canada. Ottawa, Ontario, Canada.

De Silva, S.L. & Gosnold, W.D., 2001, Episodic construction of batholiths: Insights from the spatiotemporal development of an ignimbrite flare-up. Journal of Volcanology and Geothermal Research, v. 167, p. 320-335.

De Silva, S.L., Self, S., Francis, P.W., Drake, R.E. & Carlos, R.R..,1994, Effusive silicic volcanism in the Central Andes: The Chao dacite and other young lavas of the Altiplano-Puna Volcanic Complex. Journal of Geophysical Research, Vol. 99, No. B9, p. 17,805-17,825.

Duffield, W.A. & Dalrymple, G.V., 1990, The Taylor Creek Rhyolite of New Mexico: a rapidly emplaced field of lava domes and flows, Bulletin of Volcanology, v. 52, p. 474-487.

Evernden, J.F., Savage, D.E., Curtix, G.H. and James, G.T. (1964), Potassium-Argon dates and the Cenozoic mammalian chronology of North America. American Journal of Science, v. 262, p. 145-198.

Frost, R.B., Barnes, C.G., Collings, W.J., Arculus, R.J., Ellis, D.J. & Frost, C.D., 2001, A geochemical classification for granitic rocks. Journal of Petrology, v. 42, No. 11, p. 2033-2048.

Girard, G. & Stix, J., 2009, Magma recharge and crystal mush rejuvenation associated with early post-collapse Upper Basin Member Rhyolites, Yellowstone Caldera, Wyoming, Journal of Petrology, v. 50, p. 2095-2125.

Hart, W.K. & Carlson R.W., 1985, Distribution and geochronology of Steen Mountain-type basalts from the northwestern Great Basin. Isochron West, no. 43 p. 5-10.

Henry, C.D., 2008, Ash-flow tuffs and paleovalleys in northeastern Nevada: Implications for Eocene paleogeography and extension in Sevier hinterland, northern Great Basin. Geosphere, v. 4, no. 1, p. 1-35.

Henry, C. & Wolff, J., 1992, Distinguishing strongly rheomorphic tuffs from extensive silicic lavas. Bulletin of Volcanology, v. 54, p. 171-186.

Hibbard, M.J., 1981, The magma mixing origin of mantled feldspars. Contributions to Mineral Petrology, v. 76, p. 158-170.

Hooper, P.R., Binger, G.B. & Lees, K.R. ,2002, Ages of the Steens and Columbia River flood basalts and their relationship to extension-related calc-alkalic volcanism in eastern Oregon. Geological Society of America Bulletin, v. 114, p. 43-50.

John, D., 2001, Miocene and early Pliocene epithermal gold-silver deposits in the northern Great Basin, Western United States; characteristics, distribution, and relationship to magmatism. Economic geology and the bulletin of the Society of Economic Geologist, v. 96, p. 1827-1853.

Johnson, J.A., Hawkesworth, C.J., Hooper, C.J., Binger, P.R., 1998, Major- and trace-element analyses of Steens Basalt, Southeastern Oregon, U.S. Geol. Surv. Open File Rep., v. 98-482, p. 30.

Jordan, B.T., Grunder, A.L., Duncan, R.A. & Deino, A.L., 2004, Geochronology and age progressive volcanism of the Oregon High Lava Plains: Implications for the plume interpretation of Yellowstone. Journal of Geophysical Research, v. 109, p. 10202-10220.

Justet, L & Spell, T.L. ,2001, Effusive eruptions from a large silicic magma chamber: the Bearhead Rhyolite, Jemez volcanic field, NM, Journal of Volcanology and Geothermal Research, v. 107, p. 241-264.

Katoh, S., Danhara, T., Hart, W.K. & Wolde Gabriel, G., 1999, Use of sodium polytungstate solution in the purification of volcanic glass shards for bulk chemical analysis. Nature and Human Activities, v. 4, p. 45-54.

Le Bas, M.J., Le Maitre, R.W., Streckeisen, A. & Zanettin, B., 1986, Chemical classification of volcanic rocks based on total alkali-silica diagram, v. 27, No. 3, p. 745-750.

Leeman, W.P., Annen, C. & Dufek ,2008, Snake River Plain-Yellowstone silicic volcanism: implications for magma genesis and magma fluxes. Geological Society of London, v. 304, p. 235-259.

LeMaitre, R.W., 1976, Some problems of the projection of chemical data into mineralogical classifications, Contributions to mineralogy and Petrology, v. 56, p. 181-189.

Ludwig, K., 2003, User's manual for Isoplot 3.0: A geochronological tool kit for Microsoft excel, Berkley geochronology center, Special Publication No. 4.

Manley, C.R., 1992, Extended cooling and viscous flow of large, hot rhyolite lavas: implications of numerical modeling results, Journal of Volcanology and Geothermal Research, v. 53, p. 27-46.

Manley, C.R.,1995, How voluminous rhyolite lavas mimic rhemorphic ignimbrites: eruptive style emplacement conditions, and formation of tuff-like textures, Geology, v. 23, n. 4, p. 349-352.

Manley, C.R., 1996, In situ formation of welded tuff-like textures in the carapace of a voluminous silicic lava flow, Owyhee County, SW Idaho. Bulletin of Volcanology, v. 57, p. 672-686.

Manley, C.R & McIntosh, W.C., 2002, The Juniper Mountain Volcanic Center, Owyhee County, Southwestern Idaho: Age relations and physical volcanology. In Bill Bonnichsen, C.M. White and Michael McCurry, eds., Tectonic and Magmatic Evolution of the Snake River Plain Volcanic Province. Idaho Geological Survey Bulletin 30, p. 207-227.

Miyarshiro, A., 1974, Volcanic rock series in island arcs and active continental margins, American Journal of Science, v. 274, p. 321-355.

Nash, B.P., Perkins, M.E., Christensen, D.L., & Halliday, A.N., 2006, The Yellowstone hotspot in space and time: Nd and Hf isotopes in silicic magmas. Earth and Planetary Science Letters, v. 247, p. 143-156.

Pankhurst, R.J., Leat, P.T., Sruoga, P., Rapela, C.W., Marquez, M., Storey, B.C. & Riley, T.R., 1998, The Chon Aike province of Patagonia and related rocks in West Antartica: A silicic large igneous province, Journal of Volcanology and Geothermal Research, v. 81, p. 113-136.

Patino Douce, A. E., 1997, Generation of metaluminous A-type granites by shallow melting of calc-alkaline granitioids, Geology, v. 25, no. 8, p. 743-746.

Pearce, J.A., Harris, N.B.W. & Tindle, A.G., 1984, Trace element discrimination diagrams for tectonic interpretation of granitic rocks. Journal of Petrology, v. 25, p. 956-984.

Perkins, M.E. & Nash, B.P., 2002, Explosive silicic volcanism of the Yellowstone hotspot: The ash fall tuff record. Geological Society of America Bulletin, v. 114, p. 367-381.

Petcovic, H.L. & Grunder, A.L., 2003, Textural and thermal history of partial melting in tonalitic wallrock at the margin of a basalt dike, Wallowa Mountains, Oregon, Journal of Petrology, v. 44, No. 12, p. 2287-2312.

Rahl, J.M., McGrew, A.J. & Poland, K.A., 2002, Transition from contraction to extension in the Northeastern Basin and Range: New evidence from the Copper Mountains, Nevada. The Journal of Geology, v. 110, p. 179-194.

Riley, T.R., Leat, P.T., Pankhurst, R.J., & Harris, C., 2001 Origins of large volume rhyolitic volcanism in the Antarctic Peninsula and Patagonia by crustal melting, Journal of Petrology, v. 42, No. 6, p. 1043-1065.

Rudnik, R.L. & Gao, S., 2003, Composition of the continental crust, Treatise of geochemistry, Chapter 3, p. 1-64.

Saunders, J.A., Unger, D.L., Kamenov, G.D., Fayek, M., Hames, W.E., & Utterback, W.C., 2008, Genesis of Middle Miocene Yellowstone hotspot-related bonanza epithermal Au-Ag deposits, Northern Great Basin USA. Miner Deposita,v. 43, p. 715-734.

Schrader, F.C., 1912, Jarbidge, Contact, and Elk Mountain Mining Districts, Elko County Nevada. United States Geological Survey, Bulletin 497, p. 9-134.

Seaman, S.J., 2000, Crystal clusters, feldspar glomerocryst, and magma envelopes in the Atascosa lookout lava flow, Southern Arizona, USA: Recorders of magmatic events, Journal of Petrology, v. 41, No. 5, p. 693-716.

Seymour, R.S., 1980, Petrology and geochemistry of the Coffeepot Stock, Nevada : a record of crystallization history and hydrothermal fluid migrations. A thesis, University of Oregon.

Sharp, Z.D., 1990, A laser-based microanalytical method for the in situ determination of oxygen isotope ratios of silicates and oxides: Geochimica et Cosmochimica Acta: v. 54, p. 1353-1357.

Snoke, A.W., Howard, K.A., McGrew, A.J., Burton, B.R., Barnes, C.G., Peters, M.T. & Wright, J.E., 1997, The grand tour of the Ruby-East Humboldt Metamorphic Core Complex, Northeastern Nevada: Part 1- Introduction and road log, Bingham Young University Geology Studies, v. 42, Part 1.

Starkel, W.A., Wolff, J., Henry, C.D. & Castor, S., 2009, Geologic evolution and initial constraints on the petrogenesis of the McDermitt volcanic center, Northern NV, and Southern OR. GSA Abstract, Annual Meeting, 2009.

Stewart, D.B. (1979) The formation of siliceous potassic glassy rocks, In: Yoder, H.S., Jr (ed.) The evolution of Igneous Rocks. Princeton, NJ: Princeton University Press, p. 339-350.

Streck, M.J., 2008, Mineral textures and zoning as evidence for open system processes. Reviews in Mineralogy and Geochemistry, v. 69, p. 595-622.

Stimac, J. & Pearce, T.H., 1992, Textural evidence of mafic felsic magma interaction in dacite lavas, Clear Lake, California, American Mineralogist, v. 70, p.795-809.

Stowell, H.H. & Stein, E., 2005, The significance of plagioclase-dominant coronas on garnet, Wenatchee Block, northern Cascades, Washington, U.S.A. The Canadian Mineralogist, v. 43, p. 267-385.

Sturchio, N.C., Muehlenbachs, K. & Seitz, M.G., 1986 Element redistribution during hydrothermal alteration of rhyolite in an active geothermal system Yellowstone drill cores Y-7 and Y-8, Geochemica et Cosmochimica Acta, v. 50, p. 1619-1631.

Sun, S. & McDonough, W.F., 1989, Chemical and isotopic systematic of oceanic basalts: implications for mantle composition and processes, Geological Society, London, Special Publications, 1989, v. 42, p. 313-345.

Takeuchi, A. & Larson, P., 2005, Oxygen isotope evidence for the late Cenozoic development of an orographic rain shadow in eastern Washington, USA. Geology, v. 33, no. 4, p. 313-316.

Taylor, H., 1968, The oxygen isotope geochemistry of igneous rocks. Contributions to Mineralogy and Petrololgy, v. 19, p. 1-71.

Taylor, H.P., 1978, Oxygen and hydrogen isotope studies of plutonic granitic rocks. Earth and Planetary Science Letters. v. 38, p. 177-210.

Taylor, S.R. and McLennan, S.M., 1985, The continental crust: Its composition and evolution, Blackwell, Oxford, 312 pp.

Turner, S. & Rushmer, T., 2009, Similarities between mantle-derived A-type granites and voluminous rhyolites in continental flood basalt provinces, Earth and Environmental Science Transactions of the Royal Society of Edinburg, v.100, p.51-60.

Valley, J.W., Kitchen, N., Kohn, M.J., Niendorf, C.R., & Spicuzza, M.J., 1995, UWG-2, a garnet standard for oxygen isotope ratios: Strategies for high precision and accuracy with laser heating. Geochimica et Cosmochimica Acta, v. 24, p. 5223-5231.

Wallace, A.R., 2003, Geology of the Ivanhoe Hg-Au district, Northern Nevada: Influence of Miocene volcanism, lakes, and active faulting of epithermal mineralization. Economic Geology, v. 98, p. 409-424.

Wallace, A.R., Perkins, M.E. & Fleck, R.J., 2008, Late Cenozoic paleogeographic evolution of northeastern Nevada: Evidence from the sedimentary basins. Geosphere, v. 4, no. 1, p. 36-74.

Watts, K.E., Leeman, W.P., Bindeman, I.N. & Larson, P.B., 2010, Supereruptions of the Snake River Plain: Two stage derivation of low- $\delta^{18}O$ rhyolites from normal- $\delta^{18}O$ crust as constrained by Archean xeonliths. Geology, v. 38, No. 6, p. 503-506.

Weaver, B.L., 1991, Trace element evidence for the origin of ocean-island basalts. Geology, v. 19, p. 123-126.

Whalen J.B., Currie, K.L. & Chappell, B.W., 1987, A-type granites: geochemical characteristics, discrimination and petrogenesis. Contributions to Mineralogy and Petrology, v. 95, p. 407-419.

Woods, A.W. & Huppert, H.E., 2003, On magma chamber evolution during slow effusive eruptions. Journal of Geophysical Research, v. 108, No. B8, doi: 10.1029/2002JB2019

Wright, K.E., McCurry, M. & Hughes, S., 2002, Petrology and geochemistry of the Tuff of McMullen Creek, Central Snake River Plain, Idaho, In: Tectonic and magmatic evolution of the Snake River Plain volcanic province, Bonnichsen, B., White, C.M., & McCurry, M., Idaho Geological Survey Bulletin, v. 30, pgs. 177-194.

Zoback, M.L., McKee, E.H., Blakely, R.J. & Thompson G.A., 1994, The northern Nevada rift: Regional tectono-magmatic relations and middle Miocene stress direction. Geological Society of America Bulletin, v. 106, p. 371-382.

Appendix A - Sample Locations and Petrographic Descriptions

Samples are listed in the order they were collected. Northing and Easting correspond to UTM Zone 11 T and NAD 27 CONUS. Petrologic type refers to sample locations, descriptions, petrographic descriptions (minerals are listed in order of decreasing abundances) and selected samples for point counting are listed for all collected samples relevant to the Jarbidge Rhyolite. Microscopic textures and point counted modes directly follow field descriptions for this subset.

Sample ID: JC-08-7 **Petrologic Type:** R **Map Type:** Tjr

Northing: 4631772 **Easting:** 0628071

Description: Close to road, slabby outcrop ~ 2 meters tall. Stony rhyolite, phyric, smoky corroded quartz (<8mm), well preserved sanidine (<4mm), sereticized plagioclase leaving relict shaped voids. Alternating bands of pink and grey groundmass. In thin section the sample is holocrystalline with a devitrified groundmass. Phenocryst indulde: an-subhedral fractured, embayed, chessboard extinction quartz; an-subhedral skeletal sanidine; sub-anhedral plagioclase altering to sericite and occurs as free crystals and clots; an-subhedral oxides, likely magnetite and ilmentite; anhedral altered mafics; and subhedral, boxy, and resorbed microcline. Groundmass is devitrified and cryptocrystalline (likely feldspar and quartz due to low interference colors). Eu-subhedral zircon and oxides occur in groundmass.

Sample ID: JC-08-8 **Petrologic Type:** R **Map Type:** Tjr

Northing: 4631662 **Easting:** 0627098

Description: Stony rhyolite, outcrop is slabby and protrudes as a knob from the hill side. Medium grained phyric sample with smoky corroded quartz, sanidine, and sereticized plagioclase. In thin section the sample is holocrystalline with a devitrified groundmass. Phenocryst phases included: sub-anhedral, embayed sanidine with Carlsbad twins; sub-anhedral quartz having a symplectic intergrowth with sanidine; sub-anhedral plagioclase; sub-anhedral oxides (magnetite and ilmenite); and anhedral altered mafics. Groundmass phases

include euhedral zircon, euhedral apatite as feldspar inclusion, eu-subhedral oxides, microcrystalline laths (feldspar ?) set in a devitrified groundmass.

Sample ID: JC-08-9 **Petrologic Type:** R **Map Type:** Tjr

Northing: 4631813 **Easting:** 0627195

Description: Stony rhyolite, outcrop is slabs that cropout of hill top. Sample is medium grained phyric with smoky quartz, sanidine, sereticized plagioclase, and <1mm oxidized mafics. In thin section the sample is holocrystalline with a devitrified groundmass. Phenocryst phases include: subhedral, sieved, sanidine with Carlsbad twins; an-subhedral, undulatory extinction quartz; anhedral, skeletal plagioclase; an-subhedral oxides (likely are magnetite and ilmenite); anhedral, plucked altered mafics occur in a plagioclase clots. The groundmass is cryptocrystalline, devitrified and has spherulitic texture. Anhedral quartz(?) blobs occur. Groundmass phases are euhedral zircon and euhedral apatite which occur in plagioclase clots, and zircon occurs as an independent crystals.

Sample ID: JC-08-10 **Petrologic Type:** R **Map Type:** Tjr

Northing: 4631561 **Easting:** 0627116

Description: Vitrophyre, waxy luster, float found in road. Medium grained phyric smoky quartz, sanidine, and sereticized plagioclase and perlitic texture. A flow foliation of sheared vitrophyre may be seen under hand lens.

Mode: Crystallinity (20.43), sanidine (8.59), quartz (6.39), plagioclase (4.27), pyroxenes (1.08), groundmass (GM)(79.98). Sanidine is sun-anhedral, embayed and boxy crystasl; quartz displays embayments and ocelli; plagioclase is an-subhedral embayed and skeletal crystals. The groundmass is trachytic, and displays flowbanding.

Sample ID: JC-08-11 **Petrologic Type:** R **Map Type:** Tjr

Northing: 4629900 **Easting:** 0626820

Description: Stony rhyolite outcrop with horizontal and vertical joints, approximately 5 meters tall. Phyric medium grained smoky quartz, medium and coarse grained sanidine, and medium grained plagioclase with grey-blue matrix, with oxidation

staining bands similar to lisengang banding. In thin section the sample is holocrystalline with a devitrified groundmass. Phenocryst include: eu-anhedral, embayed, resorbed, ocelli quartz; anhedral sanidine; plagioclase is anhedral, skeletal, and displays myrmektitic and symplectic intergrowth with quartz; oxides are subhedral. The groundmass is microcrystalline. Euhedral zircon and euhedral apatite occur as inclusions. Anhedral zircon is an independent crystal in groundmass. Subhedral oxides are present.

Sample ID: JC-08-12 **Petrologic Type:** R **Map Type:** Tjr

Northing: 4627812 **Easting:** 0626200

Description: Stony rhyolite outcrop, weathering along horizontal joints, display liesegne banding and is found near hill crest. Medium grained phyric stony rhyolite, smoky quart, slightly weathered sanidine, and sereticized plagioclase in a green grey groundmass. In thin section the sample is holocrystalline with a devitrified groundmass. Phenocryst phases include: anhedral, boxy, sieved, sanidine intergrown with plagioclase; anhedral plagioclase with symplectic intergrowths with sanidine; anhedral, fractured, rounded quartz; biotite is a kata-alteromorph; anhedral Fe-Ti oxides. Microcline occurs as anhedral crystals, and an anit rapakivi texture is observed. The groundmass is devitrified with microcrystalline anhedral crystallites. Groundmass phases are: sub-euhedral apatite and zircon crystals.

Sample ID: JC-08-13 **Petrologic Type:** R **Map Type:** Tjr

Northing: 4627777 **Easting:** 0626014

Description: Phyric devitrified, waxy luster, vitrophyre with medium grained smoky quartz, medium and coarse grained sanidine, and medium and coarse grained sereticized plagioclase. Crops out of ground in a saddle. Vitrophyre and stony rhyolite contact noted at this location. In thin section the sample is hypocrystalline with a glass groundmass. Phenocryst phases include: sub-anhedral boxy, with crystallographically controlled plagioclase inclusions in sanidine;.anhedral embayed, rounded, fracture, quartz; anhedral skeletal

plagioclase; biotie as anhedral, plucked, kata-alteromorph altered clinopyroxene; eu-anhedral oxides (likely magnetite and ilmenite). A single anhedral, slightly plucked serpentine crystal is noted. The groundmass is devitrified with pilotaxitic feldspar laths. Euhedral apatite, zircon and hematite (?) also occur. Apatite inclusions within biotite are fracture across intramineral fissures.

Sample ID: JC-08-14 **Petrologic Type:** TB **Map Type:** Tb_2

Northing: 4623553 **Easting:** 0628096

Description: Phyric basalt with plagioclase and oxidized mafics. Pegmatitic plagioclase crystals (<4.5 cm). Outcrop is rounded knobs. JC-08-14 B is a xenolith found in the outcrop. In thin section plagioclase is eu-subhedral and subophitic, olivine is an-subhedral, titanaugite is anhedral, and Fe-Ti oxides are present. The groundmass is plagioclase laths.

Sample ID: JC-08-15 **Petrologic Type:** TB **Map Type:** Tb_2

Northing: 4623475 **Easting:** 0623475

Description: Phyric basalt with plagioclase and oxidized mafics. Pegmatitc plagioclase crystals. Outcrop is rounded knobs. Plagioclase is several populations, the larger ones display resorbed, subophitic, titanaugite is anhedral, olivine is subhedral, and Fe-Ti oxides are subhedral.

Mode: Plagioclase (65.93), titanaugite (18.47), olivine (13.54), and oxides (2.05).

Sample ID: JC-08-16 **Petrologic Type:** TB **Map Type:** Tb_2

Northing: 4623126 **Easting:** 0628045

Description: Phyric basalt with plagioclase and oxidized mafics. Pegmatitc plagioclase crystals and sample JC-09-EN was sampled from this outcrop. Plagioclase is eu-subhedral and has multiple populations, larger crystals are sieved, titanugite is anhedral, orthopyroxene is anhedral, olivine is eu-subhedral, and Fe-Ti oxides are subhedral.

Sample ID: JC-08-18 **Petrologic Type:** R **Map Type:** Tjr

Northing: 4622286 **Easting:** 0627207

Description: Medium grained phyric vitrophyre with perlitic fracture and brown orange matrix host smoky quartz, sanidine, and plagioclase phenocryst. Multiple bodies in area display spherodial weathering and spires. In thin section the sample is holocrystalline with a devitrified groundmass. Phenocryst include an-subhedral, boxy, sieved sanidine; an-subhedral embayed, rounded, intramineral fractured, quartz with ocelli; an-subhedral boxy plagioclase; anhedral oxides (magnetite and ilmenite), and anhedral altered mafics. Groundmass phases include anhedral zircon; euhedral apatite; subhedral oxides (magnetite and ilmenite); and cryptocrystalline phases.

Sample ID: JC-08-20 **Petrologic Type:** R **Map Type:** Tjr

Northing: 4606260 **Easting:** 0624540

Description: Monolithic stony rhyolite flow breccia. Medium grained phyric phases include medium grained smoky quartz, medium grained sanidine, medium and coarse grained sereticized plagioclase, and red oxidized mafic. Note of vitrophyre float was taken.

Mode: Crystallinity (32.51), quartz (10.05), sanidine (9.29), plagioclase (9.00), oxides (0.52), garnet (3.00), microcline (0.65), and GM (67.49).

Quartz is embayed, sanidine and plagioclase are embayed and skeletal. Clots of all four major phases are found. Additionally, garnet is at the core of plagioclases. Accessory phases include zircon, apatite, and sphere (?).

Sample ID: JC-08-24 **Petrologic Type:** R **Map Type:** Tjr

Northing: 4619700 **Easting:** 0591852

Description: Outcrop of phyric stony rhyolite from river valley. Phenocryst are medium grained and consist of smoky quartz and weathered, yellowed sanidine are the phyric phases.

Mode: Crystallinity (34.88), quartz (12.15), sanidine (11.49), plagioclase (10.56), oxides (0.66), and GM (65.12). Quartz displays ocelli, sanidine is embayed and has intergrowth with plagioclase, and plagioclase is skeletal. Accessory phases include zircon and apatite.

Sample ID: JC-08-25 **Petrologic Type:** R **Map Type:** Tjr

Northing: 4620752 **Easting:** 0602571

Description: Outcrop of spires in hill side. Grey purplish matrix with medium grained phyric phases of smoky quartz, sanidine, and sereticized plagioclase.

Mode: Crystallinity (39.59), sanidine (16.50), quartz (16.24), plagioclase (5.71), hornblende (0.63), oxyhornblende (0.3), oxides (0.25), and GM (60.41). Zircon and apatite are observed as well. Sanidine is skeletal with granophyre intergrowth, quartz is an-subhedral and embayed, plagioclase is an-subhedral and skeletal, hornblende and oxyhornblede are discreet crystals expressing alteration, and oxides are magnetite and ilmenite. In groundmass, lath oxides are extremely flow orientated, wrapping around crystals and infilling embayments.

Sample ID: JC-08-26 **Petrologic Type:** R **Map Type:** Tjr

Northing: 4613113 **Easting:** 0601145

Description: Stony rhyolite interior of road cut, may be portion of a flow margin. Medium grained phyric phases are smoky quartz, sanidine, and sereticized plagioclase. In thin section subhedral sieved sanidine; an-euhedral, rounded, intramineral fractured quartz with ocelli, subhedral plagioclase with clots, and anhedral serpentine. Groundmass phases include: euhedral zircon, subhedral oxides, and hematite, and euhedral sphere (?).

Sample ID: JC-09-2 **Petrologic Type:** R **Map Type:** Tjr

Northing: 4628256 **Easting:** 0627259

Description: Stony phyric rhyolite outcrop at hill top with spherodial weathering and concentric weathering rinds. Outer surface is white-bluish and groundmass is blackish with medium grained phyric phases of smoky quartz, sanidine, and sereticized plagioclase. In thin section the sample is holocrystalline with a

cryptocrystalline groundmass. Phenocryst phases include anhedral sanidine with crystallographically controlled plagioclase inclusions; anhedral embayed, intramineral fractured quartz with ocelli; anhedral plagioclase which may form clots; anhedral oxides (magnetite and ilmenite), sub-anhedral, sieved clinopyroxene as independent crystals and clots. Groundmass phases include sub-euhedral zircon, apatite, and oxides (magnetite and ilmenite).

Sample ID: JC-09-3 **Petrologic Type:** R **Map Type:** Tjr

Northing: 4628072 **Easting:** 0627007

Description: Stony rhyolite slab from western slope. Medium grained phyric phases included smoky quartz, sanidine, and serectized plagioclase. The matrix is discolored, grey and brown. In thin section the sample is holocrystalline with a devitrified groundmass. Phenocryst phases include: sub-anhedral boxy, sieved, granophyre sanidine; an-subhedral, rounded, intramineral fractured, ocelli and embayed quartz; subhedral skeletal plagioclase; anhedral, plucked altered mafics within plagioclase clots; and subhedral oxides (likely magnetite and ilmenite). Accessory phases include euhedral zircon and apatite.

Sample ID: JC-09-4 **Petrologic Type:** R **Map Type:** Tjr

Northing: 4627950 **Easting:** 0626884

Description: Stony rhyolite crops out as slabs, and flow foliation of alternating pink and pinkish grey layers and trachytic texture are observed. Phyric phases include smoky quartz, sanidine and sereticized plagioclase. In thin section the sample is holocrystalline with a devitrified groundmass. Phenocryst include: anhedral sanidine with inclusion rims, and crystallographically controlled plagioclase inclusions; anhedral, ocelli, and intramineral fractured quartz; anhedral, boxy, embayed plagioclase; subhedral oxides (likely magnetite and ilmenite), and anhedral altered mafics. Groundmass phases include eu-subhedral zircon; subhedral apatite, and dissolved blebs of quartz (?).

Mode: Crystallinity (20.62), quartz (11.50), sanidine (5.38), plagioclase (3.25), pyroxenes (0.12), oxides (0.38), and GM (79.38). Quartz is anhedral with symplectic intergrowth

with sanidine, sanidine is an-subhedral with embayments, resportions and inclusion, plagioclase is anhedral with concentric zoning and boxy texture, and oxides are magnetite and ilmenite. Accessory phases are zircon and apatite.

Sample ID: JC-09-5 **Petrologic Type:** R **Map Type:** Tjr

Northing: 4627924 **Easting:** 0626646

Description: Devitrified **v**itrophyre rounded knobs outcrop from southwest facing hillside. Trachytic texture is displayed. Medium grained phyric phases include smoky quartz, sanidine and seriticizied plagioclase. In thin section the sample is hypocrystalline with a partly devitrified groundmass. Phenocryst phases include: subhedral, skeletal, sanidine with crystallographically controlled plagioclase inclusions; anhedral, embayed, chessboard extinction quartz; an-subhedral, skeletal plagioclase as clots and independent crystals, and anhedral altered mafics. The groundmass partly devitrified to brown clays, and primary phases are euhedral zircon and euhedral apatite.

Sample ID: JC-09-6 **Petrologic Type:** R **Map Type:** Tjr

Northing: 4627936 **Easting:** 0626549

Description: Outcrop of phyric stony rhyolite slabs from west facing slope. Medium grained phyric phases include smoky quartz, sanidine, and sereticized plagioclase. In thin section the sample is hypocrystalline with a glassy groundmass. Phenocryst phases include: subhedral, sieved sanidine with plagioclase inclusions; subhedral, rounded, intramineral fractured, undulatory extinction quartz;; subhedral, sieved, clot forming plagioclase; subhedral oxides (magnetite and ilmenite); and anhedral, kata-alteromorph altered mafics. The groundmass has a flow foliation and phases are sub-anhedral zircon, and euhedral apatites.

Sample ID: JC-09-7 **Petrologic Type:** R **Map Type:** Tjr

Northing: 4627917 **Easting:** 0626431

Description: Phyric stony rhyolite, platy south facing outcrop. Phyric phases include medium grained smoky quartz, medium grained sanidine, and coarse and medium

grained sereticized plagioclase. Large feldspar 3.8 cm long in one dimension was found in the stony rhyolite. In thin section the sample is holocrystalline with a devitrified groundmass. Phenocryst phases include: anhedral, rounded, intramineral fractured, embayed, ocelli quartz; subhedral, sieved, skeletal sanidine with plagioclase inclusions; anhedral, skeletal, sieved plagioclase and some crystals have biotite inclusions; subhedral, boxy microcline with mafic inclusions; subhedral oxides (magnetite and ilmenite); and anhedral, kata-alteromorph biotite. Groundmass phases include anhedral apatite and zircon.

Sample ID: JC-09-8 **Petrologic Type:** R **Map Type:** Tjr

Northing: 4616651 **Easting:** 0627427

Description: Phyric stony rhyolite from north facing slope below summit with local spherodial weathering. Slabby float from above with medium grained phyric phases of quartz, sanidine, and seriticized plagioclase.

Mode: Quartz (16.73), sanidine (14.11), plagioclase (3.00), zircon (0.13), oxides (0.13), and GM (65.88). In thin section the sample is holocrystalline with devitrified groundmass. Phenocryst phases include: anhedral, rounded, intramineral fractured, embayed, ocelli quartz; subhedral resorbed, sieved sanidine; subhedral boxy, resorbed, clot forming plagioclase, and an-euhedral oxides (magnetite and ilmenite). Groundmass phases include: euhedral zircon; anhedral apatite, and secondary micas.

Sample ID: JC-09-9 **Petrologic Type:** R **Map Type:** Tjr

Northing: 4617012 **Easting:** 0627089

Description: Phyric stony rhyolite protruding from ground as joints. Medium grained phyric phases include smoky quartz, sanidine, sereticized plagioclase, and oxidized mafics. The groundmass is purplish blue. In thin section the sample is holocrystalline with a devitrified groundmass. Phenocryst phases include: anhedral, embayed, intramineral fractured, rounded quartz; sub-anhedral, concentrically zoned, resorbed sanidine which displays Carlsbad twins; anhedral, resorbed plagioclase; anhedral, resorbed oxides (magnetite and ilmenite); and anhedral altered mafics. Groundmass phases include: subhedral zircon; anhedral

oxides (magnetite and ilmenite); and euhedral apatite as quartz inclusions.

Sample ID: JC-09-10A **Petrologic Type:** R **Map Type:** Tjr

Northing: 4617099 **Easting:** 0626907

Description: Brecciated upper vitrophyre with vitrophyre clasts in ashy matrix. In thin section the sample is hypocrystalline with a glassy matrix. Vitrophyre clasts are angular and have pilotaxitic texture. Phenocryst are shattered but displacement from is not significant, given that crystal clast occur as discrete groups. Vitrophyre clasts have pilotaxitic feldspar laths of comparable size to those found in JC-09-10B & 12. Mineral phases include: anhedral seriate quartz; anhedral altered mafics; an-subhedral skeletal sanidine with crystallographically controlled embayments; anhedral plagioclase; subhedral oxides; and subhedral microcline. Groundmass phases include subhedral zircon; glass chips; and euhedral apatite

Sample ID: JC-09-10B **Petrologic Type:** R **Map Type:** Tjr

Northing: 4617098 **Easting:** 0626907

Description: Partially devitrified phyric vitrophyre with medium grained smoky quartz, medium grained sanidine, medium and coarse grained slightly yellowed plagioclase, and fine grained oxidized mafics.

Mode: Quartz (4.39), sanidine (1.60), plagioclase (14.11), clinopyroxene (2.12), oxides (0.80), microcline (4.53), and GM (72.44). In thin section the sample is hypocrystalline with a glassy groundmass with pilotaxitic texture. Phenocryst phases include: Anhedral, boxy, clot forming plagioclase; anhedral, sieved, boxy microcline; anhedral, embayed, rounded, intramineral fractured quartz; eu-anhedral cumulophyric clinopyroxene; and anhedral oxides (magnetite and ilmentie). In groundmass some of the glass has devitrified to brown cryptocrystalline clays and displays perlitic fracture; sub-anhedral zircon; eu-subhedral apatite; and euhedral feldspar laths.

Sample ID: JC-09-11 **Petrologic Type:** R **Map Type:** Tjr

Northing: 4617104 **Easting:** 0626811

Description: Stony rhyolite lava flow displaying internal shearing. Phyric phases included medium grained rounded corroded smoky quartz, medium grained slightly weathered sanidines, and medium and coarse grained seretizied plagioclase. In thin section the sample is holocrystalline with a devitrified groundmass. Phenocryst phases include: subhedral boxy plagioclase; sanidine; anhedral embayed, intramineral fracture, rounded quartz; anhedral boxy, sieved microcline; anhedral oxides (magnetite and ilmenite). Groundmass phases include: euhedral feldspars, euhedral zircon; euhedral apatite and anhedral oxides.

Sample ID: JC-09-12 **Petrologic Type:** R **Map Type:** Tjr

Northing: 4617085 **Easting:** 0626785

Description: Partially devitrified vitrophyre which grades into JC-09-11. Phyric phases include medium and coarse grained seretizied plagioclase, medium grained corroded and rounded smoky quartz, and medium grained sanidine. In thin section the sample is hypocrystalline with a glassy groundmass. Phenocryst phases include: subhedral boxy plagioclase; embayed, intramineral fracture, rounded quartz; anhedral boxy, resorbed sanidine; anhedral oxides and anhedral altered mafics. Groundmass displays perlitic fracture and is partly devitrified to brown clays. Groundmass phases include: euhedral, pilotaxitic feldspar; and euhedral apatite.

Sample ID: JC-09-13 **Petrologic Type:** R **Map Type:** Tjr

Northing: 4617304 **Easting:** 0626530

Description: Stony rhyolite from hillside weathering to slabs. Medium grained phyric phases are corroded, rounded smoky quartz, sanidine and sereticized plagioclase. In thin section the sample is holocrystalline with a devitrified groundmass. Phenocryst phases are: subhedral sieved sanidine; anhedral, sieved plagioclase (one crystal cores a sanidine); anhedral, rounded, intramineral fracture, embayed, ocelli quartz; anhedral sieved microcline with biotite inclusions; anhedral,

partially plucked; intramineral fissures altered mafics (biotite ?); anhedral microcline and anhedral oxides (magnetite and quartz).

Sample ID: JC-09-14 **Petrologic Type:** R **Map Type:** Tjr

Northing: 4617462 **Easting:** 0626417

Description: Phyric stony rhyolite with apparent alteration. Medium grained phyric phases include smoky rounded quartz, sanidine, and sereticized plagioclase. Phenocryst phases include: anhedral, embayed, rounded, intramineral fractured, ocelli quartz; anhedral sieved, skeletal, embayed sanidine; subhedral sieved plagioclase; subhedral microcline; an-subhedral kata alteromorph biotite. Groundmass phases include euhedral apatite; euhedral zircon; and euhedral sphene(?).

Sample ID: JC-09-15 **Petrologic Type:** R **Map Type:** Tjr

Northing: 4600283 **Easting:** 0601263

Description: Phyric stony rhyolite with spherodial weathering that follows joints. Phyric phases are medium grained rounded, corroded smoky quartz, medium grained sanidine and medium and coarse grained plagioclase. In thin section the sample is holocrystalline with a devitrified groundmass. Phenocryst phases include: anhedral, embayed, rounded, intramineral fractured, ocelli quartz; sub-anhedral, sieved, myrmektitc, boxy, and clot forming plagioclase; an-subhedral oxides; and anhedral altered mafics. Groundmass phases include: subhedral zircon; euhedral apatite; subhedral oxides and euhedral feldspar laths.

Mode: Quartz (12.66), sanidine (4.52), plagioclase (9.30), zircon (0.46), oxides (0.91), altered pyroxenes (1.29), and GM (71.83).

Sample ID: JC-09-16 **Petrologic Type:** R **Map Type:** Tjr

Northing: 4615934 **Easting:** 0598102

Description: Partially devitrified phyric vitrophyre with medium grained phyric phases of yellowed, slightly weathered plagioclase and sanidine. In thin section the

sample is hypocrystalliine with a glassy groundmass displaying flow foliation and perlitic fracture. Phenocryst phases include; an-subhedral rounded, intramineral fractured, embayed quartz; anhedral, embayed, sieved, sanidine; subhedral, embayed, boxy, clot forming plagioclase; anhedral embayed altered mafic (biotite ?) with apatite and oxides inclusions and intramineral fissures along cleavage planes; anhedral serpentine; and oxides (magnetite and ilmenite). Groundmass phases include: perlitic, partially devitrified to brown clays glass; euhedral apatite; euhedral zircon; and euhedral sphere (?).

Sample ID: JC-09-17 **Petrologic Type:** R **Map Type:** Tjr

Northing: 4631173 **Easting:** 0608066

Description: Stony rhyolite flow interior with minor joints and slightly silicified. Phyric phases are coarse grained include rounded corroded smoky quartz, and slightly weathered sanidine and plagioclase. Approximately 20 % phyric phases and 80% groundmass.

Mode: Quartz (10.84), sanidine (11.35), plagioclase (2.45), oxides (0.13), altered mafics (0.77), and GM (74.45). In thin section the sample is holocrystalline with a devitrified groundmass. Phenocryst phases include: subhedral, embayed, intramineral fractured, sieved, ocelli quartz; sub-euhedral, skeletal sanidine; subhedral, boxy plagioclase; subhedral oxides (magnetite and ilmenite). Groundmass phases include: euhedral zircon; euhedral apatite, and micas (?). Several cumulophyric clots of quartz, sanidine, and alkali feldspar occur, and are believed to be silicic xenoliths due to crystal form and resorbtion textures.

Sample ID: JC-09-18 **Petrologic Type:** R **Map Type:** Tjr

Northing: 4630336 **Easting:** 0607886

Description: Slightly devitrified phyric vitrophyre float below vitrophyre outcrop on south facing slope. Phyric phases are coarse grained and include rounded, corroded smoky quartz, sandine, and sereticized plagioclase. In thin section the sample is hypocrystalline with a glassy groundmass dislaying flow folitation and spherulitic textures. Phenocryst phases include: anhedral, embayed quartz;

subhedral, embayed sanidine; anhedral, sieved, boxy, clot forming plagioclase; anhedral clinopyroxene; OXIDES. Groundmass phases include: euhedral feldspar laths, euhedral zircon, euhedral apatite, and subhedral oxides.

Sample ID: JC-09-19 **Petrologic Type:** B **Map Type:** Tb_2

Northing: 4623693 **Easting:** 0603659

Description: Basalt capping unit with extensive chalcedony, amygdaloidal, and phyric. Plagioclase crystals may be up to 1 cm. In thin section the sample is holocrystalline. Phenocryst phases include: bimodal size plagioclase population, large plagioclase crystals are sub-euhedral and sieved and the small population is sub-euhedral inclusions in titanaugite; anhedral, oikacryst of titanugite; anhedral olivine; and subhedral oxides (ilmenite and magnetite).

Sample ID: JC-09-20 **Petrologic Type:** B **Map Type:** Tb_2

Northing: 4625109 **Easting:** 0598310

Description: Basaltic vent with scoria, indications of phreatic magmatism, and phyric. Phyric phases are plagioclase and red oxidized mafics. In thin section the sample is holocrystalline with crystalline groundmass. Phenocryst include: three populations of plagioclase by size fraction. The largest population is euhedral and partially sieved, the next smallest population is subhedral and sieved, and the groundmass population is sub-euhedral. Anhedral titanaugite and subhedral olivine also occur.

Sample ID: JC-09-21A **Petrologic Type:** B **Map Type:** Tjr

Northing: 4621420 **Easting:** 0599562

Description: Phyric **s**tony rhyolite from hill side. Phyric phases are medium grained and include rounded corroded smoky rhyolite, plagioclase, oxidized mafics in a grey matrix.

Mode: Quartz (11.64), sanidine (12.87), plagioclase (7.53), oxides (0.96), altered mafics (1.23), and GM (65.75). In thin section the sample is holocrystalline with a devitrified groundmass. Phenocryst phases include subhedral, embayed, sieved, seriate sanidine;

anhedral, embayed, rounded, intramineral fractured, ocelli quartz; eu-subhedral boxy, sieved, seriate plagioclase; and sub-anhedral oxides (ilmenite and magnetite). Groundmass phases include: subhedral oxides (magnetite and ilmenite); euhedral apatite; and euhedral zircon.

Sample ID: JC-09-21B **Petrologic Type:** R **Map Type:** Tjr

Northing: 4621420 **Easting:** 0599562

Description: Coarsely phyric stony rhyolite with coarse grained plagioclase crystals, coarse grained sanidine, and medium grained smoky quartz. In thin section the sample is holocrystalline with a devitrified groundmass. Phenocryst phases include: anhedral, embayed, boxy sanidine; subhedral, sieved, boxy plagioclase; sub-anhedral rounded, intramineral fractures, embayed quartz; and subhedral oxides (magnetite and ilmenite).

Sample ID: JC-09-22 **Petrologic Type:** R **Map Type:** Tjr

Northing: 4548547 **Easting:** 0666387

Description: Phyric stony rhyolite outcrop below crest of hills. Phyric phases are medium grained and include rounded, corroded smoky quartz, sanidine, altered plagioclase and oxidized mafics. In thin section the sample is holocrystalline with a devitrified groundmass. Phenocryst phases include anhedral skeletal sanidine with plagioclase inclusions; anhedral, embayed quartz; an-subhedral, boxy plagioclase; anhedral altered mafics; anhedral, fractured garnets; and subhedral oxides (magnetite and ilmenite). Groundmass phases include: euhedral oxides (magnetite and ilmenite); subhedral zircon; and euhedral apatite.

Sample ID: JC-09-EN **Petrologic Type:** A **Map Type:**

Northing: 4623126 **Easting:** 0628045

Description: Rounded aphyric xenolith in Seventy Six basalt. Lighter color than surrounding basalt. In thin section all phases are seriate and the groundmass is cryptocrystalline low interference colors and many small opaques are present. Mineral phases are: subhedral, concentrically zone plagioclase that may or may

not be weathering to brown clays; anhedral quartz (one polygonal clot of quartz); and subhedral oxides.

Appendix B - Geochemistry

Samples not listed, JC-08-11, 18, JC-09-7, 10A, and 13, did not have any chemical analysis completed and are not listed below. The symbol "---" indicates that element was not determined for the sample. Major and some trace elements were determined by DCP-AES for all samples with chemical data. Rare earth element concentrations were determined for a subset of these, and those elements which do not have REE data are not listed for that portion.

DCP-AES Major Element Results (wt. %)

Sample	JC-08-7	JC-08-8	JC-08-9	JC-08-10	JC-08-12	JC-08-13
SiO_2	76.81	76.68	76.61	74.45	73.68	73.51
TiO_2	0.32	0.26	0.29	0.28	0.41	0.37
Al_2O_3	12.60	12.53	12.66	12.14	12.78	12.58
Fe_2O_3	0.44	0.55	0.43	1.14	1.71	1.22
FeO	0.32	0.41	0.31	0.86	1.38	0.98
MnO	0.01	0.00	0.00	0.02	0.02	0.03
MgO	0.02	0.02	0.03	0.06	0.07	0.06
CaO	0.72	0.69	0.84	0.97	1.28	1.43
Na_2O	2.82	2.93	3.02	2.68	3.04	2.53
K_2O	5.40	5.50	5.58	5.55	4.84	5.44
P_2O_5	0.02	0.04	0.04	0.03	0.05	0.06
Total	100.00	100.00	100.00	100.00	100.00	100.00
LOI	0.47	0.35	0.17	1.73	0.59	1.69

Sample	JC-08-14	JC-08-15	JC-08-16	JC-08-20	JC-08-24	JC-08-25
SiO_2	49.00	48.96	49.43	76.28	74.55	75.77
TiO_2	1.85	1.82	1.86	0.38	0.36	0.18
Al_2O_3	18.24	18.25	18.43	12.49	13.48	13.02
Fe_2O_3	4.22	4.17	4.13	0.94	0.74	0.76
FeO	6.57	6.52	6.49	0.72	0.56	0.58
MnO	0.17	0.17	0.17	0.02	0.01	0.02
MgO	4.24	4.40	4.14	0.04	0.06	0.04
CaO	8.31	8.20	8.32	1.17	1.40	0.79
Na_2O	3.92	3.66	3.86	3.00	2.95	2.58
K_2O	1.45	1.67	1.43	4.88	5.50	5.55
P_2O_5	0.53	0.52	0.53	0.07	0.07	0.03
Total	100.00	100.00	100.00	100.00	100.00	100.00
LOI	0.76	0.92	0.48	0.40	0.27	0.60

DCP-AES Major Element Results

Sample	JC-08-26	JC-09-2	JC-09-3	JC-09-4	JC-09-5	JC-09-6
SiO_2	77.06	75.11	76.34	76.88	75.99	76.31
TiO_2	0.22	0.28	0.28	0.25	0.24	0.24
Al_2O_3	12.51	11.98	12.55	12.41	12.31	12.62
Fe_2O_3	0.43	1.49	0.72	0.52	1.07	0.74
FeO	0.31	1.18	0.54	0.38	0.80	0.54
MnO	0.00	0.03	0.01	0.00	0.02	0.01
MgO	0.02	0.10	0.02	0.01	0.05	0.02
CaO	0.63	0.99	0.72	0.70	0.83	0.66
Na_2O	2.86	2.87	2.96	2.96	2.97	2.90
K_2O	5.62	5.20	5.51	5.56	5.37	5.54
P_2O_5	0.01	0.03	0.04	0.04	0.02	0.03
Total	100.00	100.00	100.00	100.00	100.00	100.00
LOI	0.28	0.59	0.24	0.25	0.23	0.33

Sample	JC-09-8	JC-09-9	JC-09-10B	JC-09-11	JC-09-12	JC-09-14
SiO_2	77.76	76.45	71.51	73.00	72.04	73.77
TiO_2	0.17	0.30	0.41	0.43	0.41	0.38
Al_2O_3	12.03	12.15	12.77	13.47	13.28	12.43
Fe_2O_3	0.32	1.04	1.79	1.59	1.40	1.98
FeO	0.24	0.78	1.49	1.26	1.15	1.64
MnO	0.00	0.01	0.05	0.02	0.03	0.01
MgO	0.02	0.03	0.13	0.04	0.05	0.08
CaO	0.69	0.70	1.70	1.29	1.60	1.01
Na_2O	3.02	2.81	2.68	3.22	3.00	2.77
K_2O	5.42	5.30	5.34	5.06	5.22	5.03
P_2O_5	0.03	0.03	0.09	0.09	0.08	0.07
Total	100.00	100.00	100.00	100.00	100.00	100.00
LOI	0.26	0.31	1.87	0.39	1.60	0.64

DCP-AES Major Element Results

Sample	JC-09-15	JC-09-16	JC-09-17	JC-09-18	JC-09-19	JC-09-20
SiO_2	73.63	74.28	75.81	73.00	50.32	50.36
TiO_2	0.47	0.21	0.26	0.24	1.88	1.90
Al_2O_3	13.80	12.03	12.24	12.63	16.00	15.85
Fe_2O_3	0.91	1.06	1.01	1.17	4.68	4.50
FeO	0.72	0.86	0.76	0.90	7.73	7.68
MnO	0.01	0.02	0.01	0.03	0.18	0.19
MgO	0.03	0.05	0.04	0.05	5.56	5.27
CaO	1.56	0.89	0.74	0.85	7.87	8.26
Na_2O	2.92	2.35	2.92	2.75	3.02	2.85
K_2O	5.48	5.70	5.50	6.07	1.24	1.15
P_2O_5	0.11	0.03	0.08	0.06	0.46	0.46
Total	100.00	100.00	100.00	100.00	100.00	100.00
LOI	0.28	2.39	0.54	2.13	0.20	0.66

Sample	JC-09-21A	JC-09-21B	JC-09-22	JC-09-En
SiO_2	74.49	75.10	76.98	61.03
TiO_2	0.33	0.31	0.37	0.80
Al_2O_3	13.81	13.38	11.92	19.95
Fe_2O_3	0.68	0.63	0.77	2.62
FeO	0.51	0.48	0.60	3.57
MnO	0.01	0.01	0.01	0.08
MgO	0.05	0.05	0.05	1.47
CaO	1.21	1.10	0.96	4.09
Na_2O	2.97	2.85	2.82	2.20
K_2O	5.49	5.50	5.05	2.24
P_2O_5	0.07	0.07	0.08	0.20
Total	100.00	100.00	100.00	100.00
LOI	0.34	0.48	0.33	1.35

DCP-AES Trace Element Results (ppm)

Sample	JC-08-7	JC-08-8	JC-08-9	JC-08-10	JC-08-12	JC-08-13
Ba	1054	535	990	721	2108	2010
Cr	3	4	1	1	6	3
Cu	6	3	4	8	8	10
Nb	22.3	24.9	29.1	20.8	22.7	26.0
Ni	2	21	4	8	9	1
Rb	176	222	201	210	132	163
Sr	94	49	84	68	173	158
Sc	5.7	4.1	4.6	6.0	7.5	8.0
V	3	2	0	21	15	6
Y	44	33	29	45	21	41
Zn	51	73	93	70	90	98
Zr	323	375	353	372	372	387

Sample	JC-08-14	JC-08-15	JC-08-16	JC-08-20	JC-08-24	JC-08-25
Ba	717	751	730	1894	1834	560
Cr	21	27	26	3	5	2
Cu	25	27	25	6	4	6
Nb	---	---	---	25.8	19.9	22.5
Ni	20	22	20	8	6	1
Rb	28	42	28	20	11	239
Sr	566	602	582	406	418	77
Sc	22.5	23.1	21.3	29.3	31.8	5.7
V	102	103	101	155	166	10
Y	36	38	36	40	45	58
Zn	82	125	140	126	137	48
Zr	192	230	211	272	281	223

DCP-AES Trace Element Results

Sample	JC-08-26	JC-09-2	JC-09-3	JC-09-4	JC-09-5	JC-09-6
Ba	760	888	759	532	527	388
Cr	5	3	2	9	3	0
Cu	3	6	3	3	6	2
Nb	18.6	22.9	22.0	25.2	25.4	16.5
Ni	2	23	22	14	24	13
Rb	188	180	188	243	241	167
Sr	70	71	59	47	46	35
Sc	5.1	4.7	4.1	3.3	3.8	2.7
V	7	0	0	1	0	0
Y	39	76	34	33	46	23
Zn	48	72	65	62	57	37
Zr	258	405	417	387	397	279

Sample	JC-09-8	JC-09-9	JC-09-10B	JC-09-11	JC-09-12	JC-09-14
Ba	408	943	2235	2433	2414	1966
Cr	3	11	8	5	6	4
Cu	2	6	6	7	6	7
Nb	27.0	20.1	19.1	21.3	22.8	20.9
Ni	11	20	24	18	21	22
Rb	254	184	131	140	139	161
Sr	42	69	164	177	186	142
Sc	2.9	4.7	6.4	6.8	6.9	6.3
V	0	4	0	0	0	0
Y	43	33	38	44	40	37
Zn	65	61	81	67	96	73
Zr	306	408	434	492	454	509

DCP-AES Trace Element Results

Sample	JC-09-15	JC-09-16	JC-09-17	JC-09-18	JC-09-19	JC-09-20
Ba	2715	743	565	516	688	727
Cr	6	6	0	1	59	61
Cu	5	4	5	8	59	61
Nb	27.4	17.7	23.7	21.6	32.9	36.4
Ni	32	16	18	21	34	35
Rb	133	198	229	229	20	11
Sr	328	59	55	45	34	35
Sc	8.4	4.3	3.9	4.0	29.3	31.8
V	4	0	0	1	20	11
Y	52	42	56	48	406	418
Zn	92	58	65	81	29	32
Zr	660	324	405	380	155	166

Sample	JC-09-21A	JC-09-21B	JC-09-22	JC-09-En
Ba	1597	1581	1798	825
Cr	4	3	4	95
Cu	4	3	4	26
Nb	22.3	18.5	21.9	24.6
Ni	10	13	19	29
Rb	184	180	155	116
Sr	173	165	131	479
Sc	6.6	6.0	4.1	18.2
V	6	4	3	95
Y	39	39	31	41
Zn	57	61	74	95
Zr	360	338	441	232

ICP-MS Trace Element Results (ppm)

Sample	JC-08-10	JC-08-15	JC-08-20	JC-08-24	JC-08-25	JC-09-4
Li	31.7	8.34	14.5	20.6	18.1	23.2
Be	3.95	1.33	2.18	3.33	4.18	4.05
Co	1	33	1	1	1	1
Ga	20.6	20.8	20.2	22.3	22.7	20.7
As	0.706	0.68	1.41	LDL	1.42	0.983
Mo	1.52	LDL	0.634	1.08	1.5	0.22
Sn	4.11	1.11	2.51	3.21	3.95	4.53
Sb	0.037	LDL	0.044	0.035	0.068	0.055
Cs	2.84	0.71	1.48	1.46	1.76	2.65
La	94.5	32.6	75.2	83.6	110.0	85.7
Ce	171.0	66.9	139.0	157.0	209.0	129.0
Pr	18.20	8.16	14.90	18.00	24.60	16.40
Nd	64.90	34.80	53.90	65.00	89.90	56.90
Sm	11.60	7.74	9.65	11.70	16.90	10.10
Eu	0.84	2.24	2.01	1.92	0.84	0.64
Gd	10.60	7.38	8.81	9.77	14.80	8.69
Tb	1.45	1.13	1.16	1.28	2.03	1.18
Dy	8.01	6.60	6.24	6.58	10.90	6.37
Ho	1.56	1.30	1.20	1.19	2.06	1.21
Er	4.64	3.74	3.52	3.46	5.99	3.71
Tm	0.65	0.52	0.50	0.47	0.83	0.53
Yb	4.53	3.60	3.48	3.21	5.63	3.71
Lu	0.66	0.53	0.51	0.46	0.81	0.54
Hf	11.40	5.08	11.10	10.80	7.85	10.70
Ta	2.00	1.39	1.49	1.37	1.56	2.19
W	1.75	1.02	4.02	2.59	2.1	3.41
Pb	19	1	17	18	22	26
Th	33.8	2.1	22.9	18.3	28.5	37.7
U	8.1	0.5	4.8	3.9	5.4	9.0

Trace Element Results ICP-MS

Sample	JC-09-8	JC-09-10B	JC-09-15	JC-09-17	JC-09-20	JC-09-21A
Li	49.1	9.6	31.9	31.7	2.87	24.8
Be	4.88	2.62	3.01	3.87	1.35	3.37
Co	0	4	1	1	45	1
Ga	20.7	20.6	22.7	20.9	22.0	22.6
As	1.17	1.44	1.72	1.79	3.72	0.461
Mo	0.727	1.22	1.47	0.698	1.01	0.847
Sn	3.82	2.4	3.19	4.39	1.42	3.29
Sb	0.014	0.036	0.112	0.008	0.044	0.037
Cs	2.64	1.87	0.94	2.09	0.50	1.63
La	103.0	76.8	90.6	122.0	40.9	94.3
Ce	168.0	136.0	172.0	194.0	83.1	175.0
Pr	19.00	14.80	20.70	25.20	9.81	20.10
Nd	64.70	54.20	78.90	90.80	40.90	73.10
Sm	11.40	10.00	15.20	16.70	9.22	13.60
Eu	0.49	2.44	3.61	0.68	2.37	1.87
Gd	9.77	9.10	13.20	15.10	8.78	11.50
Tb	1.32	1.26	1.79	1.99	1.36	1.54
Dy	7.15	6.97	9.62	10.50	7.96	8.00
Ho	1.39	1.37	1.82	1.94	1.58	1.48
Er	4.22	4.07	5.34	5.58	4.56	4.25
Tm	0.60	0.58	0.75	0.77	0.64	0.58
Yb	4.22	4.06	5.12	5.20	4.45	3.99
Lu	0.62	0.61	0.76	0.74	0.66	0.57
Hf	9.14	11.00	16.70	11.20	6.82	9.68
Ta	2.40	1.35	1.66	2.19	1.27	1.44
W	4.08	1.71	3.13	2.13	1.7	1.59
Pb	26	18	13	26	2	16
Th	40.9	20.0	11.0	37.0	2.6	18.5
U	9.0	3.9	2.9	7.6	0.7	3.8

Trace Element Results ICP-MS

Sample	JC-09-EN
Li	67.3
Be	2.91
Co	13
Ga	24.6
As	5.68
Mo	0
Sn	1.97
Sb	0.996
Cs	4.04
La	54.9
Ce	98.9
Pr	11.60
Nd	43.50
Sm	8.69
Eu	1.99
Gd	7.96
Tb	1.13
Dy	6.44
Ho	1.27
Er	3.75
Tm	0.53
Yb	3.75
Lu	0.56
Hf	6.18
Ta	1.13
W	5.98
Pb	12
Th	19.6
U	2.5

Appendix C - Oxygen Isotope Analysis

Samples were analyzed at Washington State University, Pullman, Washington. Samples were run with the UWG-2 garnet standard. Six samples of the standard were run with the Jarbidge Rhyolite samples and reported values of the standard are 6.47, 6.31, 6.20, 6.36, 6.43, and 6.38 ‰ in order of runs. The mean of these runs were used to correct standard data to a value of 5.90‰, and accordingly adjust the Jarbidge Rhyolite samples. The tables below summarize the results and reproduced values.

Sample	$\delta^{18}O_{quartz}$	$\delta^{18}O_{feldspar}$
JC-08-10	7.45	6.67
JC-08-24	7.72	8.22
JC-08-25	-	7.84
JC-09-4	7.96	6.61
JC-09-8	8.28	7.34
JC-09-15	8.46	7.74
JC-09-17	-	8.89

Sample	$\delta^{18}O_{quartz}$	$\delta^{18}O_{feldspar}$
JC-08-24	8.26	-
JC-08-25	-	7.87
JC-09-17	9.01	-

Appendix D - Geochronology

Crystals for analysis come from sample that was processed for geochemistry. Sample was sieved >2mm and not <0.5mm. Sieved sample was handpicked for feldspar crystals and sent to Auburn University. Geochronology was conducted at Auburn University's Auburn noble isotope mass analysis laboratory (ANIMAL), Auburn, Alabama. A staining method, using sodium cobaltinitrite, was used to identify sanidine minerals. Samples were irradiated at ... as part of package AU-14. Initially the samples were run as single crystal analyses; however, JC-08-24 yielded an unacceptable MSWD. JC-08-24 was run via a step heating method, which resulted in acceptable MSWD. The monitor has an accepted age of A J value = 28020000 ±112080.

Sensitivity (Moles/volt):	3.10581E-15	±	3.10581E-17
J-Value:	28020000	±	112080
Measured 40/36 of Air:	293	±	1.5
Mass Discrimination (% per amu):	-0.002115059	±	0.001015228
$(36/37)_{Ca}$:	0.000275	±	0.00001
$(39/37)_{Ca}$:	0.000757	±	0.00002
$(40/39)_{K}$:	0	±	0.0004
$(38/39)_{Cl}$:	0.01	±	0.01
% of Sample in Split	0.58		
Date of Irradiation:	8/28/2009		
Date of Analysis:	12/2/2009		

Sample	Unit	Outcrop	7.5' USGS quadrangle	Northing	Easting	Age	±1s
JC-08-10	Tjr	Bear Creek Summit	Jarbidge North	0627116	4631561	15.78	0.06
JC-08-24	Tjr	Wild Horse Reservoir	Badger Creek	0591852	4619700	16.29	0.03
JC-08-25	Tjr	Wild Horse Reservoir Dome	Wild Horse Reservoir	0602571	4620752	16.66	0.05

Sample: JC-08-10

Sample	^{40}Ar			^{39}Ar		
au14.1c.kfs.51	4.8786E-14	±	5.0923E-17	1.5508E-14	±	2.9153E-17
au14.1c.kfs.52	1.8402E-14	±	2.1215E-17	5.9816E-15	±	9.4708E-18
au14.1c.kfs.56	1.8968E-14	±	3.352E-17	6.3604E-15	±	2.071E-17
au14.1c.kfs.59	1.2145E-14	±	1.5267E-17	3.9888E-15	±	1.4289E-17
au14.1c.kfs.60	8.682E-15	±	1.2199E-17	2.8107E-15	±	1.1797E-17
au14.1c.kfs.61	1.5954E-14	±	2.6413E-17	5.0371E-15	±	1.9437E-17
au14.1c.kfs.67	1.3368E-14	±	2.2527E-17	4.393E-15	±	1.1955E-17
au14.1c.kfs.72	1.4422E-14	±	1.6525E-17	4.8419E-15	±	1.1643E-17
au14.1c.kfs.74	1.1383E-14	±	1.1185E-17	3.7385E-15	±	4.4259E-18
au14.1c.kfs.75	1.3947E-14	±	2.0606E-17	4.6443E-15	±	1.1732E-17

^{38}Ar			^{37}Ar			^{36}Ar		
3.4197E-17	±	2.5364E-19	4.973E-16	±	5.3436E-18	7.7257E-18	±	3.1277E-19
1.3149E-17	±	1.5203E-19	2.0921E-15	±	1.1723E-17	1.5468E-18	±	2.5224E-19
1.1504E-17	±	1.5255E-19	2.1211E-16	±	1.6675E-18	-3.935E-19	±	-7.225E-19
6.7571E-18	±	1.1194E-19	1.061E-16	±	2.1391E-18	1.0984E-18	±	3.2212E-19
5.7314E-18	±	1.8763E-19	1.0449E-16	±	2.6888E-18	1.0086E-18	±	3.394E-19
1.5666E-17	±	4.4793E-19	1.772E-16	±	1.6823E-18	3.2074E-18	±	3.1303E-19
9.1147E-18	±	1.2569E-19	1.9051E-16	±	2.8181E-18	1.1877E-18	±	2.4745E-19
9.9346E-18	±	1.7468E-19	1.4971E-16	±	2.4795E-18	3.2908E-19	±	2.2854E-19
9.1361E-18	±	1.275E-19	1.4475E-15	±	5.1589E-18	1.0371E-18	±	2.0941E-19
9.2977E-18	±	1.8096E-19	1.5693E-16	±	3.1025E-18	5.6813E-19	±	2.872E-19

%Rad	R	Age (Ma)			%-sd
0.9532	2.9987	15.8568	±	0.04807	0.00303
0.97516	3.00008	15.8641	±	0.09584	0.00604
1.00613	3.0005	15.8663	±	0.16207	0.01021
0.97328	2.9635	15.6715	±	0.14325	0.00914
0.96567	2.98287	15.7735	±	0.2071	0.01313
0.94059	2.97908	15.7535	±	0.12115	0.00769
0.97375	2.96315	15.6697	±	0.10536	0.00672
0.99326	2.9585	15.6451	±	0.09299	0.00594
0.97308	2.96274	15.6675	±	0.1236	0.00789
0.98796	2.96684	15.6891	±	0.11389	0.00726

Sample: JC-08-24

Step	^{40}Ar			^{39}Ar			^{38}Ar		
A	3.71562E-16	±	1.76726E-18	9.79637E-17	±	5.03809E-19	2.56214E-19	±	2.03342E-20
B	3.3258E-16	±	1.20369E-18	1.06903E-16	±	6.2782E-19	2.23457E-19	±	1.69111E-20
C	2.17117E-15	±	2.7108E-18	7.03803E-16	±	8.87487E-19	1.35245E-18	±	1.96206E-20
D	3.27356E-15	±	6.04736E-18	1.02398E-15	±	2.78878E-18	2.36283E-18	±	2.59626E-20
E	1.15849E-15	±	1.58239E-18	3.77518E-16	±	1.49823E-18	8.29408E-19	±	2.24535E-20
F	1.83459E-15	±	2.61719E-18	5.97299E-16	±	2.00584E-18	1.16748E-18	±	2.41827E-20
G	5.04714E-15	±	3.56687E-18	1.64203E-15	±	2.94366E-18	3.07407E-18	±	3.03849E-20
H	2.23931E-15	±	3.36075E-18	7.30154E-16	±	2.06324E-18	1.63902E-18	±	2.63846E-20
J	2.78943E-15	±	2.64196E-18	9.00613E-16	±	2.50831E-18	1.50246E-18	±	2.70796E-20
K	2.75097E-15	±	5.28734E-18	8.93773E-16	±	1.01922E-18	1.37245E-18	±	1.47191E-20
L	2.59235E-15	±	3.14816E-18	7.92392E-16	±	1.92018E-18	1.83127E-18	±	2.25069E-20
M	3.28518E-15	±	4.06821E-18	1.05874E-15	±	2.14746E-18	2.15407E-18	±	2.91996E-20
N	1.13803E-15	±	1.44201E-18	3.61894E-16	±	1.66527E-18	7.91885E-19	±	2.09481E-20
O	7.23475E-16	±	2.15459E-18	2.32548E-16	±	1.03531E-18	3.05568E-19	±	1.14204E-20

Step	^{37}Ar			^{36}Ar			%Rad	R
A	2.72502E-18	±	4.67655E-19	-3.17231E-21	±	-7.5357E-20	100%	3.80242
B	2.13986E-18	±	3.81097E-19	-1.58495E-19	±	-5.296E-20	114%	3.54916
C	1.9632E-17	±	3.61597E-19	-1.01063E-19	±	-5.4473E-20	101%	3.12735
D	3.03455E-17	±	5.06357E-19	2.97715E-19	±	5.25243E-20	97%	3.11098
E	1.11269E-17	±	4.74104E-19	-1.50846E-20	±	-6.0202E-20	100%	3.08052
F	1.75413E-17	±	5.21141E-19	4.67181E-20	±	4.58574E-20	99%	3.04837
G	4.64107E-17	±	6.6028E-19	2.24336E-20	±	3.07208E-20	100%	3.06968
H	2.17881E-17	±	5.7386E-19	1.64034E-20	±	3.80553E-20	100%	3.06027
J	2.62223E-17	±	6.09715E-19	6.63467E-20	±	4.87138E-20	99%	3.07549
K	2.67289E-17	±	6.43457E-19	1.13455E-20	±	3.05685E-20	100%	3.07418
L	2.52986E-17	±	6.89142E-19	4.79318E-19	±	4.88564E-20	95%	3.09280
M	3.13345E-17	±	5.2191E-19	-5.46909E-21	±	-7.8054E-20	100%	3.10443
N	1.03615E-17	±	4.50101E-19	1.63845E-20	±	4.63475E-20	100%	3.13128
O	6.27061E-18	±	3.99586E-19	-1.6297E-20	±	-5.3712E-20	101%	3.13179

JC-08-24 Continued

Step	Age (Ma)			%-sd
A	20.08	±	0.928	4.62%
B	18.75	±	0.779	4.15%
C	16.53	±	0.118	0.71%
D	16.45	±	0.099	0.60%
E	16.29	±	0.210	1.29%
F	16.12	±	0.145	0.90%
G	16.23	±	0.056	0.34%
H	16.18	±	0.123	0.76%
J	16.26	±	0.105	0.65%
K	16.25	±	0.095	0.59%
L	16.35	±	0.108	0.66%
M	16.41	±	0.077	0.47%
N	16.55	±	0.248	1.50%
O	16.56	±	0.334	2.02%

Sample: JC-08-25

Sample	^{40}Ar			^{39}Ar		
au14.3c.kfs.81	3.28598E-13	±	2.72158E-16	1.03826E-13	±	7.46061E-17
au14.3c.kfs.82	3.02254E-13	±	2.08138E-16	9.54029E-14	±	1.04341E-16
au14.3c.kfs.83	1.81114E-13	±	1.63257E-16	5.68653E-14	±	6.6138E-17
au14.3c.kfs.84	2.49213E-13	±	2.13592E-16	7.83248E-14	±	6.05636E-17
au14.3c.kfs.85	1.11519E-13	±	1.10456E-16	3.5446E-14	±	4.40761E-17
au14.3c.kfs.86	2.06926E-13	±	1.34748E-16	6.6179E-14	±	7.07408E-17
au14.3c.kfs.87	1.64698E-13	±	1.71356E-16	5.24799E-14	±	5.65357E-17
au14.3c.kfs.88	2.31846E-13	±	2.86993E-16	7.25196E-14	±	6.90128E-17
au14.3c.kfs.89	2.52301E-13	±	2.02526E-16	7.90539E-14	±	7.63058E-17
au14.3c.kfs.90	1.20069E-13	±	1.02254E-16	3.84123E-14	±	4.68778E-17
au14.3c.kfs.91	1.53373E-13	±	8.3125E-17	4.8962E-14	±	4.44241E-17
au14.3c.kfs.92	1.82791E-13	±	2.03172E-16	5.78583E-14	±	5.17706E-17
au14.3c.kfs.93	3.01243E-13	±	2.04269E-16	9.47763E-14	±	9.94544E-17
au14.3c.kfs.94	2.60396E-13	±	3.09816E-16	8.28664E-14	±	7.98092E-17
au14.3c.kfs.95	1.68044E-13	±	1.33053E-16	5.2913E-14	±	5.41206E-17
au14.3c.kfs.96	9.45114E-14	±	1.00808E-16	2.98288E-14	±	3.74347E-17
au14.3c.kfs.97	1.77017E-13	±	1.5568E-16	5.58359E-14	±	6.74117E-17
au14.3c.kfs.98	1.38913E-13	±	8.35724E-17	4.42449E-14	±	7.88976E-17
au14.3c.kfs.99	1.68073E-13	±	2.14538E-16	5.31336E-14	±	6.47008E-17
au14.3c.kfs.100	1.56987E-15	±	1.07192E-17	3.83566E-16	±	2.74336E-18

JC-08-25 Continued

Sample	^{37}Ar			^{36}Ar			%Rad	R
au14.3c.kfs.81	1.99745E-15	±	1.01762E-17	3.60223E-18	±	3.62548E-19	99.7%	3.15465
au14.3c.kfs.82	2.29281E-15	±	2.30543E-17	3.80895E-18	±	4.37585E-19	99.6%	3.15639
au14.3c.kfs.83	8.49359E-16	±	9.41115E-18	4.61352E-18	±	3.08633E-19	99.2%	3.16100
au14.3c.kfs.84	1.04163E-15	±	9.87765E-18	2.8995E-18	±	4.18715E-19	99.7%	3.17085
au14.3c.kfs.85	4.6532E-16	±	6.78153E-18	1.18042E-18	±	3.06912E-19	99.7%	3.13633
au14.3c.kfs.86	9.14223E-16	±	5.65167E-18	1.30955E-18	±	2.89518E-19	99.8%	3.12091
au14.3c.kfs.87	7.56735E-16	±	7.2425E-18	1.91399E-18	±	2.54581E-19	99.7%	3.12752
au14.3c.kfs.88	1.086E-15	±	8.97357E-18	4.23831E-18	±	2.96396E-19	99.5%	3.17974
au14.3c.kfs.89	1.04127E-15	±	7.2961E-18	8.31249E-18	±	3.78115E-19	99.0%	3.16043
au14.3c.kfs.90	7.02279E-16	±	4.99793E-18	9.29715E-19	±	2.55786E-19	99.8%	3.11865
au14.3c.kfs.91	5.83977E-16	±	1.57399E-18	4.37332E-18	±	3.02891E-19	99.2%	3.10609
au14.3c.kfs.92	7.36889E-16	±	9.40217E-18	1.87597E-18	±	2.82975E-19	99.7%	3.14971
au14.3c.kfs.93	1.37686E-15	±	6.98312E-18	9.17842E-18	±	4.62648E-19	99.1%	3.14984
au14.3c.kfs.94	1.05346E-15	±	4.77085E-18	4.14781E-18	±	4.22464E-19	99.5%	3.12757
au14.3c.kfs.95	7.82968E-16	±	6.33723E-18	1.4032E-18	±	3.06081E-19	99.8%	3.16803
au14.3c.kfs.96	4.84971E-16	±	5.55549E-18	2.45808E-19	±	1.98448E-19	99.9%	3.16602
au14.3c.kfs.97	5.95357E-16	±	3.65004E-18	2.32949E-18	±	2.99901E-19	99.6%	3.15797
au14.3c.kfs.98	7.11211E-16	±	5.76503E-18	1.73037E-18	±	3.16351E-19	99.6%	3.12807
au14.3c.kfs.99	8.61477E-16	±	4.57367E-18	5.29865E-19	±	2.26022E-19	99.9%	3.16027
au14.3c.kfs.100	1.92962E-17	±	1.40211E-18	4.74271E-19	±	3.36354E-19	91.1%	3.72745

Sample JC-08-25 Continued

Sample	Age (Ma)	%-sd
au14.3c.kfs.81	16.678 ± 0.019	0.12%
au14.3c.kfs.82	16.687 ± 0.023	0.14%
au14.3c.kfs.83	16.711 ± 0.026	0.16%
au14.3c.kfs.84	16.763 ± 0.021	0.13%
au14.3c.kfs.85	16.581 ± 0.030	0.18%
au14.3c.kfs.86	16.500 ± 0.022	0.13%
au14.3c.kfs.87	16.535 ± 0.026	0.16%
au14.3c.kfs.88	16.810 ± 0.027	0.16%
au14.3c.kfs.89	16.708 ± 0.023	0.13%
au14.3c.kfs.90	16.488 ± 0.028	0.17%
au14.3c.kfs.91	16.422 ± 0.020	0.12%
au14.3c.kfs.92	16.652 ± 0.025	0.15%
au14.3c.kfs.93	16.652 ± 0.022	0.13%
au14.3c.kfs.94	16.535 ± 0.027	0.16%
au14.3c.kfs.95	16.748 ± 0.024	0.14%
au14.3c.kfs.96	16.738 ± 0.032	0.19%
au14.3c.kfs.97	16.695 ± 0.027	0.16%
au14.3c.kfs.98	16.538 ± 0.034	0.20%
au14.3c.kfs.99	16.707 ± 0.031	0.19%
au14.3c.kfs.100	19.689 ± 1.401	7.11%